Atomistic simulation and analysis of novel group IV semiconductor alloys and devices

Michael Denis Dunne

Thesis submitted in partial fulfilment of the requirements
of the degree of Doctor of Philosophy

at the
Department of Physics,
University College Cork,
National University of Ireland

Supervisors: Prof. Eoin P. O'Reilly
Dr. Christopher A. Broderick
Dr. Stefan Schulz
Head of Department: Prof. John G. McInerney

January 2023

Contents

Declaration of Authorship

I, Michael Denis Dunne (student no. 113343766), hereby declare that, unless otherwise stated, this work is my own, and that it has not been submitted for another degree, either at University College Cork or elsewhere.

Signed: Michael Denis Dunne

Acknowledgements

I would like to begin by thanking all of the members, past and present, of the Photonics Theory Group (PTG) at Tyndall National Institute. It has been a pleasure to work with them over the past 4 years. I have learned so much from them over my four years in with the group. I wish all of them the best of luck in their future endeavours.

Of my colleagues in the PTG, I would like in particular to thank two of them for their contributions to the work that appears in this thesis. I thank Dr. Christopher Broderick, with whom I collaborated on most parts of my PhD studies and provided detailed advice on numerous aspects of my work. I would also like to thank Dr. Stefan Schulz for introducing me to the basics of electronic band structure calculations in the initial stages of my PhD and helping me to start working with the OMEN software package. I wish Chris and Stefan all the best as they continue their research in PTG. Similarly, I thank my examiners, both internal and external, for taking time out of their busy schedules to read and examine this thesis.

I thank Science Foundation Ireland for providing the funding which supported this research, under the project 15/IA/3082, Multiscale Simulation and Analysis of emerging Group IV and III-IV Semiconductor Materials and Devices.

I would like to thank also my friends and family for their constant support and encouragement throughout my research. In particular I'd like to thank my parents, Caroline and Timothy, for always supporting me in my studies and instilling in me from an early age the value of perseverance and hard work.

Finally, I would like to express my sincere thanks to my supervisor, Prof. Eoin O'Reilly for his guidance and patience throughout the duration of my research. I have benefited greatly from working with Eoin, both directly through his instruction and indirectly through his influence. I hope that my contribution to the ongoing research programme of the Photonics Theory Group has justified the trust he placed in me by taking me on as a research student

Abstract

A long held goal of the semiconductor community is the development of a direct gap silicon (Si) compatible material to enable the seamless integration of optical and electronic components on a single chip. The dominant elemental group-IV semiconductors silicon and germanium are the mainstays of current microelectronics, but their fundamental indirect gaps pose a roadblock to the development of active photonic components. The alloying of germanium with other group-IV elements, such as tin or carbon, has come into focus in recent years in pursuit of developing a direct gap alloy. Band engineering of germanium is attractive owing to the small difference between the indirect L_{6c}-Γ_{8v} and direct Γ_{7c}-Γ_{8v} band gaps of germanium which is only 140 meV. Alloying opens the possibility of reducing the Γ_{7c} state below that of the L_{6c} state leading to a direct gap alloy.

Initial work on $Ge_{1-x}C_x$ alloys have predicted the formation of a direct gap upon incorporation of dilute quantities of C (<1%), though there has not yet been an experimental demonstration of direct gap behaviour. $Ge_{1-x}Sn_x$ alloys have attracted greater research interest owing to the experimental demonstration of direct gap behaviour for a range of Sn compositions. Previous theoretical work suggested the transition from indirect to direct band gap occurs in a composition range of 6-11% Sn, while recent research indicates that a direct band gap emerges continuously with increasing x due to alloy band mixing. This atomistic effect, which is neglected in the widely-employed virtual crystal approximation (VCA), results in the alloy conduction band (CB) edge possessing hybridised character that evolves continuously from indirect (Ge L_{6c}-like) to direct (Ge Γ_{7c}-like) with increasing x.

In this thesis we present a theoretical analysis of electronic structure evolution in the highly-mismatched dilute carbide group-IV alloy $Ge_{1-x}C_x$ by adopting an atomistic approach encompassing calculations of the electronic structure using the semi-empirical tight-binding method. We demonstrate that C incorporation strongly perturbs the conduction band (CB) structure by driving hybridisation of A_1-symmetric linear combinations of Ge states lying close in energy to the CB edge. These calculations describe the emergence of a "quasi-direct" alloy band gap, which retains a significant admixture of indirect Ge L-point CB edge character. The trends identified by our calculations are markedly different to those expected based on a recently proposed interpretation of the CB structure based on the band anti-crossing model.

For $Ge_{1-x}Sn_x$ alloys we are interested in the impact of the previously overlooked alloy effects have on the band to band tunneling in the alloy. We achieve this using non-equilibrium Green's function (NEGF) band-to-band tunneling (BTBT) calculations based on atomistic tight-binding electronic structure calculations. We then extend this analysis to look at the effect of Sn incorporation on the current characteristics of TFET devices. We demonstrate that CB mixing strongly modifies the complex band structure, driving complex band anti-crossing that – for Sn compositions at which the band gap is assumed indirect in the VCA – strongly increases the BTBT generation rate G. Our results highlight the importance of atomistic effects in determining the electrical properties of $Ge_{1-x}Sn_x$ alloys

List of Publications

The following is a list of published work in which aspects of the research presented in this thesis have featured.

1. Refereed journal articles

- "Electronic structure evolution in dilute carbide $Ge_{1-x}C_x$ alloys and implications for device applications", Christopher A. Broderick, Michael D. Dunne, Daniel S P. Tanner, and Eoin P. O'Reilly; Journal of Applied Physics, 126, 195702, (2019) DOI: 10.1063/1.5111976
- "Atomistic origin of enhanced band-to-band tunneling in group-IV $Ge_{1-x}Sn_x$ alloys", Michael D. Dunne, Christopher A. Broderick, Mathieu Luisier, and Eoin P. O'Reilly; in preparation

2. Conference proceedings

- "Atomistic analysis of localisation and band mixing effects in $Ge_{1-x}(C,Sn)_x$ group-IV alloys", Christopher A. Broderick, Michael D. Dunne, Daniel S. P. Tanner, Amy C. Kirwan, Edmond J. O'Halloran, Stefan Schulz, and Eoin P. O'Reilly, Proceedings of IEEE 18th International Conference on Nanotechnology (IEEE Nano 2018), Cork, Ireland (2018) DOI: 10.1109/nano.2018.8626255
- "Multi-Scale Electronic Structure Analysis of Direct-Gap Group-IV Alloys: Implications for Device Applications", Christopher A. Broderick, Edmond J. O'Halloran, Amy C. Kirwan, Michael D. Dunne, Daniel S P. Tanner, Stefan Schulz, and Eoin P. O'Reilly; Proceedings of IEEE International Conference on Group IV Photonics, Singapore, (2019) DOI: 10.1109/GROUP4.2019.8925787
- "Atomistic analysis of band-to-band tunnelling in direct-gap $Ge_{1-x}Sn_x$ group-IV alloys", Michael D. Dunne, Christopher A. Broderick, Mathieu Luisier and Eoin P. O'Reilly, Proceedings of the 20th International Conference on Numerical Simulation of Optoelectronic Devices (NUSOD), (2020) DOI:10.1109/NUSOD49422.2020.9217765
- "Multi-scale theory and simulation of direct-gap group-IV semiconductor alloy", Christopher A. Broderick, Edmond J. O'Halloran, Michael D. Dunne, Amy C. Kirwan, Aleksey D. Andreev, Stefan Schulz and Eoin P. O'Reilly, Proceedings 2020 IEEE Photonics Society Summer Topicals Meeting Series (SUM), (2020) DOI:10.1109/SUM48678.2020.9161038

3. Conference talks

During the course of my doctoral research I have personally presented the following conference talks:

- "Theory of the electronic structure of direct-gap $Ge_{1-x}(C,Sn)_x$ group-IV alloys", Christopher A. Broderick, Michael D. Dunne, Daniel S. P. Tanner, Edmond J. O'Halloran, Amy C. Kirwan, Stefan Schulz, and Eoin P. O'Reilly; UK Semiconductors, Sheffield Hallam University, Sheffield, England (2019)
- "Atomistic analysis of band-to-band tunnelling in direct-gap $Ge_{1-x}Sn_x$ group-IV alloys", Michael D Dunne, Christopher A Broderick, Mathieu Luisier, and Eoin P. O'Reilly; International Conference on Numerical Simulation of Optoelectronic Devices (NUSOD), Turin, Italy (2020)
- "Enhanced band-to-band tunneling in direct-gap group-IV $Ge_{1-x}Sn_x$ alloys: impact of alloy band mixing", Michael D. Dunne, Christopher A. Broderick, Mathieu Luisier, and Eoin P. O'Reilly; American Physical Society (2021)

In addition to these talks I have also contributed to, and have had aspects of my work presented in the following conference talks, which were presented by my colleagues and collaborators:

- "Theory of localisation and band mixing effects in direct-gap $Ge_{1-x}(C,Sn)_x$ group-IV alloys", Christopher A. Broderick, Michael D. Dunne, Daniel S. P. Tanner, Edmond J. O'Halloran, Amy C. Kirwan, Stefan Schulz, and Eoin P. O'Reilly; IEEE Nano 2018, University College Cork, Ireland, (2018)
- "Theory of the electronic structure of direct-gap $Ge_{1-x}(C,Sn)_x$ group-IV alloy", Christopher A. Broderick, Michael D. Dunne, Daniel S. P. Tanner, Edmond J. O'Halloran, Amy C. Kirwan, Stefan Schulz, and Eoin P. O'Reilly; UK Semiconductors, Sheffield Hallam University, U.K, (2018)
- "Multi-scale modelling of group-IV semiconductor alloys: localisation, hybridisation and implications", C. A. Broderick, E. J. O'Halloran, A. C. Kirwan, M. D. Dunne, D. S. P. Tanner, S. Schulz and E. P. O'Reilly; Photonics West, San Francisco, U.S.A, (2018)
- "Group-IV semiconductor alloys: electronic structure evolution and the indirect- to direct-gap transition", Christopher A. Broderick, Edmond J. O'Halloran, Michael D. Dunne, Amy C. Kirwan, Daniel S. P. Tanner, Stefan Schulz and Eoin P. O'Reilly; 10th International Workshop on Bismuth-Containing Semiconductors, LAAS, Toulouse, France, (2019)
- "Multi-scale theory and simulation of direct-gap group-IV semiconductor alloys", Christopher A. Broderick, Edmond J. O'Halloran, Michael D. Dunne, Amy C. Kirwan, Aleksey D. Andreev, Stefan Schulz and Eoin P. O'Reilly; 2020 IEEE Photonics Society Summer Topical Meeting Series (SUM), Los Cabos, Baja California Sur, Mexico, (2020)

- "High-throughput atomistic calculations for direct-gap group-IV semiconductor alloys", Christopher A. Broderick, Michael D. Dunne, Daniel S. P. Tanner, Sarita Das, and Eoin P. O'Reilly, IEEE Photonics Society Summer Topicals Conference (IEEE SUM), Cabo San Lucas, Mexico (2022)

4. Conference posters

During the course of my doctoral research I have personally presented the following conference posters:

- "Theory of the electronic structure of direct-gap $Ge_{1-x}(C,Sn)_x$ group-IV alloys", Michael D. Dunne, Christopher A. Broderick, Daniel S. P. Tanner, Edmond J. O'Halloran, Amy C. Kirwan, Stefan Schulz, and Eoin P. O'Reilly, Photonics Ireland Cork, Ireland, (2018)
- "Theory and multi-scale simulation of direct-gap group IV semiconductor alloys", Michael Dunne, Christopher A. Broderick and Eoin P. O'Reilly; Photonics Ireland (2021)

In addition I have also contributed to, and have had aspects of my work presented, in the following conference posters, which were presented by my colleagues and collaborators:

- "The role of localisation and band mixing effects in direct-gap $Ge_{1-x}(C,Sn)_x$ group-IV alloys", Christopher A. Broderick, Michael D. Dunne, Amy C. Kirwan, Edmond J. O'Halloran, Daniel S. P. Tanner, Stefan Schulz, and Eoin P. O'Reilly; 34th International Conference on the Physics of Semiconductors (ICPS), Montpellier, France, (2018)
- "Indirect- to direct-gap transition in $Ge_{1-x}(C,Sn)_x$ semiconductor alloys: mechanisms and implications", Christopher A. Broderick, Michael D. Dunne, Amy C. Kirwan, Edmond J. O'Halloran, Daniel S. P. Tanner, Stefan Schulz, and Eoin P. O'Reilly; IOP Photonics, Aston University, England, (2018)
- "Group-IV semiconductor alloys: electronic structure evolution and the indirect- to direct-gap transition", Christopher A. Broderick, Edmond J. O'Halloran, Michael D. Dunne, Amy C. Kirwan, Daniel S. P. Tanner, Stefan Schulz and Eoin P. O'Reilly; 10th International Workshop on Bismuth-containing semiconductor, LAAS, Toulouse, France, (2019)
- "Multi-scale electronic structure analysis of direct-gap group-IV alloys: implications for device applications", Christopher A. Broderick, Edmond J. O'Halloran, Amy C. Kirwan, Michael D. Dunne, Daniel S P. Tanner, Stefan Schulz, and Eoin P. O'Reilly; IEEE International Conference on Group IV Photonics, Singapore, (2019)
- "Multi-scale electronic structure analysis of direct-gap group-IV alloys: implications for device applications", Amy C. Kirwan, Christopher A. Broderick, Edmond J. O'Halloran, Michael D. Dunne, Daniel S P. Tanner, Stefan Schulz, and Eoin P. O'Reilly; European Semiconductor Laser Workshop, Tyndall National Institute, University College Cork, (2019)

Chapter 1

Introduction

1.1 Background and motivation

The indirect fundamental band gaps of the group-IV semiconductors silicon (Si) and germanium (Ge) lead to intrinsically inefficient emission and absorption of light, rendering these materials unsuitable for applications in (active) photonic or photovoltaic devices. At present, the development of Si photonics is limited by the lack of direct-gap materials which are both suitable for applications in semiconductor lasers and light-emitting diodes, and are compatible with established complementary metal-oxide semiconductor (CMOS) fabrication and processing infrastructure[1–3]. Similarly, direct-gap semiconductors having a fundamental band gap of $\approx$ 1 eV and lattice constants commensurate with growth on Ge are required to facilitate the development of highly efficient multi-junction solar cells[4–6].

Coincident with the drive for Si-based photonics, the continuous reduction of transistor sizes that has underpinned progress in contemporary microelectronics is rapidly approaching the limits that can be accommodated using established complimentary metal-oxide-semiconductor (CMOS) processes and infrastructure[7, 8]. Consequently, as Moore's law [9] reaches its conclusion, there exists strong motivation to develop novel transistor architectures displaying improved performance and whose operation is either robust against, or exploits, quantum mechanical effects at nm length scales[8, 10, 11]. One such device is the tunneling field-effect transistor (TFET), which exploits band-to-band tunneling (BTBT) to inject carriers into the device channel[12]. Theoretical predictions have suggested that TFETs offer significant enhancements in performance over conventional field-effect transistors[12]. However, the mainstay group-IV semiconductors Si and Ge have proved a bottleneck to realising competitive TFET performance. Specifically, the indirect band gaps of Si and Ge mandate indirect (phonon-assisted) BTBT in order to conserve crystal momentum, with the associated low phonon-assisted BTBT generation rate then strongly limiting current generation[13–15].

These issues are being further compounded by the scaling of current CMOS devices. Previously, the scaling of the channel length and width of CMOS technologies was accompanied by the scaling of supply voltage and power consumed per device. As the size of devices has reduced further the non-scalability of the subthreshold swing is leading to a severe power crisis. For current technology

further reduction of the supply voltage would result in an exponential increase of the off-state leakage owing to thermionic emission in the switching mechanism. To reduce power consumption, new devices structures with the capability of steep subthreshold swings below the CMOS limit of 60 mV/decade are required. Realisation of the vast potential of CMOS technologies therefore requires that new materials be developed. To leverage the advanced manufacturing infrastructure of existing CMOS technologies and to integrate monolithically with exisitng CMOS chipsets these new materials must be silicon compatible, requiring a growth process that is compatible with the existing CMOS workflow.

1.2 Group-IV alloys

While there has been research into the integration of III-V photonic devices with existing CMOS fabrication, they have been limited by integration challenges and high costs. An improved solution is to use materials that are compatible with the current CMOS workflow. There has been a strong surge of interest in engineering the band structure of group-IV materials – in particular Ge, via strain or alloying – to produce semiconductors possessing a direct fundamental band gap[16, 17]. To date these efforts have centered on Ge, where the zone-centre Γ_{7c} conduction band (CB) edge lies only $\approx$ 145 meV higher in energy than the L-point L_{6c} CB minimum has made it the most attractive source of a direct band gap group-IV alloy, two methods have emphasised to bring about a direct gap using Ge, tensile straining of Ge[18–21] and alloying with other group-IV materials. However, to induce a direct gap through strained Ge requires a large amount of tensile strain[18–26] that makes the fabrication process difficult. Alloying has shown more promise, of the group-IV alloys Sn[27–32] has attracted the most interest, though broader interest in related group-IV alloys containing lead [33–37] (Pb) and carbon [38–41] (C) has begun to develop.

Initial interest in dilute carbide group-IV alloys originated over two decades ago, as a means to ameliorate issues related to the high levels of strain in Si_xGe_{1-x}/Ge heterostructures [42–44]. Related theoretical analyses have focused on the impact of C incorporation on the structural, vibrational and transport properties of ternary dilute $Si_yGe_{1-x-y}C_x$ alloys[45, 46]. To date, there have been few theoretical investigations of the implications of dilute C incorporation on the electronic structure of group-IV materials. The recent establishment of novel epitaxial techniques to enable substitutional incorporation of C in Ge opens up the potential to develop electronic, photonic and photovoltaic devices based on dilute carbide $Ge_{1-x}C_x$ alloys[38]. However, previous investigations of $Ge_{1-x}C_x$ alloys have provided a range of qualitatively conflicting conclusions, including observations of strong band gap bowing[47], a linear increase in band gap with increasing C composition x[48], or the emergence of a direct band gap for a limited range of C compositions[49].

Several studies have highlighted the challenges in growing high quality $Ge_{1-x}C_x$ alloys: because C-C bonds are stronger than Ge-C bonds, there is a strong tendency during growth to form C-related defect clusters[50]. Consistent with this analysis, Park et al. [51] showed that it would be virtually impossible to achieve fully substitutional growth of $Ge_{1-x}C_x$ alloys by conventional molecular beam

epitaxy (MBE) techniques. Recently, Stephenson et al. [52] presented a route to overcome this problem, using a hybrid gas/solid-source MBE approach with tetrakis(germyl)methane (4GeMe) as the C source, a molecule that has one C atom bonded to four Ge atoms. This enabled growth of good quality $Ge_{1-x}C_x$ alloys having C compositions $x \approx 0.2\%$ C[38]. Given the limited availability of experimental and theoretical data for $Ge_{1-x}C_x$ alloys, there is little information available in the literature regarding the alloy electronic structure. Recently, two theoretical analyses based on density functional theory (DFT) calculations have provided new insight into the $Ge_{1-x}C_x$ electronic structure. Stephenson et al. [39] used hybrid functional DFT to compute the band structure of ordered $Ge_{N-1}C_1$ ($x = \frac{1}{N}$) alloy supercells containing $N \leq 128$ atoms ($x \geq 0.78\%$), and demonstrated that C incorporation strongly perturbs the conduction band (CB) structure. On the basis of these calculations Stephenson et al. suggested that substitutional C acts as an isovalent impurity in Ge, giving rise to a C-related localised impurity state lying ≈ 0.4 eV above the Ge conduction band (CB) minimum. It was further suggested that this C-related localised impurity state undergoes a band anti-crossing (BAC) interaction with the extended zone-centre Γ_{7c} CB edge states of the Ge host matrix semiconductor – similar to that in the III-V dilute nitride alloy GaN_xAs_{1-x} [53–56] – resulting in (i) strong reduction of the fundamental band gap, (ii) the formation of a direct band gap for $x \gtrsim 0.8\%$, and (iii) closing of the alloy band gap for $x \lesssim 1.8\%$. However, suggestions regarding the presence and impact of a BAC interaction involving C-related localised states were drawn based on qualitative inspection of the calculated supercell band structures, without quantitative supporting analysis.

More recently, Kirwan et al. [41] also presented hybrid functional DFT calculations for ordered $Ge_{1-x}C_x$ alloy supercells. Here, supercell band structure calculations were supported by quantitative analysis of the character of the alloy CB edge states, as encapsulated in their associated band gap pressure coefficients. The calculated alloy band gap pressure coefficient was found to remain, independently of C composition x, approximately equal to that of the indirect (fundamental) L_{6c}-Γ_{8v} band gap of the Ge host matrix, suggesting limited hybridisation of the CB edge with Ge Γ_{7c} states. These calculations indicate the presence of a C-related localised state lying energetically within the band gap of the Ge host matrix, close in energy to the Ge CB minimum. However, analysis of the calculated alloy band gap pressure coefficients produced results inconsistent with the presence of a BAC interaction in $Ge_{1-x}C_x$, indicating instead that (i) C incorporation primarily drives hybridisation between the Γ_{7c} and X_{5c} CB edge states of Ge, and (ii) the alloy CB edge retains primarily indirect Ge L_{6c} character.

Alloying Ge with Sn has long been proposed as a direct gap group-IV alloy since initial theoretical calculations[57], with further theoretical and experimental investigations confirming direct gap behaviour[27]. The direct gap of $Ge_{1-x}Sn_x$ has received interest due to demonstrations of optically and electrically pumped lasing from $Ge_{1-x}Sn_x$ devices[31], opening the opportunity for $Ge_{1-x}Sn_x$ applications in integrated optoelectronics with existing CMOS technology based on Si. The reduction in band gap due to Sn incorporation is also expected to drive a strong increase in band to band tunneling (BTBT) in $Ge_{1-x}Sn_x$ alloys. This has sparked substantial research into $Ge_{1-x}Sn_x$ based tunneling field effect transistors (TFETs) which depend on BTBT[58–64]. Theoretical calculations

suggested $Ge_{1-x}Sn_x$ would become a direct gap material after a critical Sn composition where the energy of the direct CB edge Γ state decreased below that of the indirect L CB minimum state, this critical Sn composition was initially predicted to be in region of 20% Sn when using a virtual crystal approximation (VCA) based model[28]. Continuous downward revisions of the crossover energy led in recent years to an estimate between 6-11% Sn[65–67], demonstrating the difficulty in discerning the evolution of the electronic structure of $Ge_{1-x}Sn_x$ alloys using a VCA based model. Recently the importance of band mixing and alloy disorder on the electronic properties of $Ge_{1-x}Sn_x$ alloys has been recognised[68, 69], suggesting that instead of a sharp transition from indirect to direct gap material there is a gradual transition characterised by hybridisation of the CB edge states. The impact of this hybridisation on the behaviour of $Ge_{1-x}Sn_x$ based materials and devices has to date received little consideration.

1.3 Tunneling field effect transistors

The continuous reduction of transistor sizes that has underpinned progress in contemporary microelectronics is rapidly approaching the limits that can be accommodated using established complimentary metal-oxide-semiconductor (CMOS) processes and infrastructure. Consequently, as Moore's law reaches its conclusion, there exists strong motivation to develop novel transistor architectures displaying improved performance and whose operation is either robust against, or exploits, quantum mechanical effects at nanometre length scales. One such device is the tunneling field-effect transistor (TFET), which exploits band-to-band tunneling (BTBT) to inject carriers into the device channel[12]. Theoretical predictions have suggested that TFETs offer significant enhancements in performance over conventional field-effect transistors. However, the mainstay group-IV semiconductors Si and Ge have proved a bottleneck to realising competitive TFET performance. Specifically, the indirect band gaps of Si and Ge mandate indirect (phonon-assisted) BTBT in order to conserve crystal momentum, with the associated low phonon-assisted BTBT generation rate then strongly limiting current generation. Recent years have seen $Ge_{1-x}Sn_x$ based TFETs emerge as a contender for future devices, attracting numerous experimental and theoretical investigations[58–64].

1.4 Structure of the thesis and overview of primary results

This thesis focuses on two group-IV alloys: germanium-carbon and germanium-tin. We focus on germanium-carbon in chapter 3 where we develop the theory of its electronic structure using large scale tight-binding methods. In chapters 4 and 5 we investigate the transport properties of the group-IV alloy germanium-tin, using an atomistic non-equilibrium Greens function framework. In chapter 2 of this thesis we detail and develop the relevant theoretical background for the work that follows in the remaining chapters. This background firstly focuses on developing the fundamental theoretical framework for the tight-binding method which is utilised in later chapters to simulate the electronic band structures of group-IV alloys. The second key set of models of this thesis

described are the transport models which are used to model band-to-band tunneling in germanium-tin alloys. Also included in chapter 2 are details of the fundamental theory of electronic band structure and relevant fundamental theory relating to group-IV optoelectronics.

The investigation of the electronic, optical and material properties of germanium carbon alloys begins in chapter 3 where we further develop the theory of the electronic structure of $Ge_{1-x}C_x$ alloys. We provide an investigation of the implications of band mixing effects on the evolution of the electronic band structure of $Ge_{1-x}C_x$ with increasing C composition using a range of atomisitc tight-binding calculations. Recent theoretical and experimental investigations of $Ge_{1-x}C_x$ alloys have indicated that incorporation of C into bulk Ge causes a strong reduction in the direct band gap of the alloy, bringing about the formation of an isovalent impurity state 0.4 eV above the Ge conduction band minimum for dilute quantities of carbon (<1%). Existing literature would suggest that this C localised impurity state undergoes a band anti-crossing interaction resulting in the formation of a direct band gap for compositions x $\approx$ 1%. Recent research has continued to investigate $Ge_{1-x}C_x$ alloys through a BAC interaction with limited success in describing the full evolution of the alloy band structure[70, 71] However, quantitative analysis of this C localised state in disordered structures has been lacking: these conclusions have been based on the analysis of the band structure of $Ge_{M-1}C_1$ supercells, which incorporate a very high degree of ordering.

A more recent DFT analysis of the band gap pressure coefficients of $Ge_{1-x}C_x$ supercells also revealed a different picture to previous works [41]. The calculated alloy band gap pressure coefficient was found to largely remain the same as the L_{6c}-Γ_{8v} band gap of the Ge host matrix, thereby implying the C-related localised state in the band gap retains primarily indirect gap character. Motivated by these recent findings, in chapter 3 we seek to further elucidate the impact of C incorporation on the band structure. Using a tight-binding method parameterised from density functional theory calculations we investigate the electronic structure of $Ge_{1-x}C_x$ alloys for a range of compositions and particularly larger supercells that are outside the scope of computationally intensive DFT calculations. Larger supercells will allow us to quantify the impact that C incorporation in the ultra dilute limit and local alloy disorder have on the electronic structure.

Ordered alloy calculations confirm the presence of a C-induced localised state lying within the Ge host matrix band gap. Direct analysis of the character demonstrate that the localised state retains primarily indirect (Ge L_{6c}) gap character. Explicit analysis of the CB eigenstates in supercells containing up to 2000 atoms provides a broader picture of the electronic structure evolution. Specifically, we confirm that $Ge_{1-x}C_x$ admits a "quasi-direct" band gap in ordered alloy supercells. While the CB minimum appears at the zone centre of a $Ge_{N-1}C_1$ supercell, the associated eigenstate in selected supercells is formed predominantly of a linear combination of Ge L_{6c} CB edge states having purely s-like orbital character at the C lattice site. We further demonstrate that the alloy CB edge exhibits minimal localisation with increasing supercell size, challenging the suggestion that the introduction of an isolated substitutional C atom in Ge generates a (strongly) localised impurity state.

For disordered alloy supercells we find that short-range alloy disorder gives rise to a distribution of C-related localised states – associated with nearest-neighbour C-C pairs, as well as larger clusters of substitutional C atoms and various C-Ge-C type neighbour complexes – lying energetically within the Ge band gap, with these states acquiring minimal direct (Ge Γ_{7c}) character. Overall, our analysis reveals behaviour that is markedly different to that expected on the basis of the BAC model and, in agreement with the conclusions of Kirwan et al. [41], we demonstrate that C incorporation does not drive the formation of a direct band gap.

The investigation of the electronic, optical and material properties of germanium tin alloys begins in chapter 3 where we develop the theory of the electronic structure of $Ge_{1-x}Sn_x$ alloys and use the tight-binding method to investigate the implications of band mixing effects on the complex band structure of $Ge_{1-x}Sn_x$ alloys with increasing Sn composition. We then carry out a high throughput analysis of the impact that band mixing has on the band-to-band tunneling generation rate. Recent theoretical and experimental investigations of $Ge_{1-x}Sn_x$ alloys have indicated that incorporation of Sn into bulk Ge causes a strong reduction in the direct band gap of the alloy[65–67], bringing about an indirect to direct band gap transition for 10% Sn content. Existing literature would suggest that this transition from an indirect to a direct band gap in $Ge_{1-x}Sn_x$ alloys should be sharp in nature[65–67]. This is to say that up to a certain critical composition of Sn the band gap will be purely indirect (L-like) in nature, while at this critical Sn composition and above it the band gap will be purely direct (Γ-like) in nature.

Recent experimental and theoretical research has begun to challenge this existing assertion of the nature of the band gap transition in $Ge_{1-x}Sn_x$ alloys[68, 69]. Rather than a sharp transition from an indirect to a direct band gap, results from experimental photovoltage measurements and theoretical hydrostatic pressure calculations of the electronic alloy band structure indicate a continuous evolution of Γ character at the conduction band gap edge[68, 69], as the band gap narrows as a function of Sn concentration. This increase of Γ character at the conduction band edge, whose pressure coefficient appears to asymptotically approach that of Γ in pure Ge, is indicative of band mixing effects in the alloy which have not generally been accounted for in the contemporary literature[65–67]. The presence of band mixing effects in the alloy causes the distinction between direct and indirect band gaps to break down. As such, simple models like the virtual crystal approximation (VCA), which neglects effects related to band mixing and alloy disorder are insufficient to accurately describe the electronic band structure of $Ge_{1-x}Sn_x$ alloys. Atomistic calculations which explicitly account for the differences in size and chemical properties between Ge and Sn are required to provide quantitative insight into the properties of real $Ge_{1-x}Sn_x$ alloys.

The primary aims of this work are twofold. Firstly, to move beyond the VCA and establish atomistic quantum kinetic BTBT calculations that fully capture the electronic and transport properties of realistic, disordered $Ge_{1-x}Sn_x$ alloys. And, secondly, to apply this approach to elucidate the impact of Sn incorporation on the $Ge_{1-x}Sn_x$ complex band structure, and hence to explicitly quantify the impact of atomistic alloy effects on the direct BTBT generation rate G. We achieve these aims using non-equilibrium Green's function (NEGF)[72] BTBT calculations based on atomistic tight-binding (TB) electronic structure calculations. This fully atomistic framework allows to explicitly

analyse the impact of alloy band mixing and short-range disorder on the complex band structure and G, providing new insights relevant to proposed TFET applications of $Ge_{1-x}Sn_x$ alloys and highlighting the shortcomings of the VCA.

Beginning with idealised, ordered alloy supercells we demonstrate that Sn-induced L_{6c}-Γ_{7c} hybridisation induces a complex band-anticrossing that strongly modifies the dispersion of the evanescent Bloch band linking the valence band (VB) and CB edges. This modified complex band structure can produce a direct-gap-like pathway for BTBT at Sn compositions for which $Ge_{1-x}Sn_x$ is assumed to be indirect-gap in the VCA. Combined with the strong Sn-induced band gap reduction, this modified complex band structure further contributes to strong enhancement of G at fixed applied electric field. For ordered alloys this enhancement is found to far exceed previous VCA-based predictions with, e.g., our NEGF-calculated G at $x = 6.25\%$ being approximately four orders of magnitude larger than in pure Ge for a field of 1 $MVcm^{-1}$. We explicitly verify that Sn-induced L_{6c}-Γ_{7c} hybridisation drives this behaviour by using a model $\mathbf{k}\cdot\mathbf{p}$ Hamiltonian which, employed in conjunction with a semi-classical calculation of G based on the WKB approximation, quantitatively reproduces the enhancement and electric field dependence of G obtained from full atomistic NEGF calculations for ordered alloys.

For disordered alloys we perform high-throughput calculations to predict the dependence of G on x at fixed applied electric field using large, randomly disordered supercells. This analysis reveals that short-range alloy disorder reduces the impact of alloy band mixing, but that a disordered $Ge_{1-x}Sn_x$ alloy nonetheless retains the direct-gap-like BTBT pathway identified for idealised, ordered alloys. This direct-gap-like BTBT is driven by the impact of Sn-induced alloy band mixing on the complex band structure, and its onset hence occurs abruptly in response to Sn incorporation. As such, the direct BTBT generation rate undergoes an abrupt increase compared to pure Ge, even at low x for which the alloy retains primarily indirect-gap character. Our atomistic quantum kinetic calculations predict BTBT generation rates that, at fixed x, typically exceed equivalent VCA-based calculations by approximately one order of magnitude. Overall, our analysis provides new insight into the electronic properties of this emerging semiconductor material system, and highlights that previously overlooked atomistic effects will have important consequences for carrier transport properties relevant to proposed device applications.

With increasing interest in $Ge_{1-x}Sn_x$ as a CMOS-compatible direct-, narrow-gap semiconductor, several groups have demonstrated fabrication and characterisation of prototype $Ge_{1-x}Sn_x$-based TFETs, with the goal of achieving improved performance – specifically, subthermionic subthreshold swing, and improved "on" and "off" state current characteristics – compared to conventional Si_xGe_{1-x}-based group-IV TFETs[58–64]. In support of these efforts, a number of groups have undertaken theoretical investigations of $Ge_{1-x}Sn_x$-based TFET device structures[73–85]. These previous calculations have, due to the availability of a corresponding workflow in commercial software, centred on a single approach: using a band structure computed via the empirical pseudopotential method in the virtual crystal approximation (VCA) as input to a semi-classical BTBT calculation based on the Wentzel-Brillouin-Kramers (WKB) approximation[73–85]. In the VCA each atom is assumed to have interpolated properties associated with some defined average "$Ge_{1-x}Sn_x$" atom,

so that atomistic effects resulting from the large differences in chemical properties and covalent radius between Ge and Sn atoms are neglected. In practice, this limits the ability to make quantitative a priori predictions of alloy electronic properties. In VCA-based calculations the transition from an indirect to direct band gap has been assumed to occur abruptly at a single, critical Sn composition in the range $x = 6 - 9\%$, based generally on post-hoc fitting of bowing parameters to match experimental band gap measurements. The predicted Sn composition at which $Ge_{1-x}Sn_x$ becomes direct-gap has then been consistently revised downwards [65–67] compared to earlier predictions [28, 57] in response to emerging experimental data, highlighting the failure of the VCA to reliably predict $Ge_{1-x}Sn_x$ alloy electronic properties. Indeed, the breakdown of the VCA for $Ge_{1-x}Sn_x$ was recognised [86] and demonstrated [28] in early analysis. Recent measurements [69] and calculations [68] have demonstrated that Sn incorporation drives alloy-induced hybridisation of the Ge L-point L_{6c} conduction band (CB) minimum and zone-centre Γ_{7c} CB edge states, with this atomistic band mixing then resulting in a continuous evolution of the character of the alloy CB edge from indirect (Ge L_{6c}-like) to direct (Ge Γ_{7c}-like) with increasing Sn composition x. So, while VCA-based analysis has enabled impressive initial progress, a direct atomistic approach is required to quantitatively predict the electronic structure evolution in $Ge_{1-x}Sn_x$ alloys and identify consequences for proposed device applications[68, 87, 88].

In chapter 5 we investigate the impact of Sn incorporation on the behaviour of $Ge_{1-x}Sn_x$-based TFETs for different device structures and Sn compositions. Two types of devices were used in these calculations, a gate all around (GAA) TFET and a double gate ultra thin body (DGUTB) TFET. We use an atomistic tight binding model with the transport calculations to capture the impact of CB hybridisation on the electrical characteristics of $Ge_{1-x}Sn_x$ TFETs. The characteristics of primary interest are the sub-threshold swing, threshold current I_{on} and off current I_{off}. We aim to determine how the enhanced generation rates seen in chapter 4 manifest in realistic TFET calculations. We are primarily interested in the impact at low Sn compositions where the reduction in the area of the complex band joining the CB and VB edges is largest and should therefore lead to significantly enhanced tunneling rates.

Our investigation of the impact of atomistic effects on the current characteristics of $Ge_{1-x}Sn_x$ based TFETs reveal an increase in I_{on} when compared with the frequently used VCA framework demonstrating that the benefits of atomistic effects that lead to an enhanced generation rate in chapter 4 have been transferred to an increase in on currents in $Ge_{1-x}Sn_x$ TFETs. Disorder serves to reduce some of the benefits of band mixing and alloy band gap reduction, however, I_{on} remain elevated above those of the VCA for both TFET devices examined here. These results further build on the theoretical predictions of attractive performance of $Ge_{1-x}Sn_x$ based TFETs for post CMOS computing. Further research will be required to combine our atomistic alloy calculations with loss processes such as TAT[64], in order to improve predictions of current $Ge_{1-x}Sn_x$ TFETs designs

Finally in chapter 6 we summarise and conclude. We recapitulate the main results and findings of the research presented in this thesis and provide an outlook of potential future research directions which arise from the work detailed in this thesis, pertaining to group-IV optoelectronics.

Chapter 2

Theoretical Methods

In this chapter we review and detail some of the fundamental principles and methods which underline the objectives and methodologies of the research presented in later chapters of this thesis. We begin in section 2.1 by providing a general overview of the electronic band structure and its features including high symmetry points and the atomic band character of the conduction and valence bands and the complex band structure. Following this, in section 2.2 we describe one of the key models that will be used in this thesis, the tight-binding method which is used for calculations of the electronic band structure of germanium-based group-IV alloys. Section 2.3 then provides an overview of the non-equilibrium Green's function method that is used for transport calculations.

2.1 Electronic band structure

Quantum theory has been key to the description of the properties of bulk crystalline semiconducting materials. A key characteristic of crystalline solids is the repeated structure of the material which lends itself to the famous Bloch's theorem[89] that is encapsulated in the equation

$$\psi(\mathbf{k}, \mathbf{r}) = e^{i\mathbf{kr}} u(\mathbf{k}, \mathbf{r}) \tag{2.1}$$

where the wave function $\psi(\mathbf{r})$ is that from the Schrödinger's equation, $H|\psi(\mathbf{r})\rangle = E|\psi(\mathbf{r})\rangle$. $u(\mathbf{r})$ is a periodic function with the periodicity of the underlying crystal lattice,

$$u(\mathbf{k}, \mathbf{r}) = u(\mathbf{k}, \mathbf{r} + \mathbf{R}) \tag{2.2}$$

Where r is a position within the lattice and R is a Bravais lattice vector. Wave functions that satisfy Eq. (2.1) and (2.2) are referred to as Bloch functions representing Bloch states. Two subscripts are generally attached to the wave functions, n and $\mathbf{k}$, representing a particular state and its associated wave vector, respectively. At each value of $\mathbf{k}$ there can be many different states each referred to with a particular n value. Each Bloch function $\psi_{n\mathbf{k}}(\mathbf{r})$ with a pairing of n and $\mathbf{k}$ is unique within the first Brillouin zone, that region within a reciprocal lattice vector G of the zone centre. States outside the zone can be translated back by observing in Eq. (2.1) and (2.2) that

$\psi_{n\mathbf{k}}(\mathbf{r}) = \psi_{n(\mathbf{k}+\mathbf{G})}(\mathbf{r})$. In free atoms discrete energy levels are formed corresponding to each n, however, when the atoms are brought close together as in a crystal lattice regions of allowed and forbidden bands form, due to the interaction of atomic orbitals. The forbidden bands create band gaps in the material and the allowed bands are separated into two types, energy levels occupied by an electron called valence bands (VB) and ones not occupied by electrons called conduction bands (CB). Electrons in the VB can be excited across the band gap into the CB, this can occur via direct and indirect path as shown in Fig.2.1, where we plot the energy E associated with each wave vector $\mathbf{k}$ against $\mathbf{k}$. For an indirect gap, an electron will need both a change in energy and momentum to complete the transfer.

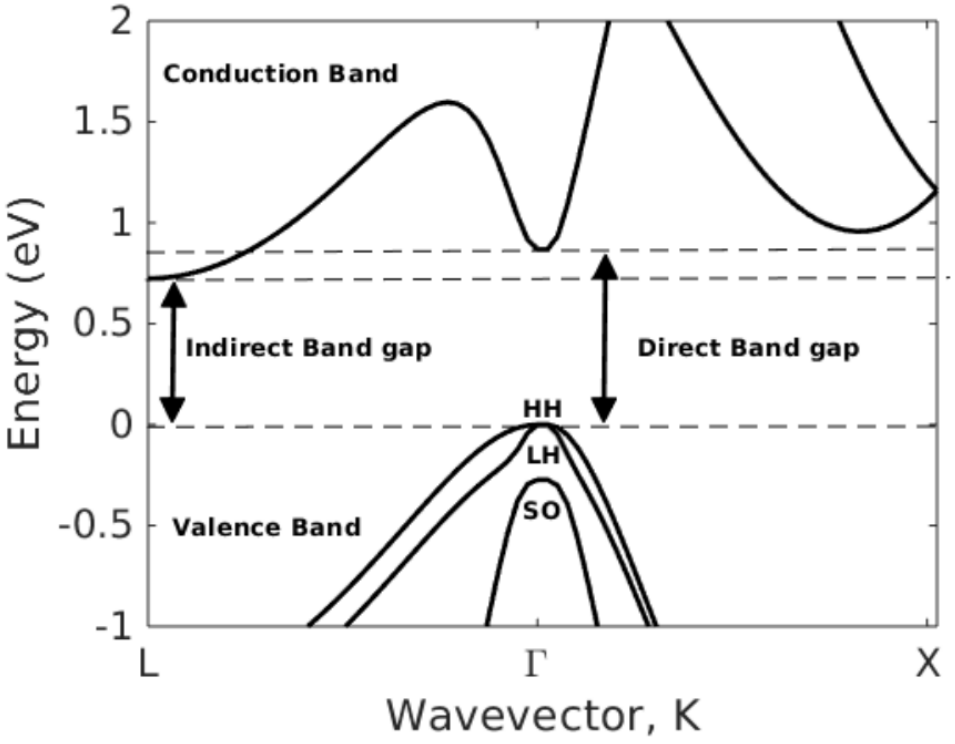

FIGURE 2.1: Bandstructure of Ge. Arrows indicate the primary indirect (L CB state to the Γ VB HH state) and direct band gaps (CB zone centre Γ state to VB HH Γ state). Note the small difference between the direct and indirect band gaps of just 141 meV

Figure 2.1 shows the band structure of bulk semiconductor germanium and shows how energy bands may be represented in **k**- space. Four bands are included in the figure, a single CB and three VBs. The three VB states are the heavy-hole (HH) band, light-hole (LH) band and the spin split-off (SO) band. Based on the size of the band gap energy, three types of solids can be defined, metals where the CB and VBs overlap with a band gap of 0 eV, insulators where there is a large energy gap (typically larger than 4 eV) and semiconductors where the band gap is intermediate between a metal and insulator, but typically with a value near 1 eV. The wave vector in Fig.2.1 is labelled at three high symmetry points of the lattice, at L, Γ and X. In this thesis we will be primarily interested in transitions at L (indirect) and Γ (direct).

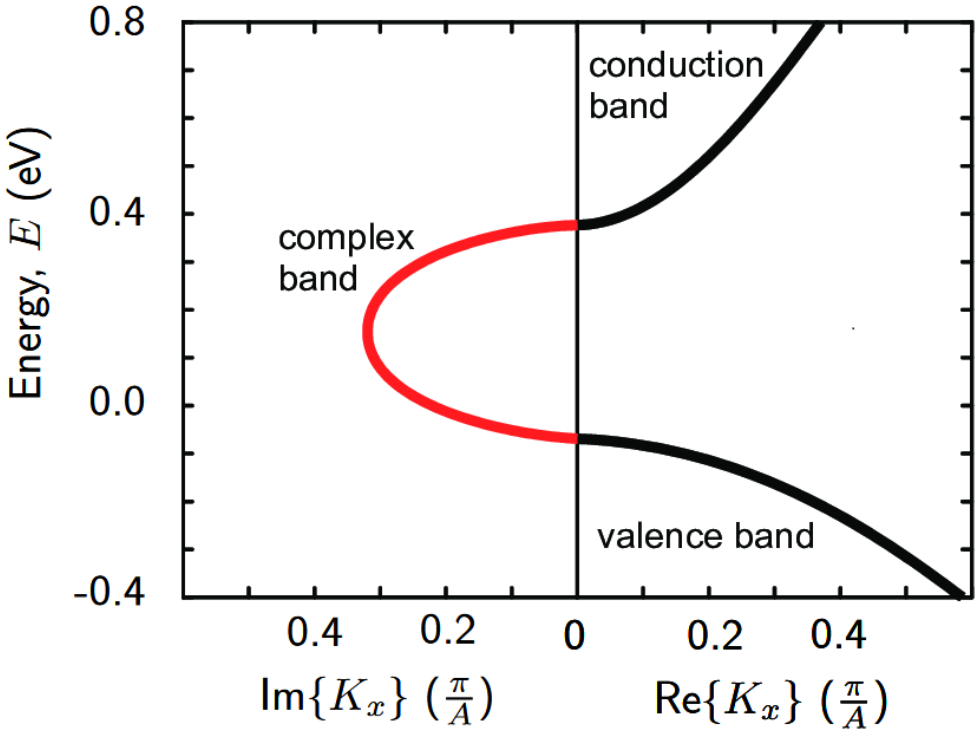

FIGURE 2.2: Sample complex bandstructure where a complex band links the CB at the zone centre to the VB at the zone centre. Further details of the complex band structure are explained in Sec.2.3.1

Up to now we have been focusing on the real band structure - that is when the wavevector is a real number. Another property of the band structure we can look at is the complex band structure which is the case where the wavevector can possess both real and imaginary components. Imaginary components of $\vec{\mathbf{k}}$, when present, indicate evanescent states; that is, the state grows or decays in magnitude from one repeat unit to the next. Similar to conventional band structure, the dispersion relation, $E(\vec{\mathbf{k}})$, is a central quantity in the complex band structure (CBS). The difference is that we now consider evanescent states in the material by letting the components of $\vec{\mathbf{k}}$ be complex. As in conventional band structure, each $\vec{\mathbf{k}}$ produces an eigenvalue problem that can be solved for E; in this way we can regard $E(\vec{\mathbf{k}})$ as a multi-valued complex function. Even though there will be multiple (and generally complex) E associated with each complex $\vec{\mathbf{k}}$, we are only interested in $\vec{\mathbf{k}}$ that produce real E. The key impact of these evanescent states is that they permit a complex band to join the band edge states at the Γ point as in Fig.2.2. These complex bands then provide a path to allow tunneling of electrons or holes between the band edge states, which is the driving factor behind current generation in TFETs.

A major part of this thesis will be concerned with calculations of the electronic band structure of group-IV elements and diamond-structured semiconductor alloys formed from them, which are characterised by a fourfold tetrahedral coordination and sp^3-hybridised covalent bonding. In the next section of this chapter we will describe how the electronic band structure of these group-IV materials may be investigated using the tight-binding method.

2.2 Tight-binding method

In this section we outline the theory of the electronic structure of semiconductor compounds and alloys based on the tight-binding method. We begin in section 2.2.1 by deriving tight-binding Hamiltonian for the two-atom primitive unit cell of a zinc blende semiconductor compound, which we will employ extensively throughout this thesis when developing the theory of the electronic structure of the group-IV alloys GeC and GeSn. Following this, in section 2.2.2 we then present the extension of the 2-atom sp^3s^* Hamiltonian to that we will use in supercell calculations.

2.2.1 Derivation

Following on from our discussion in the previous section we now set out to solve the time independent Schrödinger equation (Eq. (2.3))in order to calculate the electronic properties of the group-IV alloys of interest

$$\hat{H}\psi_n(\mathbf{k}) = E_n(k)\psi_n(\mathbf{k}) \tag{2.3}$$

where $\psi_n(\mathbf{k})$ are the Bloch functions that represent the eigenstates of the system. Several methods exist for solving the Schrödinger equation in order to calculate the its eigenvalues, we are using the tight binding method which makes the assumption that the extended Bloch states of the crystal can be described using a linear combination of atomic orbitals (LCAO). The basis we will use for these states are Bloch sums $\phi_{\alpha l\rho}$, where α represents the atomic orbital (s, p etc) of an atom l with a spin ρ. A Bloch sum for a given orbital is defined as[90]

$$\phi_{\alpha l\rho}(k) = \frac{1}{\sqrt{N}}\sum_j e^{i\mathbf{k}\cdot\mathbf{r}_{jl}}\phi_{\alpha jl\rho} \tag{2.4}$$

where $\phi_{\alpha jl\rho}$ represents the orbital α localised at atom l in the j^{th} unit cell with spin ρ. Where the sum j runs over all unit cells in the crystal. N is the total number of unit cell in the crystal, $\mathbf{r}_{jl}$ is the position vector of atom l in unit cell j, the position vector is defined as $\mathbf{r}_{jl} = \mathbf{R}_j + \mathbf{r}_l$ where $\mathbf{R}_j$ is the Bravais lattice vector giving the position of the j^{th} unit cell and $\mathbf{r}_l$ is the position of atom l in the unit cell. Using these Bloch sums $\phi_{\alpha l\rho}(k)$ we can then calculate the crystal eigenstates $\psi_n(\mathbf{k})$ as

$$\psi_n(\mathbf{k}) = \sum_{\alpha,l,\rho} C_{n\alpha l\rho}(\mathbf{k})\phi_{\alpha l\rho}(k) \tag{2.5}$$

where the sum runs over the atomic orbitals α, the electron spin ρ and the atom l in each cell. We can use this formalism for the eigenstates of the Hamiltonian to solve the Schrödinger equation. We do this by substituting our form of $\psi_n(\mathbf{k})$ into Eq. (2.3) and operating on the left with the complex conjugate of $\phi_{\beta m\rho'}(k)$, that has an orbital at an atom m in the unit cell with spin ρ'. We then obtain

$$\sum_{\alpha,l,} C_{n\alpha l\rho}(\mathbf{k}) \left(\langle \phi_{\beta m\rho'}(k) | \widehat{H} | \phi_{\alpha l\rho}(k) \rangle - E_n(\mathbf{k}) \langle \phi_{\beta m\rho'}(k) | \phi_{\alpha l\rho}(k) \rangle \right) = 0 \tag{2.6}$$

which is usually defined in terms of the Hamiltonian and the overlap matrices between the Bloch sums, that are defined as[91–93]

$$H_{\beta m\rho',\alpha l\rho}(\mathbf{k}) = \langle \phi_{\beta m\rho'}(k) | \widehat{H} | \phi_{\alpha l\rho}(k) \rangle \tag{2.7}$$

and

$$S_{\beta' m\rho',\alpha l\rho}(\mathbf{k}) = \langle \phi_{\beta m\rho'}(k) | \phi_{\alpha l\rho}(k) \rangle \tag{2.8}$$

The overlap matrices can then be defined in terms of Kronecker delta functions δ_{ij} based on basic quantum mechanics. Where we have that orbitals on a given atomic site are orthogonal to each other and orbitals of opposite spin are orthogonal to each other. We also make the assumption that there is no overlap between orbitals on neighbouring atomic sites, which can also be achieved by using the orthogonalisation procedure of Löwdin [94]). With these assumptions the overlap matrix can be defined as

$$S_{\beta' m\rho',\alpha l\rho}(\mathbf{k}) = \delta_{\beta\alpha}\delta_{ml}\delta_{\rho'\rho} \tag{2.9}$$

This simplifies one aspect of Eq. (2.6), next we rewrite the Hamiltonian $H_{\beta m\rho',\alpha l\rho}(\mathbf{k})$ using Eq. (2.4) to get an expression for the matrix elements of the tight-binding Hamiltonian[93, 95]

$$H_{\beta m\rho',\alpha l\rho}(\mathbf{k}) = \sum_j e^{i\mathbf{k}\cdot(\mathbf{r}_{jl}-\mathbf{r}_{jm})} \langle \phi_{\beta m\rho'}(k) | \widehat{H} | \phi_{\alpha l\rho}(k) \rangle \tag{2.10}$$

where $\langle \phi_{\beta m\rho'}(k) | \widehat{H} | \phi_{\alpha l\rho} \rangle$ are the matrix elements of the Hamiltonian between the atomic orbitals β and α on atoms m and l with spins ρ' and ρ.

In the tight-binding method the matrix elements $\langle \phi_{\beta m\rho'}(k) | \widehat{H} | \phi_{\alpha l\rho}(k) \rangle$ are adjustable parameters used to fit to the results of ab initio calculations. A key assumption of the tight-binding method used in this thesis is that we limit the interactions between orbitals to those between nearest neighbour atoms. Therefore the sum in Eq. (2.10) will run over pairs of nearest neighbour atoms only. This simplification will have minimal impact on the accuracy of calculations as the orbital functions $\phi_{\beta m\rho'}(k)$ will rapidly decay away from the atom m they are centred on and therefore the matrix element will be small.

In tetrahedrally-coordinated, solids such as those with the zinc-blende structure, the valence orbitals are shared between neighbouring atoms to form sp^3-hybridised bonds which can be treated using a LCAO. To model the physics of the sp^3 bonding, Chadi and Cohen used an sp^3 basis in Eqs. (2.3-2.10)[91]. This resulted in an accurate description of the valence band structure using

the tight-binding method, due to sp^3-hybridised bonds present between the atoms. However, the conduction band structure is made up of anti-bonding orbitals that are unoccupied, therefore these behave like free electrons that are difficult to describe using a LCAO. This resulted in a poor fit to conduction band structure using the method of Chadi and Cohen[91], especially away from the zone centre Γ point[96]. Due to the importance of the indirect CB L state in the behaviour of group-IV alloys of interest in this thesis a modified version of the sp^3 basis that accurately models the CB edge states is required. The modification was devised by Vogl et al. where the sp^3 model was extended to include an excited s-like atomic orbital, s^* to form the sp^3s^* model[92]. The sp^3s^* model allows interactions between the p-like orbitals and excited s^* orbitals, this improves the accuracy of the calculated CB in the tight-binding method[92].

With the sp^3s^* basis we can now move to calculate the matrix elements $\langle\phi_{\beta m\rho'}(k)|\widehat{H}|\phi_{\alpha l\rho}(k)\rangle$ for the primitive unit cell which contains two atoms, one cation and one anion. In the sp^3s^* model there are five orbitals per atom, one s-orbital, three p-orbitals and an excited s^*-orbital. With the inclusion of spin we then get a total of ten orbitals per atom and as a result the basis set, of one cation and one anion, contains twenty orbitals $|\phi_{\alpha l\rho}(k)\rangle$, where $\alpha = \mathrm{s}^*$, s, x, y, z (with the s^* and s orbitals having s-like symmetry, and the x, y and z orbitals having p-like symmetry) and $\rho = \uparrow, \downarrow$. The atoms l are denoted by $l = c$ for a cation and $l = a$ an anion. We note that in the nearest neighbour approximation two types of matrix elements will be non-zero, the diagonal on-site matrix elements and the off-diagonal interatomic matrix elements. The on-site matrix elements are the self energies of a given orbital α on a particular atom, these are related to the energies will be related to those of an isolated atom with some changes due to the effect of other atoms. The self energies can be defined as

$$H_{\beta n\rho,\alpha l\rho}(\mathbf{k}) = E_\alpha \delta_{\alpha\beta} \tag{2.11}$$

The off-diagonal elements characterised by interaction between orbitals on different atoms, are called hopping matrix elements. Taking the cation ($l = c$) to sit at the origin of a Cartesian coordinate system, the bond vectors to its four nearest-neighbour anions ($l = a$) are given by

$$\mathbf{d}_1 = \frac{a}{4}(-\widehat{x} - \widehat{y} - \widehat{z}) \tag{2.12}$$

$$\mathbf{d}_2 = \frac{a}{4}(\widehat{x} + \widehat{y} - \widehat{z}) \tag{2.13}$$

$$\mathbf{d}_3 = \frac{a}{4}(\widehat{x} - \widehat{y} + \widehat{z}) \tag{2.14}$$

$$\mathbf{d}_4 = \frac{a}{4}(-\widehat{x} + \widehat{y} + \widehat{z}) \tag{2.15}$$

where a is the lattice constant. Each of these bond vectors has three direction cosines associated with them, defined with respect to the x-, y- and z-axes by

$$l_j = \widehat{x} \cdot \widehat{d_j} \tag{2.16}$$

$$m_j = \widehat{y} \cdot \widehat{d_j} \tag{2.17}$$

$$n_j = \widehat{z} \cdot \widehat{d_j} \tag{2.18}$$

where j is a nearest neighbour and $\widehat{d_j}$ is a unit vector along the direction of the bond vector $\mathbf{d}_j$ to that neighbour. Using Eq. (2.12-2.18) in the tight-binding Hamiltonian Eq. (2.10), we find that the matrix elements of the sp^3s^* Hamiltonian in the nearest-neighbour approximation are

$$H_{\beta c\rho',\alpha a\rho}(\mathbf{k}) = \sum_{j=1}^{4} e^{i\mathbf{k}\cdot\mathbf{d}_j} \langle \phi_{\beta c\rho'}(k)|\widehat{H}|\phi_{\alpha_j a\rho'}(k)\rangle \tag{2.19}$$

where $\langle\phi_{\beta c\rho'}(k)|$ denotes the cation atomic orbital β with spin ρ', and $\phi_{\alpha_j a\rho'}(k)\rangle$ is the anion atomic orbital α at the nearest-neighbour atom site j with spin ρ and bond vector $\mathbf{d}_j$. The final step in the evaluation of the crystal Hamiltonian is finding the matrix elements $\langle\phi_{\beta c\rho'}(k)|\widehat{H}|\phi_{\alpha_j a\rho'}(k)\rangle$. We can define the interaction matrix elements as[92, 95, 97]

- $V_{ss\sigma}$ - the interaction of two s orbitals on nearest neighbour atoms
- $V_{s_a p_c\sigma}$ and $V_{s_c p_a\sigma}$ - the interaction of between s and p orbitals on nearest neighbour atoms
- $V_{s^*_a p_c\sigma}$ and $V_{s^*_c p_a\sigma}$ - the interaction of between s^* and p orbitals on nearest neighbour atoms
- $V_{pp\sigma}$ - the interaction of two p orbitals on nearest neighbour atoms via a σ bond
- $V_{pp\pi}$ - the interaction of two s orbitals on nearest neighbour atoms via a π bond

Other possible interactions such as $V_{ss^*\sigma}$ and $V_{s^*s^*\sigma}$ are assumed to be zero and are therefore excluded, which is based on the setup described by Vogl et al. to ensure s^* orbitals interact exclusively with p orbitals[96]. As stated earlier the s^* orbitals have been included to correct the CB structure away from the zone centre, while not affecting the VB structure significantly[92].

In Eq. (2.19) we evaluate the matrix elements $\langle\phi_{\beta c\rho'}(k)|\widehat{H}|\phi_{\alpha_j a\rho'}(k)\rangle$, by considering the projections of the sp and pp interactions in terms of the $sp\sigma$, $pp\sigma$ and $pp\pi$ interactions. We do this by breaking the p orbitals into its components parallel (σ interactions) and perpendicular (π interactions) to the bond vector ($\mathbf{d}_j$) for a given nearest-neighbour interaction. With $\widehat{n}_j$ as a unit vector perpendicular to $\widehat{d_j}$, and $\widehat{p}_j$ as a unit vector along the direction of the p orbital (p = x, y, z) at nearest-neighbour atom j, we can calculate the sp interactions as

$$\begin{aligned}\langle\phi_{sc\rho'}(k)|\widehat{H}|\phi_{pa\rho}(k)\rangle &= (\widehat{p_j}\cdot\widehat{d_j})\langle\phi_{sc\rho'}(k)|\widehat{H}|\phi_{p_j^{(d)}a\rho}(k)\rangle + (\widehat{p_j}\cdot\widehat{n_j})\langle\phi_{sc\rho'}(k)|\widehat{H}|\phi_{p_j^{(n)}a\rho}(k)\rangle \\ &= \left((\widehat{p_j}\cdot\widehat{d_j})V_{s_c p_a\sigma} + (\widehat{p_j}\cdot\widehat{n_j})V_{s_c p_a\pi}\right)\delta_{\rho'\rho}\end{aligned} \tag{2.20}$$

where $V_{s_c p_a \sigma} = \langle \phi_{sc\rho'}(k)|\widehat{H}|\phi_{p_j^{(d)} a\rho}(k)\rangle$ and $V_{s_c p_a \pi} = \langle \phi_{sc\rho'}(k)|\widehat{H}|\phi_{p_j^{(n)} a\rho}(k)\rangle$, however, the final term is 0 due to the spherical symmetry of the s orbital, $V_{s_c p_a \pi} = 0$. The dot product $\widehat{p}_j \cdot \widehat{d}_j$ is a direction cosine and is equal to l_j, m_j or n_j for $p = x, y$ or z (Eqs. 2.13 – 2.16). A similar derivation for the pp interactions gives

$$\langle \phi_{pc\rho'}(k)|\widehat{H}|\phi_{pa\rho}(k)\rangle = \Big((\widehat{p}\cdot\widehat{p_j})V_{pp\pi} + (\widehat{p}\cdot\widehat{d_j})(\widehat{p_j}\cdot\widehat{d_j})(V_{pp\sigma} - V_{pp\pi})\Big)\,\delta_{\rho'\rho} \tag{2.21}$$

where $\widehat{p}$ and $\widehat{p}_j$ are the unit vectors along the direction of the p orbital on the cation and its j^{th} nearest neighbour, respectively. Eqs. (2.21) and (2.22) describe the interactions between the s and p orbitals on neighbouring atoms, originally derived by Slater and Koster[97] and referred to as the two-centre integrals.

With the two-centre integrals we can calculate the matrix elements in Eq. (2.16) and we find that the 20×20 matrix representation H of the crystal Hamiltonian $\widehat{H}$ in the sp^3s^* basis is then given by[92, 95]

$$H(\mathbf{k}) - H_{SO} = \begin{pmatrix} E_c & V_{ca}(\mathbf{k}) & 0 & 0 \\ & E_a & 0 & 0 \\ & & E_c & V_{ca}(\mathbf{k}) \\ & & & E_a \end{pmatrix} \begin{matrix} |\phi_{\alpha c\uparrow}(k)\rangle \\ |\phi_{\alpha a\uparrow}(k)\rangle \\ |\phi_{\alpha c\downarrow}(k)\rangle \\ |\phi_{\alpha a\downarrow}(k)\rangle \end{matrix} \tag{2.22}$$

where each entry represents a square 5×5 block ($\alpha = s^*, s, x, y, z$). While not shown in this matrix the below-diagonals can be obtained from the above-diagonals via complex conjugation. In Eq. (2.19) we do not include the matrix elements of the spin-orbit interaction (H_{SO}) for now. The onsite orbital energies are included in the 5×5 matrices $E_l (l = c, a)$.

$$E_c = \begin{pmatrix} E_{s_c^*} & 0 & 0 & 0 & 0 \\ & E_{s_c} & 0 & 0 & 0 \\ & & E_{p_c} & 0 & 0 \\ & & & E_{p_c} & 0 \\ & & & & E_{p_c} \end{pmatrix} \begin{matrix} |\phi_{s^*c\rho}\rangle \\ |\phi_{sc\rho}\rangle \\ |\phi_{xc\rho}\rangle \\ |\phi_{yc\rho}\rangle \\ |\phi_{zc\rho}\rangle \end{matrix} \tag{2.23}$$

The inter-atomic interactions between orbitals on neighbouring atoms are included in the 5×5 matrix $V_{ca}(\mathbf{k})$ appearing in the off-diagonal blocks of Eq. (2.22).

The non-zero elements of the 20×20 matrix H_{SO} of the spin-orbit coupling in the same sp^3s^* basis as in Eqs. (2.19) and (2.20) are calculated in terms of the matrix elements $\Delta_l \equiv 3\langle \phi_{xc\uparrow}(k)|\widehat{H}_{SO}|\phi_{zc\downarrow}(k)\rangle$ and included in the Hamiltonian following the formalism of Chadi et al.[98] and are given as

$$\langle x_l;\uparrow|\widehat{H}_{SO}|y_l;\uparrow\rangle = -i\frac{\triangle_l}{3} \tag{2.24}$$

$$\langle x_l;\downarrow|\widehat{H}_{SO}|y_l;\downarrow\rangle = i\frac{\triangle_l}{3} \tag{2.25}$$

$$\langle x_l;\uparrow|\widehat{H}_{SO}|z_l;\downarrow\rangle = \frac{\triangle_l}{3} \tag{2.26}$$

$$\langle y_l;\uparrow|\widehat{H}_{SO}|z_l;\downarrow\rangle = -i\frac{\triangle_l}{3} \tag{2.27}$$

$$\langle z_l;\uparrow|\widehat{H}_{SO}|x_l;\downarrow\rangle = -\frac{\triangle_l}{3} \tag{2.28}$$

$$\langle z_l;\uparrow|\widehat{H}_{SO}|y_l;\downarrow\rangle = i\frac{\triangle_l}{3} \tag{2.29}$$

2.2.2 Alloy supercell calculations

With the tight-binding model derived for a two-atom unit cell we now turn to the calculation of the electronic structure for large supercells with up to 10^3 atoms. We require supercells with such large numbers of atoms in order to accurately predict the behaviour of atomistic effects, such as local alloy disorder, in the alloys we are interested. As an example we will discuss calculations on an N atom $Ge_{1-x}C_x$ alloy supercell, to generate this supercell we create an N atom Ge supercell before randomly selecting some sites to replace the Ge atom with a C atom. We do this for M C atoms giving a $Ge_{N-M}C_M$ supercell with a C composition $x = \frac{M}{N}$. Having generated the alloy supercell with a composition x, we must now relax the atomic positions in order to accurately describe the electronic properties of the alloy[99], as up to this point the supercells atomic positions remain that of the Ge host matrix. This relaxation is performed using a valence force field (VFF) model based on the Keating potential[100, 101], and implemented in the GULP and LAMMPS software libraries. This VFF approach takes into account changes in both bond length and bond angle, providing an accurate description of the local relaxation of the crystal lattice expected in real alloys. We denote the unrelaxed and relaxed bond vectors between the atoms at neighbouring atomic sites i and j by $\mathbf{d}_{ij}^{(0)}$ and $\mathbf{d}_{ij}^{(1)}$ respectively. $d_{ij}^{(0)} = |\mathbf{d}_{ij}^{(0)}|$ is the equilibrium bond length of the binary compound formed by atoms i and j and is given by $d_{ij}^{(0)} = \frac{\sqrt{3}}{4}a(ij)$, where $a(ij)$ is the equilibrium lattice constant of the binary compound formed by atoms i and j.

Our semi-empirical description of the structural and elastic properties of group-IV alloys is based on a nearest-neighbour VFF potential. The VFF potential we employ is that originally introduced by Musgrave and Pople[102], as later modified by Martin[103]. We consider this potential in its non-polar form, whereby the contribution to the lattice free energy associated with an atom located at site i is given by

$$
\begin{aligned}
V_i = & \frac{1}{2}\sum_j \frac{k_r}{2}\left(r_{ij} - r_{ij}^{(0)}\right)^2 \\
& + \sum_j \sum_{k>j} \left[\frac{k_\theta}{2} r_{ij}^{(0)} r_{ik}^{(0)} \left(\theta_{ijk} - \theta_{ijk}^{(0)}\right)^2 \right. \\
& + k_{rr}\left(r_{ij} - r_{ij}^{(0)}\right)\left(r_{ik} - r_{ik}^{(0)}\right) \\
& \left. + k_{r\theta}\left(r_{ij}^{(0)}\left(r_{ij} - r_{ij}^{(0)}\right) + r_{ik}^{(0)}\left(r_{ik} - r_{ik}^{(0)}\right)\right)\left(\theta_{ijk} - \theta_{ijk}^{(0)}\right)\right]
\end{aligned}
\tag{2.30}
$$

where the indices j and k describe the nearest-neighbour atoms of atom i. The unstrained (equilibrium) and relaxed bond lengths between atoms i and j are denoted respectively by $r_{ij}^{(0)}$ and r_{ij}; $\theta_{ijk}^{(0)}$ and θ_{ijk} respectively denote the unstrained and relaxed angles between the adjacent nearest neighbour bonds formed by atoms i and j, and i and k. The first and second terms in Eq. (2.45) respectively describe contributions to the lattice free energy associated with pure bond stretching (changes in r_{ij}) and pure bond-angle bending (changes in θ_{ijk}), while the third and fourth terms are "cross terms" which respectively describe the impact of changes in r_{ik} on r_{ij}, and the impact of changes in θ_{ijk} on both r_{ij} and r_{ik}. By re-casting the lattice free energy expressed in Eq. (2.45) in terms of macroscopic and internal strains, and inverting the associated derived expressions for the elastic constants C_{11}, C_{12} and C_{44}, and Kleinman (internal strain) parameter ζ, expressions describing the force constants k_r, k_θ, k_{rr} and $k_{r\theta}$ explicitly in terms of C_{11}, C_{12}, C_{44}, ζ and the equilibrium bond length $r^{(0)}$ can then be derived[104]. These analytical relationships circumvent the conventional requirement to perform numerical fitting to determine the force constants, and provide an exact description of the static lattice properties of the constituent materials. To perform structural relaxations for alloy supercells this VFF potential was implemented using either the General Utility Lattice Program (GULP)[105–107] for $Ge_{1-x}C_x$ or the Large-scale Atomic/Molecular Massively Parallel Simulator (LAMMPS)[108, 109] for $Ge_{1-x}Sn_x$.

After relaxing the atomic positions we can now move forward to calculate the sp^3s^* Hamiltonian for the supercell. As before we have ten orbitals per atom in the sp^3s^* model (including spin-orbit coupling), therefore the Hamiltonian for the supercell containing N atoms will be a $10N \times 10N$ matrix. The overall form of this matrix will be similar to Eq. (2.22) with two 5×5 blocks containing the orbital energies for each atom. However, when dealing with an alloy we must take into account the fact that the four nearest neighbours of a particular atom may not be of the same species. Therefore, when calculating the orbital energies of an atomic site i we average over the orbital energies of the binary compounds formed by atom i and its four nearest-neighbour atoms j, and include the valence band offsets ΔE_v between each of these binary compounds. The spin-degenerate energy of the $|\phi_{\alpha l\rho}^{(i)}\rangle$ orbital on atomic site i is calculated as

$$
E_{\alpha l}^{(i)} = \frac{1}{4}\sum_{j=1}^{4}\left(\triangle E_v^{(ij)} + E_{\alpha l}^{(ij)}\right) \tag{2.31}
$$

where the sum runs over the nearest neighbours j of atom i and $\Delta E_v^{(ij)}$ is the valence band offset and $E_{\alpha l}^{(ij)}$ is the energy of the orbital α for the compound formed by atoms i and j.

Up to now our calculation of the orbital energies has neglected to include the effect of strain produced due to the deviation of $\mathbf{d}_{ij}^{(1)}$ from $\mathbf{d}_{ij}^{(0)}$. Several methods have been developed for the incorporation of strain that describe the variation of the band edge energies with strain well in alloy supercells and in atomistic calculations of quantum-confined heterostructures[110–112]. However, they require a large number of additional parameters that makes parameterisation of the Hamiltonian more difficult. In this thesis we include the strain-induced change in the band edge energies via a bond length scaling term in the calculation of the inter-atomic interaction matrix elements. The scaling is $\left(\frac{\mathbf{d}_{ij}^{(0)}}{\mathbf{d}_{ij}^{(1)}}\right)^{\eta}$ and affects each type of inter-atomic interaction (i.e. $V_{ss\sigma}$, $V_{pp\pi}$, $V_{s_c p_a \sigma}$, etc.), it is included by multiplication with the interaction parameter for each compound in the supercell. Included in this bond length scaling term is a parameter η, that is parameterised for inter-atomic interaction, with the value of η for each binary compound by fitting the strain-induced variations of the band edge energies to a range of hydrostatic deformation potentials, that are found using experimental measurements or ab initio calculations[113].

The off-diagonal 5×5 blocks $V_{ca}(\mathbf{k})$ of Eq. (2.19) that include the contribution of the coupling between orbitals on adjacent atoms to Hamiltonian appear in the form of four independent 5×5 blocks coupling the atomic orbitals on site i to those on each of its nearest neighbours j. For the full supercell these must be modified to include the fact that the nearest neighbours j of atom i may not be of the same species, leading to differences in the interaction matrix elements depending on the nearest neighbour environment in the supercell. With these changes the 5×5 blocks describing the inter-atomic interactions between the orbitals $|\phi_{\alpha_j a\rho}\rangle$ on atomic site i and the orbitals $|\phi_{\beta^{(j)} c\rho'}\rangle$ on each of its nearest-neighbour atoms j, are given by

$$V^{(i,j)}_{\beta,\rho' l',\alpha\rho l}\left(\mathbf{k}\right) = e^{i\mathbf{k}\cdot\mathbf{d}_{ij}^{(1)}} \langle \phi_{\beta^{(j)} c\rho'} | \widehat{H} | \phi_{\alpha_j a\rho} \rangle \tag{2.32}$$

which is a more general form of Eq. (2.19). The matrix elements of the above equation, $\langle \phi_{\beta^{(j)} c\rho'} | \widehat{H} | \phi_{\alpha_j a\rho} \rangle$, are determined in a similar fashion as for the two atom unit cell, but with the added multiplication by the bond-length scaling term. The Hamiltonian for a typical supercell $H_{SC}(\mathbf{k})$ is given in Eq.(2.33) without the spin-orbit coupling terms. The band structure of the crystal is then determined by diagonalising the Hamiltonian after the spin-orbit interactions have been added.

$$
H_{SC}(\mathbf{k}) - H_{SO} = \begin{array}{c}
\begin{array}{ccccccccccc}
|\phi_{\beta c\uparrow c^{\uparrow}}^{(1)}\rangle & |\phi_{\beta a\uparrow}^{(2)}\rangle & \dots & |\phi_{\beta c\uparrow}\hat{(}N-1)\rangle & |\phi_{\beta a\uparrow}^{(N)}\rangle & |\phi_{\beta c\downarrow}^{(1)}\rangle & |\phi_{\beta a\downarrow}^{(2)}\rangle & \dots & |\phi_{\beta c\downarrow}^{(N-1)}\rangle & |\phi_{\beta a\downarrow}^{(N)}\rangle & \\
E_c^{(1)} & V_{\beta\uparrow a,\alpha\uparrow c}^{(1,2)}(\mathbf{k}) & \dots & 0 & V_{\beta\uparrow a,\alpha\uparrow c}^{(1,N)}(\mathbf{k}) & 0 & 0 & \dots & 0 & 0 & |\phi_{\alpha c\uparrow}^{(1)}\rangle \\
 & E_a^{(2)} & \dots & V_{\beta\uparrow c,\alpha\uparrow a}^{(2,N-1)}(\mathbf{k}) & 0 & 0 & 0 & \dots & 0 & 0 & |\phi_{\alpha a\uparrow}^{(2)}\rangle \\
 & & \ddots & \vdots & \vdots & 0 & 0 & \dots & 0 & 0 & \vdots \\
 & & & E_c^{(N-1)} & V_{\beta\uparrow a,\alpha\uparrow c}^{(N-1,N)}(\mathbf{k}) & 0 & 0 & \dots & 0 & 0 & |\phi_{\alpha c\uparrow}^{(N-1)}\rangle \\
 & & & & E_a^{(N)} & 0 & 0 & \dots & 0 & 0 & |\phi_{\alpha a\uparrow}^{(N)}\rangle \\
 & & & & & E_c^{(1)} & V_{\beta\downarrow a,\alpha\downarrow c}^{(1,2)}(\mathbf{k}) & \dots & 0 & V_{\beta\downarrow a,\alpha\downarrow c}^{(1,N)}(\mathbf{k}) & |\phi_{\alpha c\downarrow}^{(1)}\rangle \\
 & & & & & & E_a^{(2)} & \dots & V_{\beta\downarrow c,\alpha\downarrow a}^{(2,N-1)}(\mathbf{k}) & 0 & |\phi_{\alpha a\downarrow}^{(2)}\rangle \\
 & & & & & & & \ddots & \vdots & \vdots & \vdots \\
 & & & & & & & & E_c^{(N-1)} & V_{\beta\downarrow a,\alpha\downarrow c}^{(N-1,N)}(\mathbf{k}) & |\phi_{\alpha c\downarrow}^{(N-1)}\rangle \\
 & & & & & & & & & E_a^{(N)} & |\phi_{\alpha a\downarrow}^{(N)}\rangle
\end{array}
\end{array}
\tag{2.33}
$$

2.3 Transport calculations

In the course of this work we set out to calculate the transport properties of GeSn alloys, in order to investigate the impact of Sn incorporation on band to band tunneling. We seek to analyse this impact for possible application of GeSn in tunneling fields effect transistors (TFETs) where band-to-band tunneling (BTBT) is the main current path and the impact on GeSn photodetectors where BTBT represents a detrimental effect that increases the dark current. Many possible methods exist for transport calculations, such as effective mass approximation and the WKB approximation. Our selection is motivated by the need to include atomistic effects such as disorder and band mixing, therefore we use the non-equilibrium Green's function (NEGF) method to calculate the transport properties of GeSn wires. The NEGF method allows us to efficiently calculate the transport properties of large bulk like structures containing thousands of atoms and further allows us to calculate the electrical properties of TFET structures. In this section we provide an outline of the NEGF method as implemented in the OMEN software, which is used in this thesis.

2

2.3.1 Open boundary conditions (OBC) and complex band structure

As a first step towards calculating the transport properties we must set the transport problem. We start by considering the atomic structure: following the layout of Schulman et al. [114] we work in a slab basis. A slab consists of the minimum number of atomic planes that can be used to repeat the structure along the transport direction. In the case of a [100] structure the minimum number of planes is four. Transport occurs along the x direction and each of the ends are connected to semi-infinite reservoirs from/to which charge carriers are injected. We use the sp^3s^* TB model from section 2.2 with spin-orbit coupling included. Eventually we wish to solve the time independent Schrödinger equation using open boundary conditions. For our devices we have an electrons injected from the source on the left of our nanowires, having an energy E relative to the VB. These injected electrons can then be transmitted through the nanowire. The Schrödinger equation is written as

$$H|\psi\rangle = E|\psi\rangle \tag{2.34}$$

where H is the Hamiltonian and $|\psi_E\rangle$ are the wave fucntions, we can expand these in terms of atomic orbitals $\phi_\alpha(\mathbf{r})$ of type α (s, p, or excited s^*)

$$\psi(E) = \sum_{\alpha,i} C_i^\alpha(E)\phi_\alpha(\mathbf{r} - \mathbf{r_i}) \tag{2.35}$$

where the atomic orbitals $\phi_\alpha(\mathbf{r})$ are orthogonal to each other and the sum runs over the atomic orbitals and the positions of the atoms in the slab basis. $C_i^\alpha(E)$ are the coefficients for the orbital

α at an atomic site i with a position r_i. As mentioned above we work in a slab basis, where each slab has a width Δ and there are a total L/Δ slabs in a nanowire of length L.

Moving into this slab basis the scalar coefficients $C_i^{\alpha}(E)$ become vectors of the form $C_i(r_i, E)$, where now i is the i^{th} slab in the nanowire and r_i is the position of an orbital in the slab. Left-multiplying Eq. (2.34) with $\langle\phi_{\alpha i}|$ we obtain the matrix equations

$$(E - H_{ii})C_i(r_i, E) - H_{ii+1}C_{i+1}(r_i, E) - H_{ii-1}C_{i-1}(r_i, E) = 0 \tag{2.36}$$

We have assumed here that only nearest-neighbour interactions are included. As before we are using the sp^3s^* TB model where we have 10 orbitals per atom with spin-orbit coupling. We now rewrite this equation in a simpler form using some new notation

$$(D_{ii})C_i(r_i, E) + T_{ii+1}C_{i+1}(r_i, E) + T_{ii-1}C_{i-1}(r_i, E) = 0 \tag{2.37}$$

whose elements $E - H_{ii} \equiv D_{ii}$ describes the on-site energy in a slab i and also the interactions between neighbouring atoms within slab i, $H_{ii+1} \equiv -T_{ii+1}$ contains the nearest-neighbour interactions between atoms in slab i and slab $i+1$, and $H_{ii-1} \equiv -T_{ii-1}$ contains the nearest-neighbour interactions between atoms in slab i and slab $i-1$. Each slab contains N atoms, therefore the matrices in the above equation are of the size $10 \times N$. Not only is the above equation valid in the nanowire slabs but also in the left and right contacts, looking at the injected electrons in the left contact we write an ansatz equation for the coefficients $C_i(r_i, E)$ as

$$C_i(r_i, E) = \frac{1}{\sqrt{A}} \sum_n [a_n e^{ik_n(E)x} \varphi_{i,n}^{+}(r_i, E) + b_n e^{-ik_n(E)x} \varphi_{i,n}^{-}(r_i, E)] \tag{2.38}$$

Here A is a normalization constant, a_n is the injection coefficient for a state $\varphi_{i,n}^{+}(r_i, E)$ transmitted through the device (i.e., flowing from left to right), and b_n is the coefficient for a state $\varphi_{i,n}^{-}(r_i, E)$ reflected back in the contact, respectively. $\varphi_{i,n}^{\pm}(r_i, E)$ (associated with $e^{ik_n(E)x_i}$) is the n^{th} reservoir state and can be propagating or exponentially decaying. Inserting Eq. (2.38) into Eq. (2.37) and separating the transmitted and the reflected parts of the coefficient $C_i(r_i, E)$, we exploit the fact that both resulting contributions must vanish for each quantization level n since the contacts are assumed infinite, to get

$$(D_{ii} + T_{ii+1}e^{\pm ik_n(E)\Delta} + T_{ii-1}e^{\mp ik_n(E)\Delta})\varphi_{i,n}^{\pm}(r_i, E) = 0 \tag{2.39}$$

with Δ the slab width. It is worth noting that Eq. (2.39) is exactly the equation solved for the band-structure calculation of an infinite wire, but with exchanged input and output variables. In the open boundary condition problem, one searches for all the wave vectors k corresponding to one injection energy E. A well established procedure consists in transforming Eq. (2.39) to the a complex non-Hermitian generalized eigenvalue problem[115, 116] of size $2 \times 10 \times N$

$$\begin{pmatrix} D_{ii} & T_{ii+1} \\ I & 0 \end{pmatrix} \begin{pmatrix} \varphi_i \\ \varphi_{i+1} \end{pmatrix} = e^{ik\Delta} \begin{pmatrix} -T_{ii-1} & 0 \\ 0 & I \end{pmatrix} \begin{pmatrix} \varphi_i \\ \varphi_{i+1} \end{pmatrix} \tag{2.40}$$

where we have dropped the variables E and r_i. Eq. (2.40) enables us to determine the complex bandstructure of a slab with a width Δ, and can be solved using a generalised eigenvalue approach.

2.3.2 Non-equilibrium Green's function method

After determining the OBCs we now turn to solving the transport problem for which we use the NEGF formalism that consists in solving the following system of equations for electrons or holes [117]

$$(\mathbf{E} - \mathbf{H}(k) - \mathbf{V} - \mathbf{\Sigma}^{RB}(E,k)) \cdot \mathbf{G}^{R}(E,k) = \mathbf{I} \tag{2.41}$$

$$\mathbf{G}^{<}(E,k) = \mathbf{G}^{R}(E,k) \cdot (\mathbf{\Sigma}^{<B}(E,k)) \cdot \mathbf{G}^{A}(E,k) \tag{2.42}$$

where the unknowns are the retarded $\mathbf{G}^{R}(E,k)$ and the lesser $\mathbf{G}^{<}(E,k)$ Green's functions at energy E and momentum k. They are matrices of size $N_A \times N_{orb}$ where N_A is the number of atoms composing the simulation domain and N_{orb} the number of orbitals describing the properties of each atom. The terms $\Sigma^{RB}(E,k)$ and $\Sigma^{<B}(E,k)$ account for losses in the device due to coupling to the contacts and inscattering from the contacts respectively.

The single elements of the retarded $G_{ij}^{R\sigma_1\sigma_2}(E,k)$ and lesser $G_{ij}^{<\sigma_1\sigma_2}(E,k)$ Green's Functions represent the coupling or correlation between two orbitals σ_1 and σ_2 situated on two atoms i and j. The diagonal matrix $\mathbf{E}$ contains the electron/hole energy E, $\mathbf{I}$ is the identity matrix, $\mathbf{H}(k)$ refers to the device Hamiltonian matrix, which includes the orbital on-site energies as well as the coupling elements between different orbitals and atoms ($H_{ij}^{\sigma_1\sigma_2}$). The entries of the diagonal matrix $\mathbf{V}$ are the electrostatic potential at each atomic site. The open boundary conditions are cast into the matrices $\mathbf{\Sigma}^{RB}(E,k)$ and $\mathbf{\Sigma}^{<B}(E,k)$.

Equations (2.35)-(2.36), which have the form "$A \cdot B = C$", must be solved for each possible energy E and momentum k. This can be done with a recursive Green's Function (RGF) algorithm instead of directly inverting or multiplying large matrices.

The equation of motion for $G^{<}$ is written as [118]

$$(E - H_0^D - \Sigma^{RB})G^{<} = \Sigma^{<B}G^{A} \tag{2.43}$$

where $E - H_0^D$ is an $N \times N$ block tridiagnoal matrix and the matrices Σ^{RB} and $\Sigma^{<B}$ are $N \times N$ matrices with two non-zero blocks, one in the upper left corner and the other in the lower right corner. On the left side of Eq. (2.43), $E - H_0^D - \Sigma^{RB}$ is $G^{R^{-1}}$[118]. Therefore we also get an equation of motion for the retarded Green function in the device

$$(E_{H0}^{D} - \Sigma^{RB})G^{R} = 1 \tag{2.44}$$

For our calculations the retarded Green function can be represented as

$$[G^{R}] = \begin{bmatrix} D_1 - \Sigma_{1,1}^{RB} & T_{1,2} & 0 & 0 \\ T_{2,1} & D_2 & \ddots & 0 \\ 0 & \ddots & \ddots & T_{N-1,N} \\ 0 & 0 & T_{N,N-1} & D_N - \Sigma_{N,N}^{RB} \end{bmatrix}^{-1} \tag{2.45}$$

following the notation of Eq. (2.39). The remaining unknowns here are the self-energies $\Sigma_{1,1}^{RB}$ and $\Sigma_{N,N}^{RB}$. From ref. [118] we have

$$\Sigma_{1,1}^{RB} = T_{1,0} g_{0,0}^{R} T_{0,1} \tag{2.46}$$

and

$$\Sigma_{N,N}^{RB} = T_{N,N+1} g_{N+1,N+1}^{R} T_{N+1,N} \tag{2.47}$$

Where lower case g^R posses the same structure as the upper case G^R except the boundary matrices $T_{0,1}$, $T_{1,0}$, $T_{N+1,N1}$ and $T_{N,N+1}$ are set to zero. To determine the self energies $\Sigma_{1,1}^{RB}$ and $\Sigma_{N,N}^{RB}$ we require $g_{0,0}^{R}$ and $g_{N+1,N+1}^{R}$. For the left semi infinite lead we can write $g_{0,0}^{R}$

$$g_{0,0}^{R} = \begin{bmatrix} D_{-M} - \Sigma_{-M,-M}^{RB} & T_{-M,-M+1} & 0 & 0 \\ T_{-M+1,-M} & \ddots & \ddots & 0 \\ 0 & \ddots & D_{-1} & T_{1,0} \\ 0 & 0 & T_{0,-1} & D_0 \end{bmatrix}^{-1} \tag{2.48}$$

with $\Sigma_{-M,-M}^{RB}$ given by

$$\Sigma_{-M,-M}^{RB} = T_{-M,-M-1} g_{-M-1,-M-1}^{R} T_{-M-1,-M} \tag{2.49}$$

Here, M represents the layer which the potential becomes constant for successive layers out to $-\infty$. $g_{-M-1,-M-1}^{R}$ is the surface Green function of the semi infinite contact terminated at layer $-M$. From ref. [118] in the nearest neighbour TB model the surface Green function is

$$g_{-M-1,-M-1}^{R} = [D_{-M} + T_{-M-1,-M-1} \phi Z \phi^{-1}]^{-1} \tag{2.50}$$

and the boundary self energy is

$$\Sigma_{-M,-M}^{RB} = T_{-M-1,-M} \phi Z \phi^{-1} \tag{2.51}$$

where Z is the diagonal matrix of propagation factors and ϕ is the matrix of Bloch states propagating toward the device. A similar procedure can used for the right contact to derive $g^R_{N+1,N+1}$ and hence $\Sigma^{RB}_{N,N}$. With $g^R_{0,0}$ found the rest of the recursive Green function G^R can now be calculated recursively using[118]

$$G^R_{L,L} = g^R_{L,L} + g^R_{L,L} T_{L,L-1} G^R_{L-1,L-1} T_{L,L} g^R_{L,L} \tag{2.52}$$

2.3.3 Wave function method

While the NEGF method enables accurate calculation of the transport properties it has the draw back of being computationally expensive. A more efficient method can be found in the wave function formalism. The form implemented in the OMEN software is the renormalization method of Grosso et al[119] with some optimisations. Working in the same slab basis as the NEGF method from section 2.3.2 we write the Schrödinger equation for a transmission problem with L layers as as[120–123]

$$\begin{pmatrix} \bar{H}_{1,1} + \bar{\Sigma}_1 - \bar{1}E & \bar{H}_{1,2} & - & \cdots & \bar{0} \\ \bar{H}^\dagger_{1,2} & \bar{H}_{2,2} - \bar{1}E & \bar{H}_{2,3} & \bar{0} & \bar{0} \\ \bar{0} & \ddots & \ddots & \ddots & \bar{0} \\ \vdots & \ddots & \ddots & \ddots & \bar{H}_{L-1,L} \\ \bar{0} & \cdots & \bar{0} & \bar{H}^\dagger_{L-1,L} & \bar{H}_{L,L} + \bar{\Sigma}_L - \bar{1}E \end{pmatrix} \begin{pmatrix} \bar{C}_1 \\ \bar{C}_2 \\ \vdots \\ \vdots \\ \bar{C}_L \end{pmatrix} = \begin{pmatrix} \bar{V}_I \\ \bar{0} \\ \vdots \\ \vdots \\ \bar{0} \end{pmatrix} \tag{2.53}$$

where $\bar{\Sigma}_1$ and $\bar{\Sigma}_L$ are the self energies that couple the first and last layers of the nanowire structure to the semi-infinite contact regions on either side of the nanowire. The orbital coefficients of the jth layer are contained in the vectors $\bar{C}_j$ and the vector $\bar{V}_I$ represents the injection from the left contact.

To proceed two properties of the nearest neighbour tight-binding model with Chadi's description[91] of the spin-orbit interaction are used. First is that in the nearest neighbour orthogonal tight-binding model the only interatomic coupling is between anions and cations. There are no anion-anion or cation-cation matrix elements. Second, when the spin-orbit interaction is included using Chadi's model[91], the only complex submatrices are the diagonal blocks, with no interactions between orbitals of different spin.

Another important property of the structure used in the wave function method is the geometry of a zinc blende crystal. When the zinc blende structure is oriented in the [100], the atom will be organised such as to from plane normal to [100] direction. In each of these planes there will be a single type of atom, either an anion or a cation. As such atoms in each plane only interact with atoms in neighbouring planes. With no in-plane interactions, we can simplify the blocks in Eq. (2.53), denoting the atomic planes n=1,2,...,N, $N = 4L$, the diagonal blocks take the form[124]

$$\bar{H}_{l,l} = \begin{pmatrix} H'_{4l-3,4l-3} & H_{4l-3,4l-2} & 0 & 0 \\ H^{\dagger}_{4l-3,4l-2} & H_{4l-2,4l-2} & H_{4l-2,4l-1} & 0 \\ 0 & H^{\dagger}_{4l-2,4l-1} & H_{4l-1,4l-1} & H_{4l-1,4l} \\ 0 & & H^{\dagger}_{4l-1,4l} & H'_{4l,4l} \end{pmatrix} \tag{2.54}$$

where l= 1,2, ...,L and the matrices $H_{p,p}$ denote single-atomic plane blocks. $H_{p,p}$ will have the same form throughout the nanowire except for the first and last blocks as these incorporate the open boundary conditions which only affect the first and last planes of the nanowire, where they have the form $H'_{1,1} = H_{1,1} + \Sigma_1$ and $H'_{4L,4L} = H'_{4L,4L} + \Sigma_{4L}$. The self-energies Σ_p incorporate the open-system boundary conditions therefore the first and last diagonal blocks are non-Hermitian. When the spin-orbit interaction is neglected, the diagonal blocks of Eq. (2.54), $H_{p,p}$, are real and diagonal. Where they only contain the orbital same atom parameters. The off-diagonal blocks in Eq. (2.53) are[124]

$$\bar{H}_{l,l+1} = \begin{pmatrix} 0 & 0 & 0 & 0 \\ 0 & 0 & 0 & 0 \\ 0 & 0 & 0 & 0 \\ H_{4l,4l+1} & 0 & 0 & 0 \end{pmatrix}, l = 1, 2, ..., (L-1), \tag{2.55}$$

for two adjacent layers l and $l+1$, the only coupling is between the last plane of layer l and the first plane of layer $l+1$. The dimension of the block matrices in Eq. (2.54) and Eq. (2.55) are $10 \times N_{orb}$, where N is the number of atoms in a plane and 10 is the number of orbitals per atom with spin orbit coupling.

With the Hamiltonian defined in this manner we can now proceed to the renormalization method[125] that forms the key part of the wave function method. When spin-orbit is included in Eq. (2.53), the majority of the system is real. As we shall see below, the renormalization method[125] allows us to take advantage of these properties to efficiently solve the Hamiltonian. The renormalization method[125] involves the decoupling of each atomic plane from its neighbouring planes, that will then allow efficient calculation of the Hamiltonian. This process involves the transformation of the existing Hamiltonian to a new from while keeping the wave functions unchanged. An interior plane p ($p \neq 1, 4L$) is decoupled by

$$H = M^{-1}_{L,p} \widetilde{H} M^{-1}_{R,p} \tag{2.56}$$

where $M^{-1}_{L,p1}$,$M^{-1}_{R,p1}$ are the transformation matrices, $\widetilde{\mathbf{H}}$ is the decoupled Hamiltonian and H is the original Hamiltonian. The decoupled Hamiltonian has the form[124]

$$\widetilde{H} = \begin{bmatrix} \ddots & \ddots & & & & \\ \ddots & \hat{H}_{p-1,p-1} - 1E & 0 & \hat{H}_{p-1,p+1} & & \\ 0 & 0 & H_{p,p} - 1E & 0 & & \\ & \hat{H}^{\dagger}_{p-1,p+1} & 0 & \hat{H}_{p+1,p+1} - 1E & H_{p+1,p+2} & \\ & & \ddots & \ddots & \ddots & \end{bmatrix} \tag{2.57}$$

while the transformation matrices have the form

$$M^{-1}_{L,P} = \begin{bmatrix} \ddots & 0 & \ddots & \dots & \dots \\ \ddots & 1 & X^{\dagger}_{p} & 0 & \ddots \\ \ddots & 0 & 1 & 0 & \ddots \\ \vdots & 0 & Y^{\dagger}_{p} & 1 & \ddots \\ \vdots & \ddots & \ddots & 0 & \ddots \end{bmatrix}, M^{-1}_{R,p} = (M^{-1}_{L,p})^{\dagger} \tag{2.58}$$

where $X_p = (H_{p,p} - 1E)^{-1} H^{\dagger}_{p-1,p}$ and $Y_p = (H_{p,p} - 1E)^{-1} H_{p,p+1}$. Additionally the terms $\hat{H}_{a,a}$ in Eq. (2.57) are defined as

$$\hat{H}_{p-1,p+1} = -H_{p-1,p} Y_p, \quad \hat{H}_{p-1,p-1} = H_{p-1,p-1} - H_{p-1,p} X_p, \quad \hat{H}_{p+1,p+1} = H_{p+1,p+1} - H^{\dagger}_{p,p+1} Y_p \tag{2.59}$$

Each plane needs to be decoupled only once, therefore we need only index the matrices $M^{-1}_{L,p1}$, $M^{-1}_{R,p1}$ by the decoupled plane index to proceed. The wave function is determined via repeated decoupling of planes until the decoupled Hamiltonian $\widetilde{\mathbf{H}}$ is block diagonal. Only the final step in the in the renormalization will be slightly different, that is the decoupling of the first and last planes 1 and $4L$, because the end blocks are not Hermitian due to the inclusion of the open-system boundary conditions[124].

The wave function is found then by multiplying the inhomogeneous vector by the inverse of the decoupled block-diagonal Hamiltonian $\widetilde{\mathbf{H}}$ and then by the transformation matrices $M_{R,p}$, in reverse decoupling order. The multiplication proceeds as a matrix-vector multiplication, a recursion relation can be used to get the wave function coefficients for each plane.

The transformation matrices are not multiplied together, instead it is a matrix-vector multiplication and therefore much more efficient[124]. As we noted, each plane is decoupled once, therefore a recursion relation can give the subvectors of the wave function coefficients for each atomic plane. The recursion is

$$C_1 = [\widetilde{H}_{1,1} + \Sigma_1 - 1E]^{-1} V_1, \quad C_{4L} = -X_{4L} C_1 \tag{2.60}$$

for the the first plane and subsequent planes p are given by

$$C_p = -X_p C_{p-m} - Y_p C_{p+n} \tag{2.61}$$

where the recursion proceeds in reverse decoupling order and, prior to decoupling, the plane p was connected to planes $(p-1)$ and $(p+1)$, $p \neq 1, 4L$.

2.4 Conclusions

In this chapter we have presented the theoretical background which will be relevant to the study of the electronic and transport properties of the group-IV semiconductor alloys $Ge_{1-x}C_x$ and $Ge_{1-x}Sn_x$ throughout the remainder of the thesis.

We have over viewed the theoretical methods that we have used to calculate the electronic of tetrahedrally bonded semiconductors. By reviewing the theory of electronic band structure in a solid in section 2.2, we derived a method for calculating the electronic properties in the tight-binding framework. In section 2.3 we have reviewed the non-equilibrium Green's function method that will be used to calculate the transport properties of $Ge_{1-x}Sn_x$ alloys.

We have summarised the computationally efficient wave function method for calculating the transport properties in Section 2.3.3. In chapter 3 we will use the TB formalism to investigate the electronic properties of $Ge_{1-x}C_x$ alloys with a view to determining the viability of direct gap optical emission from the alloy. In chapters 4 and 5 we will use the transport frameworks described here to investigate the impact of Sn incorporation on band to band tunneling in $Ge_{1-x}Sn_x$ alloys and the implications for $Ge_{1-x}Sn_x$ TFETs.

Chapter 3

Electronic structure evolution in dilute carbide $Ge_{1-x}C_x$ alloys

3.1 Overview

In this chapter we present a theoretical analysis of the evolution of the electronic structure of the group-IV alloy $Ge_{1-x}C_x$ with increasing carbon content in the dilute regime (x < 2%). Given the conflicting suggestions of direct gap behaviour in $Ge_{1-x}C_x$ alloys, further theoretical insight is required to quantify the nature and evolution of the $Ge_{1-x}C_x$ electronic structure, so that the potential of the alloy for practical applications can be assessed. In this thesis, we calculate the electronic structure of idealised (ordered) $Ge_{N-1}C_1$ alloy supercells, and of realistic (large, disordered) $Ge_{1728-M}C_M$ ($x = \frac{M}{1728}$) alloy supercells containing a random distribution of M substitutional C atoms. While previous DFT-based analyses have been limited to ordered supercells containing $\leq$ 128 atoms ($x \geq 0.78\%$)[38], we adopt a semi-empirical theoretical framework that allows high-throughput calculations to be performed for large supercells containing $\gtrsim 10^3$ atoms. Using this approach we quantify (i) the impact of C incorporation on the Ge electronic structure in the ultra-dilute (impurity) limit, (ii) the impact of alloy disorder (including C clustering) on the electronic structure, and (iii) the evolution of the electronic structure with C composition x in large, disordered alloy supercells.

These calculations demonstrate a reduction in the fundamental band gap with increasing C content due to reduction in the CB edge energy while the VB edge remains relatively unperturbed. Our calculations demonstrate the formation of a quasi direct band gap in $Ge_{1-x}C_x$ alloys where the $Ge_{1-x}C_x$ CB edge states acquires an admixture of indirect and direct gap like character. Ordered supercell calculations show the emergence of a direct gap like state at the CB minimum located at the zone centre Gamma point. Increasing C composition in ordered supercells drives a reduction in band gap brought about by an increase in band mixing effects. Initially this would lead one to conclude that $Ge_{1-x}C_x$ possesses a direct gap, however, further calculations that investigate the character of the CB minimum state demonstrate that the CB edge state is only quasi direct with a large indirect component. The character of the CB edge state was probed via two methods, firstly via pressure calculations of the CB edge state by applying hydrostatic strain to the supercells: the

resulting pressure coefficient could then be compared to the pressure coefficients of the Ge direct and indirect valleys which have values of 4.33 eV/kbar and 13.33 ev/kbar respectively. Secondly we project the Ge Γ and L states onto the alloy CB states. As a result we find the alloy CB edge state retains primarily indirect gap character, acquiring at maximum 22% Γ direct gap character. Analysis of the evolution of the $Ge_{1-x}C_x$ fundamental band gap with composition demonstrates a decrease in the band gap with composition however in the dilute regime of interest there is minimal difference between the $Ge_{1-x}C_x$ and Ge band gaps. This suggests minimal localisation of electron states on the isolated C atoms, suggesting C does not act as an isovalent impurity in $Ge_{1-x}C_x$. Further, direct calculation of the localisation of the C derived state reveals little localisation about the C atom. While the direct gap character of the C derived state remains low, the indirect L character of the state is large, >71% at high compositions, and increases in the dilute regime.

We explicitly demonstrate the presence of C-induced mixing of Ge host matrix CB edge states in ordered alloy supercells, and demonstrate that the $Ge_{1-x}C_x$ alloy CB edge retains primarily indirect (Ge L_{6c}) character. Explicit analysis of the CB eigenstates in supercells containing up to 2000 atoms provides a broader picture of the electronic structure evolution. Specifically, we confirm that $Ge_{1-x}C_x$ admits a "quasi-direct" band gap in ordered alloy supercells: while the CB minimum appears at the zone centre of a $Ge_{N-1}C_1$ supercell, the associated eigenstate in selected supercells is formed predominantly of a linear combination of Ge L_{6c} CB edge states having purely *s*-like orbital character at the C lattice site. We further demonstrate that the alloy CB edge exhibits minimal localisation with increasing supercell size, challenging the suggestion that the introduction of an isolated substitutional C atom in Ge generates a (strongly) localised impurity state. For disordered alloy supercells we find that short-range alloy disorder gives rise to a distribution of C-related localised states – associated with nearest-neighbour C-C pairs, as well as larger clusters of substitutional C atoms and various C-Ge-C type neighbour complexes – lying energetically within the Ge band gap, with these states acquiring minimal direct (Ge Γ_{7c}) character. Overall, our analysis reveals behaviour that is markedly different to that expected on the basis of the BAC model and, in agreement with the conclusions of Kirwan et al.[41], we demonstrate that C incorporation does not drive the formation of a direct band gap.

The rest of this chapter is organised as follows. In section 3.2 we describe the methods used to calculate the electronic band structure of $Ge_{1-x}C_x$ alloys. We also overview the parameterisation of the tight binding model based on initial DFT calculations, where we compare the accuracy of our tight binding model with the DFT calculations. The results of $Ge_{1-x}C_x$ calculations will then be separated into two sections, one focusing on ordered alloy calculations in section 3.3 and the other on disordered alloy calculations in section 3.4. The separate investigation of ordered and disordered alloys is required due to the large impact alloy disorder can have on HMAs. In section 3.3 we first minimize alloy disorder by creating ordered supercells where a single C atom is placed in a supercell. As a result ordered alloys represent an ideal case which serves to maximize the benefits of C incorporation. In section 3.4 we investigate disordered supercells via random incorporation of C in a large supercell which is a more realistic representation of the material due

to the disorder that would be present in real alloys. In section 3.5 we discuss the implications of this research for device applications and in section 3.6 we summarise and conclude.

3.2 Theoretical models

Highly-mismatched semiconductor alloys are characterised by constituent elements differing significantly in size (covalent radius) and chemical properties (valence orbital energies), resulting in (i) significant changes to the electronic structure of the host matrix semiconductor in response to incorporation of dilute concentrations of the alloying element, and (ii) strong sensitivity of the electronic structure to short-range alloy disorder[54–56]. From a technical perspective, these factors constitute a breakdown of the virtual crystal approximation (VCA), mandating direct atomistic calculations in order to capture – even qualitatively – the evolution of the alloy electronic structure.

Beginning with an N-atom Ge_N supercell, the smallest C composition that can be treated is $x = \frac{1}{N}$ in an ordered $Ge_{N-1}C_1$ supercell. Investigation of the material properties in the dilute composition (impurity) limit is therefore limited by the maximum supercell size that can be treated by the electronic structure method employed, and the use of ordered supercells to achieve dilute compositions precludes the investigation of alloy disorder effects. First principles methods that accurately describe the electronic properties of semiconductors are in practice limited to $N \lesssim 10^2$ atoms, allowing access to compositions $\sim 1\%$ but providing limited scope to investigate properly electronically isolated impurities or to quantify alloy disorder effects.

Our theoretical analysis of dilute $Ge_{1-x}C_x$ alloys is therefore based on a semi-empirical framework, which can be extended to large system sizes to enable quantitative atomistic analysis of the impact of alloy disorder and related effects in realistic ($N \gtrsim 10^3$, disordered) alloy supercells. Firstly, we use a parameterised valence force field (VFF) potential to perform structural relaxation of alloy supercells[126]. Secondly, the electronic structure of relaxed alloy supercells is computed using a nearest-neighbour sp^3s^* tight-binding (TB) Hamiltonian as described in section 2.2[40]. Both the VFF potential and TB Hamiltonian are parameterised via the bulk structural, elastic and electronic properties of the constituent materials – i.e. the elemental and compound materials formed by nearest-neighbour bonds in a given alloy supercell – which for $Ge_{1-x}C_x$ are the elemental diamond-structured group-IV semiconductors Ge and C, and the fictitious zinc blende IV-IV compound GeC (zb-GeC)[104, 127].

3.2.1 Valence force field potential

We use the modified form [103] of the VFF potential introduced by Musgrave and Pople[102], whereby the contribution to the lattice free energy associated with an atom located at lattice site i is

Parameter	Unit	Ge	C	zb-GeC
$r^{(0)}$	Å	2.445	1.530	1.969
k_r	eV Å^{-2}	7.0414	26.4077	11.8086
k_θ	eV Å^{-2} rad^{-2}	0.5104	3.7208	1.0780
k_{rr}	eV Å^{-2}	0.2416	0.9740	1.0557
$k_{r\theta}$	eV Å^{-2} rad^{-1}	0.3005	1.7832	1.2515

TABLE 3.1: Equilibrium bond lengths $r^{(0)}$, and force constants k_r, k_θ, k_{rr} and $k_{r\theta}$, used to implement structural relaxations for $Ge_{1-x}C_x$ alloy supercells using the VFF potential of Eq. (3.1). Force constants have been computed analytically based on DFT-calculated structural properties for Ge, C and zb-GeC. [104, 126]

$$
\begin{aligned}
V_i = & \frac{1}{2}\sum_j \frac{k_r}{2}\left(r_{ij}-r_{ij}^{(0)}\right)^2 \\
& + \sum_j \sum_{k>j} \left[\frac{k_\theta}{2} r_{ij}^{(0)} r_{ik}^{(0)} \left(\theta_{ijk}-\theta_{ijk}^{(0)}\right)^2 \right. \\
& \qquad + k_{rr}\left(r_{ij}-r_{ij}^{(0)}\right)\left(r_{ik}-r_{ik}^{(0)}\right) \\
& \left. + k_{r\theta}\left(r_{ij}^{(0)}\left(r_{ij}-r_{ij}^{(0)}\right) + r_{ik}^{(0)}\left(r_{ik}-r_{ik}^{(0)}\right)\right)\left(\theta_{ijk}-\theta_{ijk}^{(0)}\right) \right],
\end{aligned}
\tag{3.1}
$$

where the indices j and k describe the nearest-neighbour atoms of atom i, $r_{ij}^{(0)}$ and r_{ij} respectively denote the unstrained (equilibrium) and relaxed bond lengths between atoms i and j, and $\theta_{ijk}^{(0)}$ and θ_{ijk} respectively denote the unstrained and relaxed angles formed by adjacent nearest neighbour bonds, between atoms i and j, and between atoms i and k. The first and second terms in Eq. (3.1) respectively describe contributions to the lattice free energy associated with pure bond stretching and pure bond-angle bending, while the third and fourth terms are "cross terms" which respectively describe the impact of changes in r_{ik} on r_{ij}, and the impact of changes in θ_{ijk} on both r_{ij} and r_{ik}.

Re-casting Eq. (3.1) in terms of macroscopic and internal strains allows the force constants k_r, k_θ, k_{rr} and $k_{r\theta}$ to be determined analytically in terms of the elastic constants C_{11}, C_{12} and C_{44}, and the Kleinman (internal strain) parameter ζ for diamond or weakly-polar zinc blende structured materials[126]. This provides an exact description of the static lattice properties in the linear elastic limit, circumventing the conventional requirement to determine the VFF force constants via numerical fitting. The unstrained bond lengths and VFF force constants used in our calculations are provided in Table 3.1. Structural relaxations – implemented using the General Utility Lattice Program (GULP) [105–107] – for $Ge_{1-x}C_x$ alloy supercells proceed by minimising the lattice free energy computed via Eq. (3.1), by allowing the supercell lattice vectors and ionic positions to relax freely.

3.2.2 Tight-binding Hamiltonian

Given its use of a localised basis of atomic orbitals, the TB method is well suited to analyse the impact of localised impurities on the electronic structure of a given host matrix semiconductor[128].

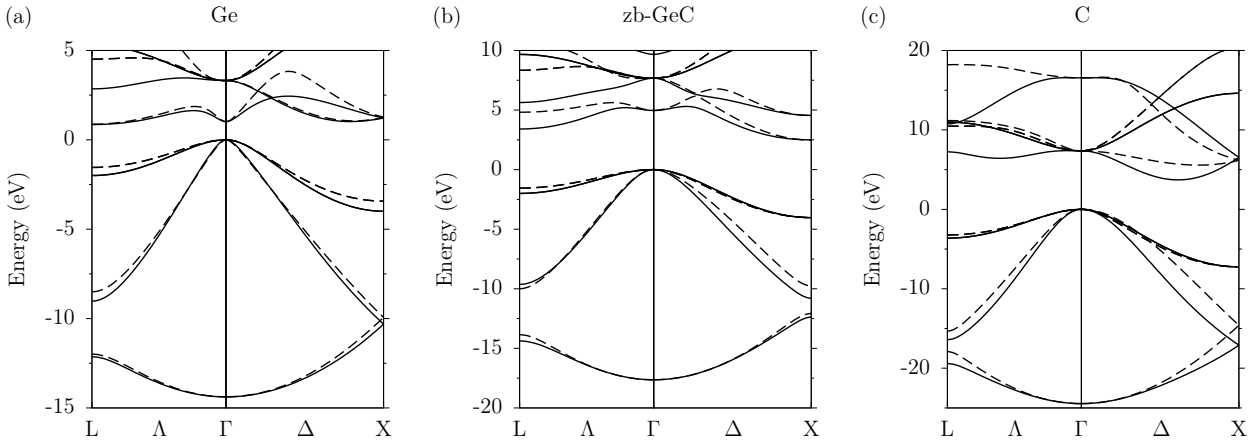

FIGURE 3.1: Band structure of (a) Ge, (b) zb-GeC, and (c) C calculated via DFT using the HSEsol exchange-correlation functional (dashed lines), and via a semi-empirical sp^3s^* TB Hamiltonian (solid lines). All calculations omit spin-orbit coupling. For comparative purposes, the zero of energy has been chosen to lie at the VB edge in all cases. Note the differences in scales on the ordinates of (a), (b) and (c).

This is of particular importance for highly-mismatched alloys – such as $Ge_{1-x}C_x$ – in which the constituent elements have significant differences in size and chemical properties. We employ a nearest-neighbour sp^3s^* TB Hamiltonian[92], based closely on that we have recently established for $Ge_{1-x}Sn_x$ alloys[68]. We note however that the TB model employed here differs from that of O'Halloran et al. [68]. in that we omit spin-orbit coupling. This is justified on the basis that DFT calculations have demonstrated that C incorporation in Ge primarily impacts the band structure close in energy to the Ge CB edge[38, 41], where spin-orbit coupling has minimal impact. Henceforth, we therefore refer to high-symmetry eigenstates of Ge using the conventional O_h ($m\bar{3}m$) point group notation for the diamond lattice[129].

It is well established that the accuracy of the TB fit to the band structure of a given semiconductor material can be improved via the inclusion of d-like atomic orbitals, to obtain a $sp^3s^*d^5$ basis set[130]. We have chosen to employ an sp^3s^* rather than $sp^3s^*d^5$ basis in our calculations for two reasons. Firstly, while the $sp^3s^*d^5$ basis allows for more accurate fitting of a given target band dispersion, this comes at the cost of doubling the size of the Hamiltonian for a supercell containing a given number of atoms compared to that associated with a sp^3s^* basis. For the large supercell sizes required to simulate the properties of realistic highly-mismatched alloys, this doubling of the size of the supercell Hamiltonian represents a significant increase in the computational cost of numerical diagonalisation. Secondly, while the $sp^3s^*d^5$ basis enables a range of band-edge effective masses to be accurately fitted to, the sp^3s^* basis is sufficient to accurately describe the band energies at high-symmetry points in the Brillouin zone. Since our aim here is to describe the nature of the alloy band gap, we are interested primarily in band hybridisation effects. The strength with which different eigenstates of a given semiconductor hybridise in response to a perturbation generally depends critically on the separation in energy of a small number of high-symmetry states. For dilute $Ge_{1-x}C_x$ alloys we are interested in identifying the potential presence of an indirect- to direct-gap transition, so it is crucial that the energy of the L_{1c} (CB minimum) states are described accurately relative to the $\Gamma_{2'c}$ (zone-centre CB edge) state. For the purpose of

describing the nature and evolution of the band gap of a large number of semiconductor alloys the sp^3s^* basis is therefore sufficient, representing a small trade-off in accuracy in order to significantly reduce parametric complexity and computational cost. Indeed, we have previously demonstrated that a TB Hamiltonian employing an sp^3s^* basis provides quantitatively accurate insight into the properties of highly-mismatched III-V semiconductor alloys containing nitrogen [131–133] (N), boron [134–136] (B) or bismuth [137–140] (Bi).

The impact of lattice relaxation (local strain) is incorporated in the TB Hamiltonian via bond length- and angle-dependent inter-atomic interaction matrix elements using, respectively, the generalised form of Harrison's rule [141, 142] and the Slater-Koster two-centre integrals[97]. To overcome the failure of this conventional parameterisation to describe deformation potentials associated with tetragonal (biaxial) deformations, we include two additional strain-related terms. Firstly, we include an on-site correction of the p orbital energies, which provides an accurate description of the Γ-point VB edge axial deformation potential b[143]. Secondly, we include a correction to the $V_{s^*p\sigma}$ inter-atomic interaction matrix elements, which accounts for the influence of d orbital interactions in determining the axial deformation potential Ξ_u^{X} associated with the X-point CB edge states[144]. To incorporate these corrections in alloy supercell calculations we have cast them in local form, by writing the infinitesimal strain tensor at each lattice site in terms of the relaxed nearest-neighbour bond lengths and angles about that site. For a given relaxed alloy supercell, the construction of the supercell Hamiltonian – which accounts explicitly for size and chemical differences between constituent elements – proceeds as described in O'Halloran et al. [68].

Our TB parameters are obtained by fitting to selected high-symmetry point energies determined via hybrid functional (HSEsol) DFT calculations[127]. Since C incorporation in Ge primarily impacts the band structure close in energy to the CB edge of the Ge host matrix semiconductor, our priority in fitting TB parameters for Ge was to describe the energies of the $\Gamma_{2'c}$, L_{1c} and X_{1c} high-symmetry Γ-, L- and X-point CB edge states[68]. In the VB C incorporation will lead to a C-related state deep within the VB and will have little impact at the top of the VB[145]. For C and zb-GeC we follow the fitting procedure outlined by Vogl et al. [92] without modification. The zero of energy for our alloy TB Hamiltonian is set at the Ge $\Gamma_{25'v}$ VB edge. We assume a natural VB offset of -4.24 eV between C and Ge, following the first principles calculations of Li et al. [146]. Based on a linear interpolation of this VB offset with respect to the HSEsol-calculated lattice constants of C and Ge[104], we estimate a VB offset of -2.12 eV between Ge and zb-GeC.

The resulting TB fits to the Ge, zb-GeC and C band structures are shown respectively in Figs. 3.1(a), 3.1(b) and 3.1(c), where solid (dashed) black lines show the TB-calculated (reference HSEsol DFT [127]) band structure. Note the differences in scales on the ordinates of Figs. 3.1(a), 3.1(b) and 3.1(c). For zb-GeC and C the underestimation of the L-point CB edge energies represents a typical sp^3s^* fit[92]. We note however that these discrepancies, which are largest in our TB fit to the band structure of C, should have minimal impact in alloy supercell calculations. Since we employ a nearest-neighbour TB Hamiltonian, parameters for C are only employed in the construction of the supercell Hamiltonian when C atoms appears as nearest neighbours. In a randomly disordered substitutional $\mathrm{Ge}_{1-x}\mathrm{C}_x$ alloy having C composition x, the probability for small x of

two C atoms occupying nearest-neighbour lattice sites is $2x^2$ – i.e. a randomly disordered N-atom $Ge_{1-x}C_x$ supercell will contain, on average, a total of $N \times 2x^2$ C-C nearest-neighbour pairs. Since we are concerned only with dilute C compositions $x \lesssim 2\%$, for the supercells considered in our analysis – which contain $N \leq 2000$ atoms – we expect < 2 C-C pairs to be present in any given disordered alloy supercell. This indeed turns out to be the case for the randomly disordered supercells considered in section 3.4.3. In addition, as we describe in section 3.3.2, the results of our TB supercell calculations for small, ordered $Ge_{1-x}C_x$ supercells are in good quantitative agreement with hybrid functional DFT calculations[41, 147], confirming the appropriateness of our TB model to investigate $Ge_{1-x}C_x$ alloys.

3.2.3 Hydrostatic pressure coefficients calculations

States originating from different wave vectors $\mathbf{k}$ in the Brillouin zone of the primitive unit cell of the underlying diamond lattice are folded back to the zone centre ($\mathbf{K} = 0$) in supercell calculations. It can therefore be difficult to identify the character of individual zone-centre states in the band structure of a $Ge_{1-x}C_x$ supercell, and hence to deduce the composition at which the alloy becomes a direct-gap semiconductor. To address this issue, we investigate how the alloy CB structure changes as hydrostatic pressure is applied to the alloy supercell. The pressure coefficients $\frac{dE_g}{dP}$ for the indirect L_{6c}-Γ_{8v} and direct Γ_{7c}-Γ_{8v} band gaps of Ge are significantly different to one another, having respective values 4.66 and 13.33 meVkbar^{-1} in our HSEsol calculations, and 4.07 and 13.23 meVkbar^{-1} in our mBJ calculations. Calculation of $\frac{dE_g}{dP}$ for the fundamental band gap in a given alloy supercell then allows us to identify the character of the band gap, and hence to track the evolution of the character of the CB edge states and band gap with increasing Sn composition x.

3.3 Band structure of ordered $Ge_{1-x}C_x$ alloy supercells

In this section we present the results of our analysis of the electronic structure of dilute $Ge_{1-x}C_x$. We first provide motivation for our choice of supercell sizes in section 3.3.1. We begin our analysis of the band structure in section 3.3.2 by considering the impact of C incorporation on the band structure of ordered alloy supercells, and then in sections 3.3.3 and 3.3.4 we respectively analyse in detail the character and localisation of the alloy CB edge states as a function of C composition x.

3.3.1 Selection of ordered alloy supercells

Emerging theoretical evidence suggested the possibility of strong C-induced hybridisation of the Ge Γ_{7c} and L_{6c} CB edge states in $Ge_{1-x}C_x$. In a real alloy, all states that can (by symmetry) mix will mix: this physical effect will manifest in electronic calculations regardless of the choice of supercell. In the case of $Ge_{1-x}C_x$, we note that (i) the alloy CB edge originates from the Ge L_{6c} states, and (ii) we are interested in the acquisition of direct Ge Γ_{7c} character by the alloy

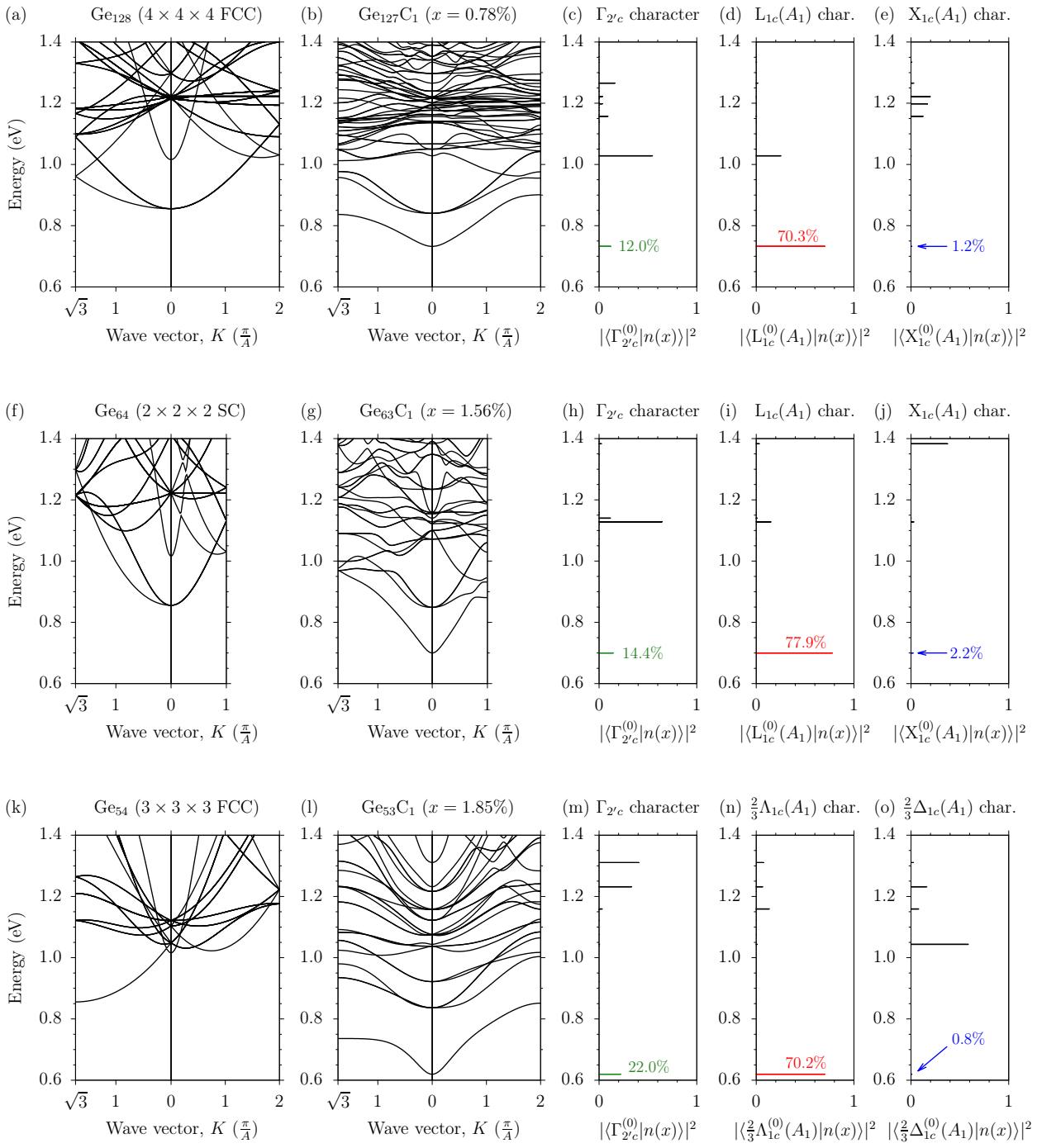

FIGURE 3.2: Top row: Calculated CB structure for (a) a Ge_{128} supercell, and (b) an ordered $Ge_{127}C_1$ ($x = 0.78\%$) supercell. (c) – (e) respectively show the calculated fractional Ge $\Gamma_{2'c}$, $L_{1c}(A_1)$ and $X_{1c}(A_1)$ character spectra of the $Ge_{127}C_1$ supercell of (b). Middle row: Calculated CB structure for (f) a Ge_{64} supercell, and (g) an ordered $Ge_{63}C_1$ ($x = 1.56\%$) supercell. (h) – (j) respectively show the calculated fractional Ge $\Gamma_{2'c}$, $L_{1c}(A_1)$ and $X_{1c}(A_1)$ character spectra for the $Ge_{63}C_1$ supercell of (g). Bottom row: Calculated CB structure for (k) a C-free Ge_{54} supercell, and (l) an ordered $Ge_{53}C_1$ ($x = 1.85\%$) alloy supercell. (m) – (o) respectively show the calculated fractional Ge $\Gamma_{2'c}$, $\frac{2}{3}\Lambda_{1c}(A_1)$ and $\frac{2}{3}\Delta_{1c}(A_1)$ character spectrum for the $Ge_{53}C_1$ supercell of (l). The zero of energy of all band structure plots is set at the Ge VB edge. Green, red and blue colouring is used to highlight the Ge $\Gamma_{2'c}$, $L_{1c}(A_1)$ (or $\frac{2}{3}\Lambda_{1c}(A_1)$), and $X_{1c}(A_1)$ (or $\frac{2}{3}\Delta_{1c}(A_1)$) character of the alloy supercell CB edge state. CB structure figures are given along two directions, along (111) towards L on the left hand side and along (001) towards X on the right hand side of each figure.

CB edge. These observations suggest that there does not exist sufficient physical justification to explicitly neglect Γ_{7c}-L_{6c} mixing – which can be expected to be pronounced based on the small separation in energy of these states – in the analysis of the $Ge_{1-x}C_x$ electronic structure. We restrict our attention primarily to supercells in which the L-point states of the underlying diamond structure fold to the supercell zone centre $\mathbf{K} = 0$ – i.e. $n \times n \times n$ face-centred cubic (FCC) or simple cubic (SC) supercells for even values of n. This allows for C-induced hybridisation of the L_{1c} CB minimum and $\Gamma_{2'c}$ zone-centre CB edge states of Ge, which can be expected to be important given the small ≈ 0.15 eV separation in energy between the fundamental (indirect) and direct band gaps of Ge. Our calculations suggest, in agreement with hybrid functional DFT calculations[38, 41], that C incorporation has minimal impact on the valence band (VB) structure, so we focus our analysis on the alloy CB structure.

We note that in supercells where L and X do not fold back to the origin, such as in the 54 atom case, L and Γ do not mix with each other. Points close to L and X will however fold back to the origin, with states two-thirds of the way from Γ to L and from Γ to X folding back in the 54 atom case. Supercell calculations carried out by a colleague (Amy Kirwan) show that the pressure coefficients of these states are very close to those of the states at the L and X point. These states will still provide the lowest energy conduction states at Γ in the 54-atom supercell and are therefore available to mix with the state, to which they are close in energy. Consequently, a very similar pressure coefficient analysis could be undertaken in such supercells to analyse the character of the lowest conduction band states in the alloy. However, the Γ state is the lowest conduction state at the zone centre in the 54-atom Ge supercell, with the states which are two thirds of the way to L and to X lying higher in energy. This inversion of the order of the direct and indirect gap states may then have a quantitative impact on the results and analysis of mixing in small supercells where L and X do not fold back to the origin.

We select three supercells for the alloy band structure calculations. The first is an 128-atom $Ge_{127}C_1$ 444 FCC supercell with a composition of $x = 0.78125\%$ which was chosen as the lowest composition to be investigated that can be compared to similar investigation of the alloy CB edge state using DFT calculations. The next supercell is a 64-atom $Ge_{63}C_1$ 222 SC supercell with a composition of $x = 1.5625\%$. Both of these supercells will have folded band structures such that the L_{6c} states of Ge CB edge will fold to the zone centre and maximize mixing with the Ge Γ_{7c} state. The final supercell is a 54-atom $Ge_{53}C_1$ 333 FCC supercell with a composition of $x = 1.8519\%$ where the L_{6c} states of Ge CB edge will not fold to the zone centre and will therefore not mix with the Ge Γ_{7c} state.

3.3.2 Band structure of ordered $Ge_{1-x}C_x$ alloy supercells

Figure 3.2(b) shows the calculated CB structure of an ordered, 128-atom $Ge_{127}C_1$ ($x = 0.78\%$) supercell. For comparative purposes, the CB structure of the corresponding C-free Ge_{128} supercell is shown in Fig. 3.2(a). The band dispersion is plotted as a function of $\frac{\pi}{A}$, where A is the supercell lattice constant, equal respectively to $\frac{na}{2}$ or na for an $n \times n \times n$ FCC or SC supercell. The

lowest energy CB states at $\mathbf{K} = 0$ in Ge_{128} are the folded L_{1c} CB edge states, with the $\Gamma_{2'c}$ zone-centre state lying 160 meV higher in energy. For the $Ge_{127}C_1$ supercell we firstly note that C incorporation strongly perturbs the CB structure, leading to a large band gap reduction of 91 meV compared to the fundamental band gap of Ge ($E_g = 0.856$ eV, in the absence of spin-orbit coupling). Additionally, we note that the alloy CB minimum lies at $\mathbf{K} = 0$. Indeed, based on qualitative inspection of Fig. 3.2(b) it is tempting to conclude – given the strong band gap reduction and apparent emergence of a C-related impurity band lying energetically within the Ge band gap – that C acts as an isovalent impurity, driving strong band gap reduction via a BAC interaction, as suggested by Stephenson et al. [38, 39]. However, we note that the CB edge state is non-degenerate, while the second lowest energy set of CB states – lying 108 meV above the CB edge in energy – is threefold degenerate. This suggests C-induced splitting of the fourfold degenerate L_{1c} CB edge states of Ge, and that the alloy CB edge might be better described in terms of a linear combination of Ge L_{1c} states, rather than as a hybridised C-related localised impurity state.

To ascertain whether or not this is the case, we have undertaken a quantitative analysis of the character of the alloy CB states. Figure 3.2(c) shows the fractional Ge $\Gamma_{2'c}$ character of the $Ge_{127}C_1$ CB states, calculated by projecting the $\Gamma_{2'c}$ eigenstate $|\Gamma^{(0)}_{2'c}\rangle$ of the Ge_{128} host matrix supercell onto the full spectrum $\{|n(x)\rangle\}$ of $\mathbf{K} = 0$ $Ge_{127}C_1$ alloy CB eigenstates. Note that we use the superscript "(0)" henceforth to denote unperturbed Ge host matrix eigenstates. We calculate that the $Ge_{127}C_1$ CB edge eigenstate – highlighted in Fig. 3.2(c) via green colouring – acquires a small (12.0%) admixture of Ge $\Gamma_{2'c}$ character. As a consequence of their symmetry the second lowest energy set of CB states acquire no Ge $\Gamma_{2'c}$ character, while the third lowest energy state – originating from the Ge $\Gamma_{2'c}$ state and lying 296 meV above the CB edge in energy – retains majority (54.4%) Ge $\Gamma_{2'c}$ character. We find that the remainder of the Ge $\Gamma_{2'c}$ character is spread over a small number of higher energy alloy CB states, originating primarily from the X_{1c} CB edge states of Ge. Our calculations therefore suggest that the $Ge_{127}C_1$ CB edge acquires only a small amount of direct (Ge $\Gamma_{2'c}$) character. To confirm this we calculate the pressure coefficient $\frac{dE_g}{dP}$ associated with the fundamental band gap. We have shown elsewhere [37, 68, 69] that calculation of the band structure as a function of hydrostatic pressure can provide very useful insight into the character of the band edge states, and hence the nature and evolution of the alloy band gap. The pressure coefficients associated with the indirect L_{1c}-$\Gamma_{25'v}$, direct $\Gamma_{2'c}$-$\Gamma_{25'v}$ and indirect X_{1c}-$\Gamma_{25'v}$ band gaps of Ge are significantly different to one another, having respective values $\frac{dE_g}{dP} = 4.66$, 13.33 and -1.60 meV kbar^{-1} in the HSEsol DFT calculations to which we fit our TB parameters. Since we are dealing with dilute C compositions, we expect that an alloy having primarily indirect character will have a significantly lower pressure coefficient than an alloy having direct-gap character. We calculate $\frac{dE_g}{dP} = 5.25$ meV kbar^{-1} for the $Ge_{127}C_1$ supercell confirming that, despite strong perturbation of the CB structure, the alloy CB edge retains primarily Ge L_{1c} character. Our calculated value of $\frac{dE_g}{dP}$ here is in good agreement with the value of 4.55 meV kbar^{-1} obtained from the hybrid functional DFT calculations of Kirwan et al. [41], with the similarly low values of the TB- and DFT-calculated supercell band gap pressure coefficient confirming the indirect nature of the alloy band gap.

Direct inspection of the $Ge_{127}C_1$ CB edge eigenstate reveals purely s-like orbital character (A_1 symmetry) at the C lattice site. Since, in general, alloying drives hybridisation between host matrix states having the same symmetry, we conclude that C incorporation drives hybridisation primarily between $|\Gamma_{2'c}^{(0)}\rangle$ and a linear combination $|L_{1c}^{(0)}(A_1)\rangle$ of Ge L_{1c} eigenstates having purely s-like orbital character at the C lattice site. We confirm that this is the case by using the $\mathbf{K} = 0$ eigenstates of Ge_{128} to explicitly construct $|L_{1c}^{(0)}(A_1)\rangle$, and then calculate the corresponding Ge $L_{1c}(A_1)$ character of the $Ge_{127}C_1$ CB states – shown in Fig. 3.2(d) – analogously to the calculation of the $\Gamma_{2'c}$ character. Doing so, we indeed find that the $Ge_{127}C_1$ CB edge eigenstate – highlighted in Fig. 3.2(d) via red colouring – is constituted primarily of $|L_{1c}^{(0)}(A_1)\rangle$, having 70.3% Ge $L_{1c}(A_1)$ character. Finally, since the calculated Ge $\Gamma_{2'c}$ and $L_{1c}(A_1)$ character of Figs. 3.2(c) and 3.2(d) demonstrates the presence of hybridisation between $\Gamma_{2'c}$, $L_{1c}(A_1)$ and higher energy CB states, we investigate the possibility of C-induced mixing with higher energy Ge host matrix CB states. In Ge_{128} the next highest energy CB states above $\Gamma_{2'c}$ are the folded X_{1c} CB edge states. As such, we construct $|X_{1c}^{(0)}(A_1)\rangle$ – i.e. a linear combination of Ge X_{1c} states having purely s-like orbital character at the C lattice site – and calculate the Ge $X_{1c}(A_1)$ character of the $Ge_{127}C_1$ CB states. The results of this analysis are shown in Fig. 3.2(e), where we note that the $Ge_{127}C_1$ CB edge eigenstate – highlighted in Fig. 3.2(e) via blue colouring and an arrow – acquires only 0.8% Ge $X_{1c}(A_1)$ character. We therefore conclude for the $Ge_{127}C_1$ supercell considered here (i) that C incorporation drives hybridisation between A_1-symmetric (linear combinations of) Ge host matrix states lying close in energy to the CB edge, (ii) that the $Ge_{127}C_1$ CB edge is derived primarily from a linear combination $|L_{1c}^{(0)}(A_1)\rangle$ of Ge L_{1c} CB minimum states, and (iii) that the alloy band gap retains primarily indirect character.

To investigate these trends as a function of x we have repeated this analysis for an ordered, 64-atom $Ge_{63}C_1$ ($x = 1.56\%$) supercell, the calculated CB structure of which is shown in Fig. 3.2(g). The CB structure of the corresponding C-free Ge_{64} supercell is shown in Fig. 3.2(f). Again, we note that the lowest energy CB states at $\mathbf{K} = 0$ in Ge_{64} are the folded L_{1c} CB minimum states. Since this supercell has SC lattice vectors, the Brillouin zone boundary along (001) lies at $K_z = \frac{\pi}{A}$. Again, we note that C incorporation leads to a strong reduction of the band gap, by 93 meV compared to the fundamental band gap of Ge. Despite that the C composition in $Ge_{63}C_1$ is twice that in $Ge_{127}C_1$, we note that the calculated band gap reduction in both cases is approximately equal. This suggests strong composition-dependent bowing of the alloy band gap, the details of which depend precisely on the band mixing present in a given alloy supercell. We note that the ordering, degeneracy and orbital character of the $Ge_{63}C_1$ $\mathbf{K} = 0$ eigenstates are as described above for $Ge_{127}C_1$. Figures 3.2(h), 3.2(i) and 3.2(j) show, respectively, the Ge $\Gamma_{2'c}$, $L_{1c}(A_1)$ and $X_{1c}(A_1)$ character of the $Ge_{63}C_1$ $\mathbf{K} = 0$ CB states. Qualitatively, we note similar trends as for the $Ge_{127}C_1$ supercell. Firstly, C incorporation drives hybridisation between the $\Gamma_{2'c}$, L_{1c} and X_{1c} states of the Ge host matrix. Secondly, the alloy CB edge eigenstate retains primarily (77.9%) indirect (Ge $L_{1c}(A_1)$) character, and acquires only a small admixture (14.4%) direct (Ge $\Gamma_{2'c}$) character. As in Figs. 3.2(c) – 3.2(e), the $\Gamma_{2'c}$, $L_{1c}(A_1)$ and $X_{1c}(A_1)$ character of the $Ge_{63}C_1$ CB edge eigenstate in Figs. 3.2(h) – 3.2(j) is highlighted using green, red and blue colouring. Thirdly, C-induced

hybridisation of this state with X_{1c} states is negligible, with the alloy CB edge state acquiring only minimal (2.2%) Ge $X_{1c}(A_1)$ character.

We have so far considered the impact of C incorporation on the CB edge states only in the case where the L-point eigenstates of the corresponding C-free Ge supercell fold to $\mathbf{K} = 0$. It is however pertinent to enquire as to whether the trends identified above – and hence our conclusion that the $Ge_{1-x}C_x$ band gap retains primarily indirect character – is a consequence of the choice of supercells employed in our analysis. Indeed, the mechanism driving the electronic structure evolution in response to C incorporation should be present in all alloy supercells, regardless of the specific choice of supercell. To address this issue we present also the results of equivalent analysis of an ordered, 54-atom $Ge_{53}C_1$ ($x = 1.85\%$) supercell, the calculated CB structure of which is shown in Fig. 3.2(l). The CB structure of the corresponding C-free Ge_{54} supercell is shown in Fig. 3.2(k). For this $3 \times 3 \times 3$ FCC supercell the L points of the Brillouin zone of the underlying diamond lattice map directly to the L points of the supercell Brillouin zone. As such, the calculated CB minimum in Ge_{54} lies at $\mathbf{K} = (\frac{\pi}{A}, \frac{\pi}{A}, \frac{\pi}{A})$. Comparing Figs. 3.2(k) and 3.2(l) we note that, qualitatively, the impact of C incorporation on the CB edge again appears to illustrate the emergence of a direct band gap: the CB minimum relocates from $\mathbf{K} = (\frac{\pi}{A}, \frac{\pi}{A}, \frac{\pi}{A})$ to $\mathbf{K} = 0$ in response to C incorporation. Figure 3.2(m) shows the calculated Ge $\Gamma_{2'c}$ character of the $Ge_{53}C_1$ $\mathbf{K} = 0$ CB states. We note that the alloy CB edge again acquires only minority (22.0%) Ge $\Gamma_{2'c}$ character. Despite the explicit choice of a Ge host matrix supercell in which the CB minimum is not folded to $\mathbf{K} = 0$ (cf. Fig. 3.2(k)), giving way to a C-containing alloy supercell CB structure having its minimum at $\mathbf{K} = 0$ (cf. Fig. 3.2(l)), careful analysis of the corresponding supercell CB edge eigenstate reveals primarily indirect character, thereby demonstrating that an alloy band gap having direct character does *not* emerge due to C incorporation.

In this 54-atom supercell hybridisation between the Ge $\Gamma_{2'c}$ and L_{1c} states is blocked, since the latter do not fold back to $\mathbf{K} = 0$. In Ge_{54} the lowest energy CB states that fold to $\mathbf{K} = 0$ originate from wave vectors $\mathbf{k} = (\frac{2\pi}{3a}, \frac{2\pi}{3a}, \frac{2\pi}{3a})$, and equivalent points, located two-thirds of the way along the Λ direction between the Γ and L points in the Brillouin zone of the underlying diamond lattice. These states, which we denote by $|\frac{2}{3}\Lambda_{1c}^{(0)}\rangle$, lie 33 meV above the $\Gamma_{2'c}$ zone-centre CB edge state in Fig. 3.2(k). The next lowest energy set of Ge states which fold to $\mathbf{K} = 0$ originate from wave vectors $\mathbf{k} = (0, 0, \frac{4\pi}{3a})$, and equivalent points, which lie two-thirds of the way along the Δ direction. The corresponding states in the lowest energy CB, which we denote by $|\frac{2}{3}\Delta_{1c}^{(0)}\rangle$, lie 88 meV above the $\Gamma_{2'c}$ zone-centre CB edge states. Figures 3.2(n) and 3.2(o) respectively show the corresponding calculated Ge $\frac{2}{3}\Lambda_{1c}(A_1)$ and $\frac{2}{3}\Delta_{1c}(A_1)$ character of the $Ge_{53}C_1$ $\mathbf{K} = 0$ CB eigenstates. The Ge $\Gamma_{2'c}$, $\frac{2}{3}\Lambda_{1c}(A_1)$ and $\frac{2}{3}\Delta_{1c}(A_1)$ character of the CB edge eigenstate is highlighted in Figs. 3.2(m) – 3.2(o) using green, red and blue colouring, respectively. We calculate that the CB edge eigenstate has majority (70.2%) Ge $\frac{2}{3}\Lambda_{1c}(A_1)$ character, and acquires only minimal (0.8%) Ge $\frac{2}{3}\Delta_{1c}(A_1)$ character. We note the quantitative similarity to the $Ge_{127}C_1$ and $Ge_{63}C_1$ cases: despite that the L- and X-points do not fold to $\mathbf{K} = 0$ in Ge_{54}, the $Ge_{53}C_1$ is nonetheless formed primarily of a linear combination of states originating from a point along the Λ direction and having purely *s*-like orbital character at the C lattice site. Overall, we therefore conclude that the $Ge_{1-x}C_x$ CB edge

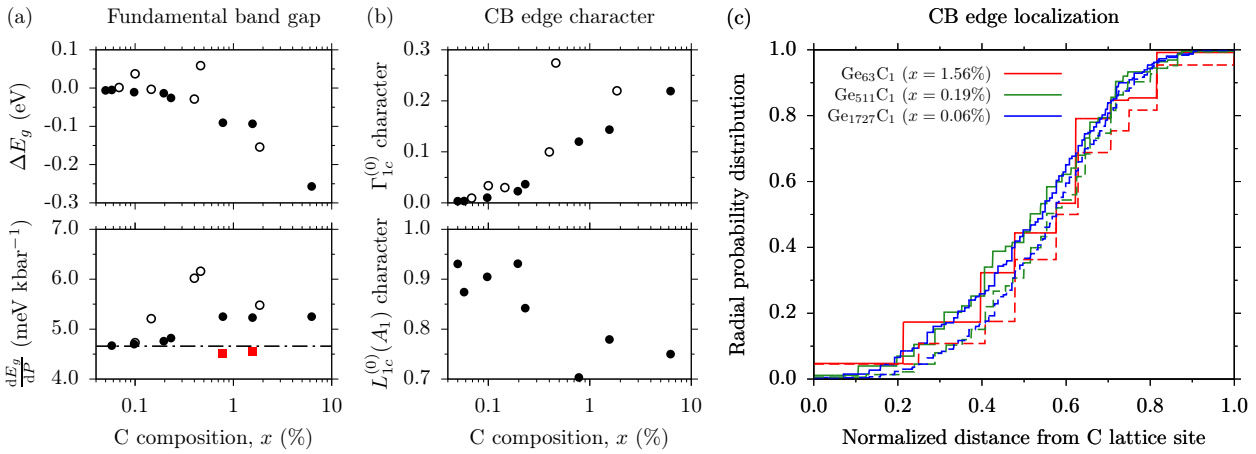

FIGURE 3.3: (a) Change in $\mathbf{K} = 0$ band gap ΔE_g (upper panel) and band gap pressure coefficient $\frac{dE_g}{dP}$ (lower panel) as a function of C composition x for a series of ordered $Ge_{N-1}C_1$ ($x = \frac{1}{N}$) alloy supercells having $16 \leq N \leq 2000$. The dashed grey line in the lower panel denotes the pressure coefficient $\frac{dE_g}{dP} = 4.66$ meV kbar^{-1} of the fundamental (indirect) band gap of Ge. The closed red squares in the lower panel show the hybrid functional DFT-calculated values of $\frac{dE_g}{dP}$ from Ref. [41]. (b) Fractional Ge $\Gamma_{2'c}$ (upper panel) and $L_{1c}(A_1)$ (lower panel) character of the alloy CB edge eigenstate for the same ordered $Ge_{N-1}C_1$ supercells as in (a). Closed (open) circles in (a) and (b) correspond to $n \times n \times n$ FCC or SC supercells having even (odd) values of n. (c) Radial probability distribution functions (RPDFs) for the CB edge eigenstate in ordered $Ge_{63}C_1$ (solid red line), $Ge_{511}C_1$ (solid green line) and $Ge_{1727}C_1$ (solid blue line) supercells. In each case the dashed line of the same colour shows the calculated RPDF for the CB edge eigenstate $|L^{(0)}_{1c}(A_1)\rangle$ of the corresponding Ge_N host matrix supercell and the distance from the C atom is normalised such that the farthest central cell distance from the C is scaled to be 1.

eigenstate retains primarily indirect character, irrespective of the specific choice of supercell(s) employed in electronic structure calculations. This conclusion is in direct agreement with the hybrid functional DFT calculations of Kirwan et al. [41].

3.3.3 Trends versus C composition: band mixing and the ultra-dilute (impurity) limit

Having investigated in detail the impact of C incorporation in small ordered supercells containing ≤ 128 atoms, we turn our attention now to the evolution of the alloy CB edge state and band gap as we approach the ultra-dilute limit of having an isolated substitutional C atom in a Ge matrix. The results of these calculations are summarised in Fig. 3.3, which shows the calculated variation with x of (a) the band gap reduction ΔE_g (upper panel) and band gap pressure coefficient $\frac{dE_g}{dP}$ (lower panel), and (b) the Ge $\Gamma_{2'c}$ character (upper panel) and Ge $L_{1c}(A_1)$ (lower panel) character of the $\mathbf{K} = 0$ CB edge eigenstate. Results are shown for ordered $Ge_{N-1}C_1$ supercells containing $16 \leq N \leq 2000$ atoms: the lowest (highest) C composition investigated is $x = 0.05\%$ ($x = 6.25\%$) in an ordered $10 \times 10 \times 10$ FCC $Ge_{1999}C_1$ ($2 \times 2 \times 2$ FCC $Ge_{15}C_1$) supercell. Results for $n \times n \times n$ FCC supercells having even (odd) values of n are denoted in Figs. 3.3(a) – 3.3(d) by closed (open) circles. We recall that for odd n FCC supercells the L points of the Brillouin zone associated with the underlying diamond lattice do not fold to $\mathbf{K} = 0$, so that C-induced $\Gamma_{2'c}$-L_{1c} mixing is blocked in these supercells.

Examining Fig. 3.3(a) we note that, in general, C incorporation drives a strong reduction of the $\mathbf{K} = 0$ supercell band gap, with the magnitude of the band gap reduction ΔE_g growing strongly with increasing x (decreasing N). The lowest band gap we calculate is $E_g = 0.599$ eV in a $Ge_{15}C_1$ supercell, which is reduced by 257 meV compared to the fundamental (indirect) band gap of Ge. For some large (ultra-dilute) supercells we calculate a band gap at the folded Γ point which exceeds the fundamental L_{1c}-$\Gamma_{25'v}$ band gap of the Ge host matrix. We emphasise that this is a result of the L_{1c} states not folding to $\mathbf{K} = 0$ in these supercells: the lowest energy CB states in these supercells originate from wave vectors $\mathbf{k} = (\frac{(n-1)\pi}{na}, \frac{(n-1)\pi}{na}, \frac{(n-1)\pi}{na})$ located along the Λ direction in the primitive unit cell Brillouin zone, and hence lie higher in energy than the L_{1c} CB minima. For sufficiently low x, C-induced hybridisation of A_1-symmetric Ge CB edge states is insufficient to push the fundamental band gap below that of Ge. Closed red squares in the bottom panel of Fig. 3.3(a) show the values of $\frac{dE_g}{dP}$ calculated via hybrid functional DFT by Kirwan et al. [41]. Generally, we find that our TB-calculated pressure coefficients are ≈ 1 meV kbar^{-1} larger than those obtained from equivalent hybrid functional DFT calculations. This indicates a tendency of the TB calculations to overestimate the Ge $\Gamma_{2'c}$ character, or underestimate the $X_{1c}(A_1)$ character associated with the $Ge_{1-x}C_x$ alloy CB edge, emphasising the robustness of our conclusions regarding the indirect nature of the alloy band gap.

Turning our attention to Fig. 3.3(b), we again note that the precise calculated value of $\frac{dE_g}{dP}$ depends on the specific details of band mixing – as determined by zone folding – in a given alloy supercell. For all supercells the calculated values of $\frac{dE_g}{dP}$ remain significantly closer to the value 4.66 meV kbar^{-1} associated with the L_{1c}-$\Gamma_{25'v}$ indirect band gap of Ge, than to the value 13.33 meV kbar^{-1} associated with the direct $\Gamma_{2'c}$-$\Gamma_{25'v}$ band gap. This emphasises that the $Ge_{1-x}C_x$ band gap retains primarily indirect character, even for C compositions as high as $x = 6.25\%$.

The indirect nature of the $Ge_{1-x}C_x$ band gap is further emphasised by analysing the evolution of the calculated Ge $\Gamma_{2'c}$ and $L_{1c}(A_1)$ character of the $Ge_{N-1}C_1$ CB edge eigenstates, shown respectively in the upper and lower panels of Fig. 3.3(b). Note the absence of open circles in the lower panel of Fig. 3.3(b): since the L-point eigenstates in an odd n supercell do not fold to $\mathbf{K} = 0$, the Ge L_{1c} eigenstates can not contribute to the $\mathbf{K} = 0$ supercell eigenstates. As x decreases (N increases) towards the ultra-dilute limit, we note that the CB edge Ge $\Gamma_{2'c}$ character tends towards zero. Similarly, we note that the CB edge Ge $L_{1c}(A_1)$ character tends to increase with decreasing x. While the CB edge Ge $\Gamma_{2'c}$ character reaches a value as low as 0.3% in the largest $Ge_{1999}C_1$ supercell considered, we note that the corresponding Ge $L_{1c}(A_1)$ character attains a value 93.1% in the same supercell. This reflects that, for the case of an isolated substitutional C atom, the CB edge state consists primarily of a linear combination of Ge L_{1c} states having A_1 symmetry at the C lattice site, and also contains a small admixture of other (non-$\Gamma_{2'c}$) A_1-symmetric linear combinations of Ge states. The largest calculated alloy CB edge Ge $\Gamma_{2'c}$ character in an even n supercell is 21.9% in $Ge_{15}C_1$ ($x = 6.25\%$), suggesting that ordered $Ge_{1-x}C_x$ structures acquire minimal direct-gap character even as the C composition is increased beyond the dilute regime. We note higher Ge $\Gamma_{2'c}$ character in the 216-atom $Ge_{215}C_1$ ($x = 0.46\%$) supercell, but recall from

Fig. 3.3(a) that the lowest energy CB state at $\mathbf{K} = 0$ in this supercell lies above the Ge L_{1c} CB edge.

For small ($N \leq 128$) supercells we note that our calculated values of ΔE_g and $\frac{dE_g}{dP}$ are in good quantitative agreement with the hybrid DFT calculations of Ref. [41]. Our calculated CB structure for an ordered $Ge_{127}C_1$ supercell is also in good overall agreement with the calculations of Kirwan et al. [41], as well as those of Stephenson et al. [39]. At higher C compositions our calculations disagree qualitatively with the hybrid DFT calculations of Ref. [39], which suggest that the alloy band gap has closed even in a $Ge_{53}C_1$ ($x = 1.85\%$) supercell. We note however that the $Ge_{53}C_1$ supercell band structure presented in Ref.[39] contains several unusual features, including a large energy splitting of the VB edge states. This VB edge splitting, which should vanish in an ordered alloy supercell, suggests improper supercell relaxation, casting doubt on the suggestion that the band gap closes in the C composition range between 1.56% (in $Ge_{63}C_1$) and 1.85% (in $Ge_{53}C_1$).

3.3.4 Evolution of conduction band edge eigenstates in ordered alloy supercells

Having considered in detail the character of the CB edge eigenstates, we finally consider their localisation in response to C incorporation. The solid red, green and blue lines in Fig. 3.3(c) respectively show the calculated cumulative radial probability distribution function (RPDF) associated with the CB edge eigenstates in $Ge_{63}C_1$ ($x = 1.56\%$), $Ge_{511}C_1$ ($x = 0.19\%$) and $Ge_{1727}C_1$ ($x = 0.06\%$) – i.e. $2 \times 2 \times 2$, $4 \times 4 \times 4$ and $6 \times 6 \times 6$ SC – supercells. Here, the cumulative RPDF is calculated for a given supercell eigenstate by selecting the C lattice site as the origin of coordinates and then, at a given distance from this origin, adding the total probability density residing on atoms located at that distance from the C lattice site. For a given supercell eigenstate the rate at which the cumulative RPDF approaches a value of unity gives an indication of the degree of localisation of the state. As such, for an eigenstate strongly localised about the C lattice site, we would expect the calculated cumulative RPDF in Fig. 3.3(c) to rapidly approach its maximum value with increasing distance. To facilitate comparison of RPDFs calculated for eigenstates of supercells having different size, we plot the RPDF as a function of distance normalised to the maximum interatomic distance in each supercell – i.e. normalised by the dimensions of a given supercell. For a highly localised state, we would then expect the cumulative RPDF to approach unity more rapidly with increasing supercell size in Fig. 3.3(c).

To quantify the presence of any localisation generated by C incorporation, we show also in Fig. 3.3(c) the cumulative RPDFs associated with the constructed host matrix CB edge eigenstate $|L_{1c}^{(0)}(A_1)\rangle$ for the Ge_{64} (dashed red line), Ge_{512} (dashed green line) and Ge_{1728} (dashed blue line) supercells. We note that these $|L_{1c}^{(0)}(A_1)\rangle$ host matrix CB edge states extend through the full supercell: in a given N-atom Ge_N supercell the associated cumulative RPDF therefore increases smoothly in magnitude with increasing distance from the lattice site on which the eigenstate has been constructed to have purely s-like orbital character. Considering firstly the cumulative RPDF associated with the Ge_{64} CB edge eigenstate, we calculate that 10% of the probability density

associated with $|L_{1c}^{(0)}(A_1)\rangle$ resides on the origin and its four nearest-neighbour lattice sites. Substituting the Ge atom at the origin by C, this increases to 18% for the corresponding $Ge_{63}C_1$ ($x = 1.56\%$) supercell. Based solely on analysis of small supercell eigenstates, it then appears that C incorporation generates appreciable electron localisation at the CB edge. However, this trend is not borne out in the larger supercells: in both $Ge_{511}C_1$ and $Ge_{1727}C_1$ we calculate that the associated increase in localisation compared to the $|L_{1c}(A_1)\rangle$ host matrix CB edge state is $< 5\%$.

To quantify the overall change in localisation in response to C incorporation, we have also calculated the inverse participation ratio (IPR) associated with the CB edge eigenstates in all supercells studied[148, 149]. The IPR is calculated as

$$IPR = \frac{\sum_i |\psi(\mathbf{r_i})|^4}{\left(\sum_i |\psi(\mathbf{r_i})|^2\right)^2} \tag{3.2}$$

where $\psi(\mathbf{r_i})$ is the wave function at atom i. The IPR associated with an eigenstate in an N-atom supercell attains a minimum value of $\frac{1}{N}$ for a fully delocalised eigenstate having equal probability density at each lattice site, and a maximum value of 1 for a fully localised eigenstate for which the probability density resides entirely at a single lattice site. The calculated IPR for the $Ge_{N-1}C_1$ CB edge eigenstate tends towards an average value $\approx \frac{2}{N}$ in the ultra-dilute limit, a minimal increase from the value $\frac{1.62}{N}$ calculated for the corresponding $|L_{1c}^{(0)}(A_1)\rangle$ host matrix eigenstate. Similar analysis for higher energy alloy CB states reveals qualitatively similar results: incorporation of an *isolated* substitutional C atom in Ge does not lead to any significant electron localisation about the C atom. (As we will describe in section 3.4.3 below, this is no longer the case in the presence of C clustering, which can result in significant localisation of electrons occupying states lying energetically within the Ge band gap.)

The strong CB edge localisation observed in calculations for small ordered $Ge_{N-1}C_1$ supercells [41] then gives way to a delocalised alloy CB edge in the ultra-dilute (large N) limit. This is in stark contrast to equivalent analysis of dilute nitride $GaN_x(As,P)_{1-x}$ alloys[150, 151], to which $Ge_{1-x}C_x$ has recently been compared, where substitutional N incorporation generates N-related impurity states which are found to be highly localised about the N lattice site in the ultra-dilute limit. Based on the calculated high Ge $L_{1c}(A_1)$ character of the $Ge_{1-x}C_x$ CB edge eigenstates this lack of strong localisation is not surprising: the alloy CB edge is formed primarily from a linear combination of a small number of delocalised Ge eigenstates, and is hence itself delocalised. As such, we conclude that dilute C incorporation in Ge does *not* introduce significant electron localisation about substitutional C atoms, which are spaced widely apart in ordered alloy supercells.

On the basis of our analysis of the electronic structure of ordered $Ge_{1-x}C_x$ alloy supercells we conclude overall that – despite the large mismatch in size and chemical properties between Ge and C – from the perspective of the electronic structure an *isolated* C atom does not act as an isovalent impurity when incorporated substitutionally in Ge. Our analysis explicitly rules out the interpretation of the $Ge_{1-x}C_x$ CB structure in terms of C-related localised impurity states and the BAC model. Moreover, our analysis therefore suggests – in agreement with the conclusions of

Kirwan et al. [41] – that substitutional C incorporation in Ge does *not* drive the formation of a direct band gap in dilute $Ge_{1-x}C_x$ alloys.

3.4 Impact of C incorporation on conduction band edge states in disordered $Ge_{1-x}C_x$ alloys

3.4.1 Motivation and supercell selection

Having quantified the impact of C incorporation on the electronic structure of ordered $Ge_{1-x}C_x$ alloy supercells, we turn our attention now to more realistic, disordered alloy supercells. To date most analysis of $Ge_{1-x}C_x$ alloys have focused on ordered alloy structures which neglect disorder effects. Given the importance of disorder effects in other HMAs this neglection of disorder represents a short coming of the current literature. Here we set out to specifically include disorder effects and determine their impact on the CB edge states of $Ge_{1-x}C_x$.

To analyse the electronic structure in the presence of alloy disorder, two key requirements guide our choice of supercells. Firstly, we must choose sufficiently large supercells so that incorporation of dilute C compositions $x \sim 1\%$ correspond to substitution of multiple C atoms. This allows for the formation of disordered local neighbour environments in the supercell, and hence allows alloy disorder effects to be explicitly included in our electronic structure calculations. Secondly, since we have identified that C incorporation drives hybridisation between Ge host matrix states lying close in energy to the CB edge, it is important that we choose supercells which accurately reflect this band mixing as it occurs in a real $Ge_{1-x}C_x$ alloy. In supercell calculations, more states fold back to $\mathbf{K} = 0$ close in energy to the CB edge as the supercell size increases, providing a more accurate representation of C-induced band mixing.

Based on the analysis of section 3.3.3 – showing that the electronic properties associated with an isolated C impurity have converged for $N \approx 2000$ atoms in the supercell – we therefore use 1728-atom ($6 \times 6 \times 6$ SC) $Ge_{1728-M}C_M$ ($x = \frac{M}{1728}$) supercells, and perform calculations for supercells containing up to $M = 35$ substitutional C atoms ($x \approx 2\%$). To obtain a reliable description of the evolution of the electronic structure with x, we perform a high-throughput analysis: at each C composition we construct, relax and calculate the electronic structure of 25 distinct disordered supercells, where Ge atoms are substituted by C at randomly selected lattice sites. Results for a given C composition are then obtained via configurational averaging – i.e. by averaging over the results of calculations for these 25 distinct disordered supercells.

3.4.2 Band structure of disordered $Ge_{1-x}C_x$ alloy supercells

Before investigating the evolution of the character of the CB edge states with composition in disordered supercells we first calculate the band structure of a select disordered 1728 atom $Ge_{1-x}C_x$ supercell with a composition of 2%. This $6 \times 6 \times 6$ supercell will have a heavily folded band

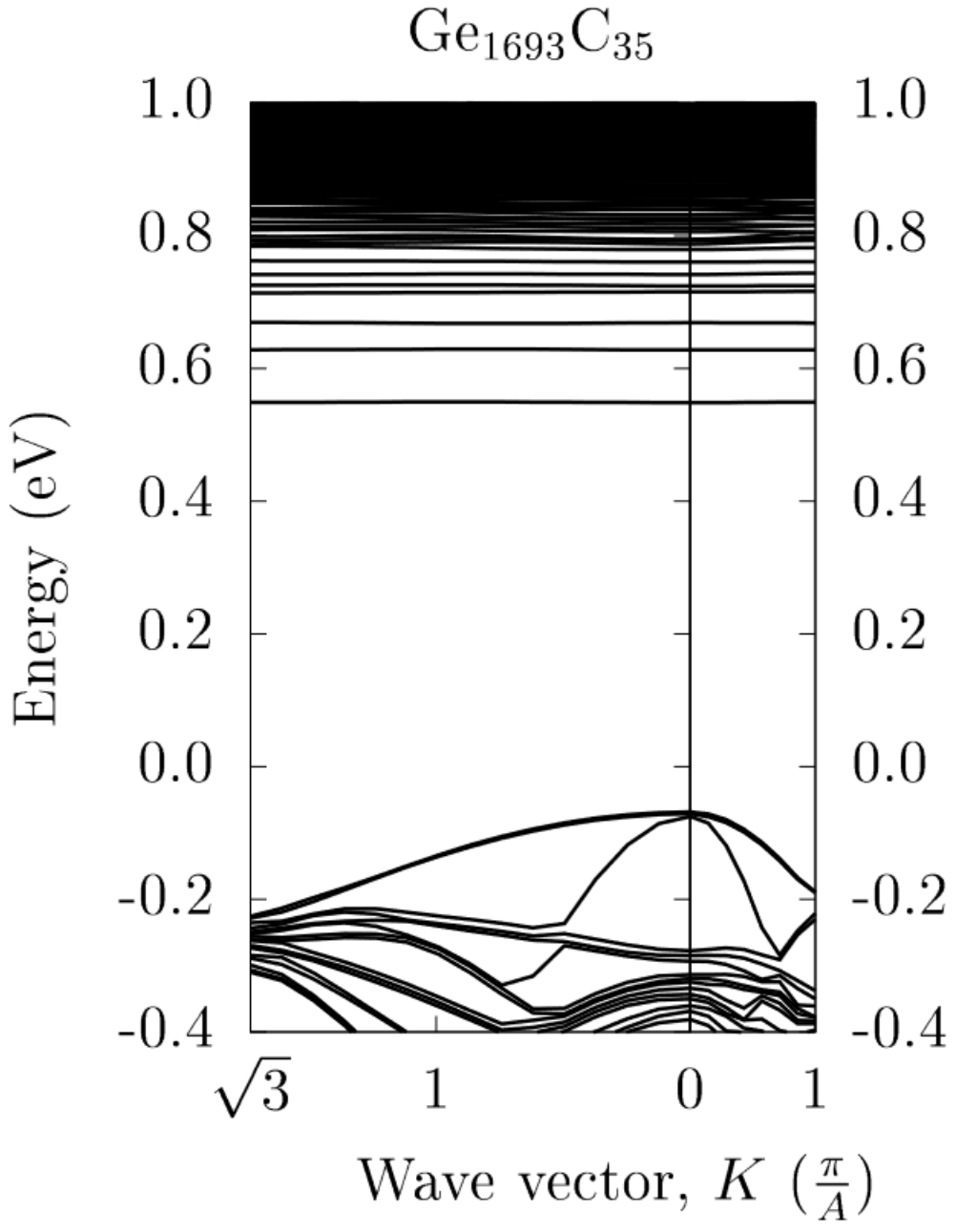

FIGURE 3.4: Calculated CB and VB structure for a $Ge_{1694}C_{34}$ supercell. Band structure figures are given along two directions, along (111) towards L on the left hand side and along (001) towards X on the right hand side of each figure.

structure making it difficult to select individual bands. In Fig. 3.4 we plot the band structure of this supercell. We note that the CB minimum state possesses minimal dispersion and is essentially a flat band, this arises because the C state is highly localised, therefore C states in neighbouring cells do not overlap and hence there is no dispersion in the calculated C state band. The C state is therefore made up of bulk Ge states with a range of k values. By contrast, the highest valence bands will have a dispersion similar to that seen in Ge, indicating that they each have a well defined k value, made up primarily of the Ge bulk state with the given k value. There is no reason to expect the C state to have any significant change or increase in its k character as you move away from the zone centre, and hence its optical behaviour will not change significantly across the

flat band, indicating that the CB edge contains minimal direct gap character. Further we can see that a number of states have formed within the band gap of Ge; these are likely due to C clusters forming in the supercell as will be shown in the next section. At higher energies disorder leads to a lifting of degenerecies, forming a spectrum of states that again have low dispersion and hence indirect behaviour. This band structure indicates that in disordered $Ge_{1-x}C_x$ alloys the CB edge retains primarily indirect gap character.

3.4.3 Evolution of conduction band edge states in disordered $Ge_{1-x}C_x$ alloys

The configurational averaging approach is favourable here compared to the use of a single, ultra-large supercell at each distinct C composition, due to the localised nature of the alloy CB states in *disordered* $Ge_{1-x}C_x$ alloys (described below). In conventional semiconductor alloys, which display minimal carrier localisation, eigenstate formation arises from the (generally weak) hybridisation of delocalised eigenstates, therefore requiring ultra-large supercells to quantitatively describe the resultant alloy properties by directly encapsulating the associated length scales[152]. Conversely, highly-mismatched alloys are characterised by effects pertaining to carrier localisation and short-range alloy disorder, which act on significantly reduced length scales. Supercells containing $N \sim 10^3$ atoms are therefore sufficient to describe the properties of such materials, with configurational averaging providing an efficient means to explore the impact of the formation of distinct short-range (near-neighbour) environments on the electronic structure[138, 139, 153, 154].

As in sections 3.3.2 – 3.3.4 above, our primary concern is to quantify the evolution of the character of the alloy CB states with increasing x. To do this, we use the $\Gamma_{2'c}$ and folded L_{1c} states $|\Gamma^{(0)}_{2'c}\rangle$ and $|L^{(0)}_{1c}\rangle$ of the Ge_{1728} host matrix supercell to calculate the fractional Ge $\Gamma_{2'c}$ and L_{1c} character spectra of the $Ge_{1728-M}C_M$ $\mathbf{K} = 0$ CB eigenstates. To average the calculated spectra at fixed x we sort the calculated Ge $\Gamma_{2'c}$ and L_{1c} character into energy intervals of width 5 meV: for each distinct disordered supercell a given energy interval is populated by the total Ge $\Gamma_{2'c}$ or L_{1c} character of alloy CB states lying in the range of energy spanned by the interval, and the resulting totals for all 25 supercells are then averaged to obtain the average Ge $\Gamma_{2'c}$ or L_{1c} character in that energy range. The results of this analysis are summarised in Figs. 3.5(a) – 3.5(h), which show the calculated evolution with x of the averaged fractional Ge $\Gamma_{2'c}$ (green) and L_{1c} (orange) character for the disordered 1728-atom $Ge_{1-x}C_x$ supercells described above. The C compositions in Fig. 3.5 begin at $x = 0$ for the C-free Ge_{1728} host matrix supercell in Fig. 3.5(a), and increase in steps of $M = 5$ C atoms in subsequent panels up to a maximum C composition $x = 2.03\%$ ($M = 35$) in fig. 3.5(h). Note the different scales on the abscissae of Figs. 3.5(a), 3.5(b), and 3.5(c) – 3.5(h).

Beginning in Fig 3.5(a) with the reference Ge_{1728} supercell, the lowest energy $\mathbf{K} = 0$ CB states are the fourfold degenerate folded L_{1c} states which possess 100% Ge L_{1c} character, while the next lowest energy CB state is the $\Gamma_{2'c}$ state which possesses 100% Ge $\Gamma_{2'c}$ character. Next, Fig. 3.5(b) shows the corresponding spectra calculated and averaged for $Ge_{1723}C_5$ ($x = 0.29\%$) supercells. We firstly observe, as in our ordered supercell calculations (section 3.3.2), that C incorporation generates a downward shift in energy of CB states possessing Ge L_{1c} character, reflecting the

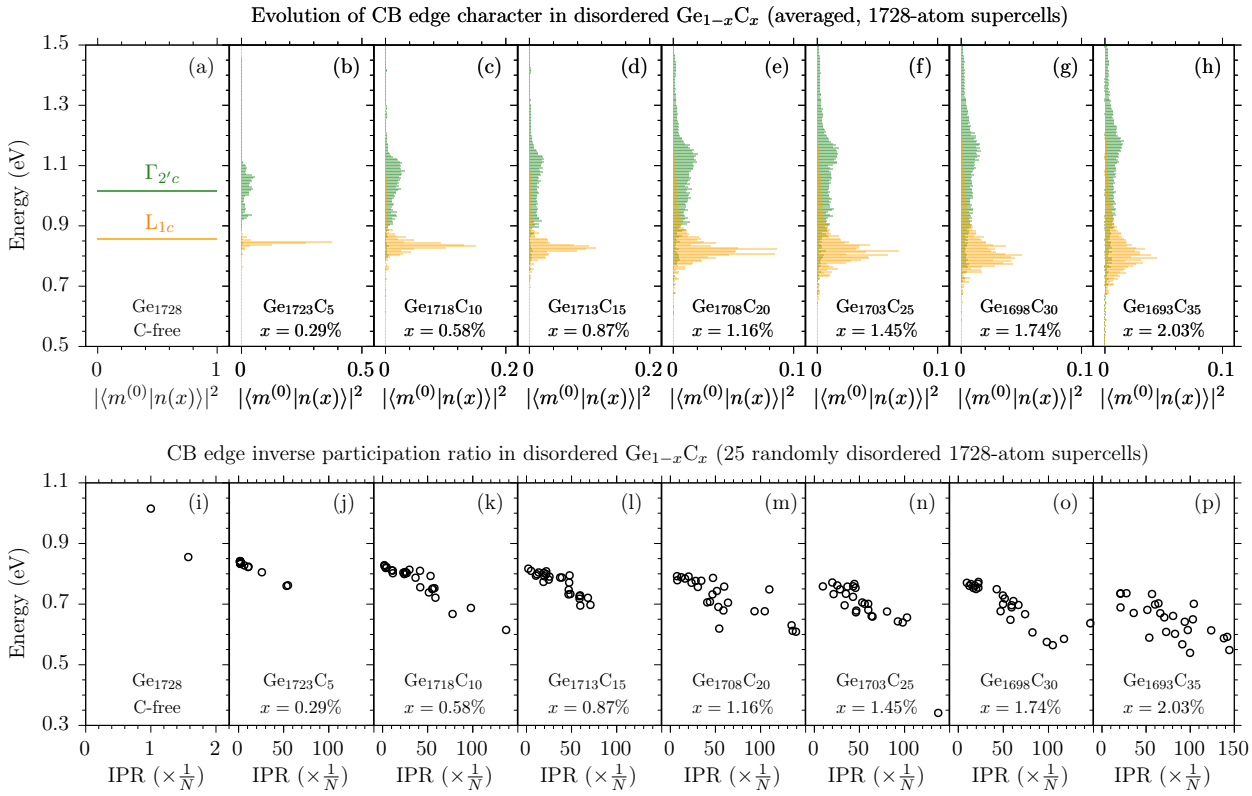

FIGURE 3.5: Top row: Evolution of the character of the alloy CB edge states in 1728-atom disordered $Ge_{1-x}C_x$ supercells. (a) Fractional Ge $\Gamma_{2'c}$ (green) and L_{1c} (orange) character spectra for a C-free Ge_{1728} ($6 \times 6 \times 6$ SC) supercell, calculated respectively by projecting the Ge_{1728} CB edge eigenstate $|m^{(0)}\rangle = |\Gamma^{(0)}_{2'c}\rangle$ or $|L^{(0)}_{1c}\rangle$ onto the full set of supercell zone-centre ($\mathbf{K} = 0$) eigenstates. (b) – (h) respectively show the fractional Ge $\Gamma_{2'c}$ and L_{1c} character spectra for a series of disordered, 1728-atom $Ge_{1728-M}C_M$ supercells having $M = 5$ – 35, in steps of 5 C atoms, corresponding respectively to C compositions $x = 0.29\%$, 0.58%, 0.87%, 1.16%, 1.45%, 1.74% and 2.03%. Note the difference in scales on the abscissae of panels (a), (b), (c) – (d), and (e) – (h). Bottom row: Calculated energy and IPR of the CB edge eigenstate in the 25 distinct, randomly disordered 1728-atom $Ge_{1728-M}C_M$ supercells for which averaged data are presented in the top row. (i) shows the calculated energies and IPRs of the $|\Gamma^{(0)}_{2'c}\rangle$ and $|L^{(0)}_{1c}(A_1)\rangle$ states in C-free Ge_{1728}. (j) – (p) respectively show the alloy CB edge energies and IPRs calculated for supercells having C compositions $x = 0.29\%$, 0.58%, 0.87%, 1.16%, 1.45%, 1.74% and 2.03%. Note the difference in scales on the abscissae of panels (i) and (j) – (p).

introduction of primarily Ge L_{1c}-derived states lying energetically within the Ge band gap. We also observe broadening of the energy range within which the Ge L_{1c} character resides. This strong energetic broadening of the CB edge Bloch character is a consequence of C-related alloy disorder. In ordered alloy supercells containing only a single substitutional C impurity, the Born-von Karman boundary conditions generate an ordered alloy in which the C atoms are arranged on a regular grid – determined by the supercell lattice vectors – and the underlying cubic symmetry of the diamond lattice is preserved. The calculated Ge character for ordered supercells then resides only on discrete alloy states (cf. Fig. 3.2), with the associated spectral features having zero width in energy. Substitution of multiple C atoms at randomly selected lattice sites to form a disordered alloy supercell results in short-range structural disorder, breaking the underlying cubic symmetry. This reduction in symmetry, associated with the presence of a wide range of C local neighbour environments, leads in general to the lifting of degeneracies and, in the case of highly-mismatched

alloys such as $Ge_{1-x}C_x$, to strong dependence of the calculated electronic properties, including the CB edge energy, on the precise short-range disorder present in a given alloy supercell. The Ge $\Gamma_{2'c}$ and L_{1c} character is then broadened and spread over a continuous energy range in a real $Ge_{1-x}C_x$ alloy, with the degree of energetic broadening reflecting the sensitivity of the electronic structure to short-range structural disorder.

Turning our attention to the averaged Ge $\Gamma_{2'c}$ character in Fig. 3.5(b), we observe extremely strong energetic broadening. While the Ge L_{1c}-related feature remains sharply defined in energy, we find that alloy disorder gives rise to strong intrinsic inhomogeneous broadening of the Ge $\Gamma_{2'c}$ character. At this C composition $x = 0.29\%$ we find that the maximum Ge $\Gamma_{2'c}$ character residing within a single 5 meV energy interval is 5.4%. We note that this is in contrast to the results shown in Figs. 3.2(c), 3.2(h) and 3.2(m) for small ordered supercells containing a single C atom, where the Ge $\Gamma_{2'c}$ character resides on only a small number of alloy CB levels. Our calculations therefore suggest that C-related alloy disorder leads to strong inhomogeneous energetic broadening of the Ge $\Gamma_{2'c}$ character. Similarly to the ordered supercell calculations of section 3.3.2, we find that states lying in the same energy interval generally possess an admixture of both Ge $\Gamma_{2'c}$ and L_{1c} character – i.e. they are hybridised states formed of a linear combination of Ge host matrix states. The $\Gamma_{2'c}$ character is found predominantly at higher energies, with only a limited amount of $\Gamma_{2'c}$ character mixing into the lowest energy CB states. By comparison, we find that the alloy supercell VB edge states (not shown) retain strong Ge $\Gamma_{25'v}$ character and display comparatively minor energetic broadening, reflecting that C incorporation has minimal impact on the VB structure.

As x is further increased, we note the continuation of this general trend. Firstly, the feature associated with the Ge L_{1c} character is both shifted downwards and increasingly broadened in energy with increasing x. Secondly, we observe extremely strong inhomogeneous broadening of the Ge $\Gamma_{2'c}$ character, which becomes spread over a broad range of energies at and above the CB edge in a given alloy supercell. Thirdly, we note that states lying close in energy to the alloy CB edge acquire minimal Ge $\Gamma_{2'c}$ character and remain primarily Ge L_{1c}-derived. This describes that the fundamental alloy band gap remains primarily indirect in character, similar to that in Ge, but that spectral features associated with this band gap undergo strong inhomogeneous broadening in the presence of alloy disorder. Again, we note that this behaviour is markedly different to that expected on the basis of the BAC model, whereby a direct band gap would be expected to emerge via the transfer of increasing Ge $\Gamma_{2'c}$ character to the alloy CB edge with increasing C composition x. In general, the results of our disordered alloy analysis support the conclusions of Kirwan et al. [41], and of our ordered supercell analysis in section 3.3.3 above: dilute C incorporation in Ge does *not* give rise to a direct band gap. Given the small $\Gamma_{2'c}$ character associated with individual $Ge_{1-x}C_x$ CB states, we do not expect strong optical matrix elements and direct-gap optical recombination between these states and the VB edge.

Finally, the calculated strong inhomogeneous broadening of the Ge $\Gamma_{2'c}$ and L_{1c} character suggests the formation of a distribution of C-related localised states close in energy to the CB edge in $Ge_{1-x}C_x$ alloys. Given that an isolated C impurity generates minimal localisation at the CB edge (section 3.3.4), this suggests that C-related alloy disorder – i.e. the formation of nearest-neighbour

C-C pairs and even near-neighbour C pairs, as well as larger clusters of neighbouring C atoms – can generate significant electron localisation. To ascertain the extent to which this is the case, at each C composition x we have computed the IPR associated with the lowest energy CB eigenstate in each of the 25 randomly disordered $Ge_{1728-M}C_M$ supercells for which averaged data are presented in Figs. 3.5(a) – 3.5(h). The calculated energies and IPRs of these states are shown in Figs. 3.5(i) – 3.5(p). Recalling that a larger IPR reflects stronger localisation, we firstly note a general trend in the calculated IPRs for distinct supercells at fixed x: the IPR associated with a given eigenstate tends to increase strongly with decreasing eigenstate energy. This reflects the emergence of tightly-bound C-related cluster states lying deep within the Ge host matrix band gap in energy – related predominantly here to the presence of C atoms in close proximity to one another – similar to the distribution of N-related cluster states in dilute nitride $GaN_x(As,P)_{1-x}$[133, 153]. Secondly, we note that the localisation of the lowest energy CB state in $Ge_{1-x}C_x$ tends on average to increase with increasing x, reflecting the formation of more localised states in response to the closer proximity of substitutional C atoms at higher C compositions. Thirdly, at fixed x we note the spread in energy of the lowest energy CB state in distinct randomly disordered supercells, which tends to increase with increasing x and is $\gtrsim 0.2$ eV for the highest C composition considered. This accounts for the strong inhomogeneous broadening of the CB states observed in Figs. 3.5(a) – 3.5(h), and confirms that the strong sensitivity of the electronic structure to short-range alloy disorder is a consequence of electron localisation about clusters of substitutional C atoms. As an extreme example of this localisation we note that the CB edge eigenstate in one of the $Ge_{1703}C_{25}$ ($x = 1.45\%$) supercells considered has both a markedly low energy of 0.341 eV and a high IPR of $\frac{137}{N}$ (visible in the bottom right-hand corner of Fig. 3.5(n)). Further inspection reveals that this highly localised eigenstate is associated with the presence of a C-Ge-C-Ge-C nearest-neighbour chain in the supercell, about which the calculated eigenstate is strongly localised (with its probability density distributed over only $\left(\frac{137}{N}\right)^{-1} \approx 13$ atoms in total).

3.5 Implications for device applications

Previous analysis has suggested the emergence of a direct band gap in dilute $Ge_{1-x}C_x$ alloys, and that the resulting alloy band structure should produce performance in $Ge_{1-x}C_x$-based semiconductor lasers and modulators which is comparable to that in conventional direct-gap III-V semiconductor materials[38]. Conversely, the results of our detailed analysis of electronic structure evolution in $Ge_{1-x}C_x$ alloys have strongly negative implications from the perspective of potential device applications.

Firstly, our calculations for ordered alloy supercells suggest that the large differences in size and electronegativity between C and Ge drives hybridisation between Ge host matrix states lying close in energy to the CB edge. While this C-induced band mixing results in the transfer of some direct (Ge $\Gamma_{2'c}$) character to the alloy CB edge, this direct-gap character in general remains minimal. Indeed, we confirmed that dilute $Ge_{1-x}C_x$ admits a "quasi-direct" band gap: while supercell

electronic structure calculations show the CB minimum to lie at $\mathbf{K} = 0$, the alloy band gap retains primarily indirect character.

Secondly, our analysis of large disordered alloy supercells also demonstrates strong sensitivity of the $Ge_{1-x}C_x$ electronic properties to the presence of short-range alloy disorder, behaviour typical of a highly-mismatched semiconductor alloy. In the presence of alloy disorder our calculations describe a breakdown of the CB edge Bloch character, leading to a broad distribution of C-related localised states lying below the Ge CB edge in energy. Individually, these states only possess small direct (Ge $\Gamma_{2'c}$) character, and so will not support appreciable direct-gap optical recombination. Further analysis would be required to estimate the magnitude of the optical recombination rate associated with these localised states in a realistic, disordered $Ge_{1-x}C_x$ alloy. Such analysis is beyond the scope of this work, but, based on the calculated $\Gamma_{2'c}$ distributions (cf. Fig. 3.5), we would expect a considerably lower radiative recombination rate in dilute $Ge_{1-x}C_x$ than would be found in a conventional direct-gap semiconductor.

From the perspective of carrier transport, experimental measurements for closely-related dilute $Si_{1-x}C_x$ alloys show significant degradation in electron mobility in response to C incorporation. Theoretical analysis by Vaughan et al. [46] has demonstrated that the electron mobility in dilute $Si_{1-x}C_x$ is limited not only by C-related alloy scattering, but also by electrically active crystalline defects. Based on our electronic structure analysis here, we similarly expect strong suppression of electron mobility in dilute $Ge_{1-x}C_x$ alloys. The identification in our disordered supercell calculations of strong inhomogeneous energetic broadening of the CB edge Bloch character reflects the presence of a distribution of localised states and indicates a breakdown of strict $\mathbf{k}$-selection. On this basis, we expect many scattering pathways to open up for electrons in the $Ge_{1-x}C_x$ CB, so that the electron mobility in the alloy is both strongly and intrinsically limited.

We emphasise that the conclusions drawn above are based solely on the results of our analysis of the electronic structure of idealised $Ge_{1-x}C_x$ alloys – i.e. purely substitutional, defect-free alloys. The presence of defects – e.g. in the form of C interstitials due to non-substitutional incorporation – will likely exacerbate limitations on the optical and transport properties. Overall, while dilute $Ge_{1-x}C_x$ alloys are of interest from a fundamental perspective due to their unusual electronic properties, we conclude that they are likely to be of limited value for applications in CMOS-compatible optoelectronic devices.

3.6 Conclusions

In summary, we have presented a theoretical analysis of electronic structure evolution in the group-IV dilute carbide alloy $Ge_{1-x}C_x$. Our calculations were based on a computationally efficient and highly-scalable semi-empirical atomistic framework, consisting of (i) structural relaxation using a VFF potential, and (ii) electronic structure calculations using a sp^3s^* TB Hamiltonian. Both the VFF potential and TB Hamiltonian were parameterised based on hybrid functional DFT calculations of the structural, elastic and electronic properties of the constituent diamond-structured

elemental semiconductors Ge, C, and the fictitious IV-IV compound semiconductor zb-GeC. The validity of this framework has been established by comparison to the results of hybrid functional DFT calculations for small alloy supercells containing up to 128 atoms, where good qualitative and quantitative agreement is found for the nature and evolution of the alloy band gap. Using this framework we investigated the evolution with C composition x of the electronic structure of idealised (ordered) and realistic (disordered) $Ge_{1-x}C_x$ alloys.

Recently, it has been suggested that C incorporation in Ge drives the evolution of a direct band gap via the formation of C-related localised impurity states, with these C-related states undergoing a BAC interaction with the extended Γ_{7c} zone centre CB edge state of the Ge host matrix semiconductor. Contrary to this suggestion, our calculations for ordered $Ge_{1-x}C_x$ alloys revealed the presence of weak C-induced mixing of Ge Γ_{7c} character into the alloy CB edge state. As such, rather than being formed via a BAC interaction of an admixture of a C-related localised impurity state, we showed that the CB edge in ordered $Ge_{1-x}C_x$ alloy supercells is predominantly formed of an A_1-symmetric (s-like) linear combination of the extended L_{6c} CB edge states of Ge. Consequently, we demonstrated that the $Ge_{1-x}C_x$ CB edge displays minimal localisation about C lattice sites as the ultra-dilute limit is approached. More recent research based on DFT calculations have continued to investigate the evolution of the dilute $Ge_{1-x}C_x$ alloys band structure through a BAC interaction but have highlighted the inability of the BAC model to fully describe the alloy CB structure[70, 71].

For large, disordered $Ge_{1-x}C_x$ alloy supercells we calculated the evolution of the electronic structure up to $x = 2\%$. Generally, we found that the lowest energy $Ge_{1-x}C_x$ alloy CB states acquire only a minimal admixture of Ge Γ_{7c} (direct-gap) character, while retaining predominantly Ge L_{6c} (indirect-gap) character. With increasing x our calculations revealed that C-related alloy disorder leads to strong inhomogeneous energetic broadening of the Bloch character associated with the CB edge states, due to the formation of a distribution of localised states, associated with C clustering and lying energetically within the Ge band gap. The formation of a distribution of localised states within the Ge band gap indicates that dilute $Ge_{1-x}C_x$ alloys are likely to possess intrinsically poor optical properties. On average, we calculated that the direct (Ge Γ_{7c}) character becomes distributed to higher energy alloy CB states with increasing C composition x, behaviour which is markedly different to that expected based on the BAC model.

In conclusion, rather than acquiring a direct band gap via a BAC interaction, our analysis demonstrates that the $Ge_{1-x}C_x$ CB edge attains minimal direct character. The C-induced band mixing identified by our calculations instead leads to the formation of a "quasi-direct" hybridised alloy band gap in the dilute C limit, which retains predominantly indirect (Ge L_{6c}) character, with a distribution of C localised states emerging within the Ge band gap in the presence of short-range alloy disorder. These general conclusions are in qualitative and quantitative agreement with those of recent analysis based on hybrid functional DFT calculations[41]. We therefore conclude that C incorporation in Ge does *not* give rise to a direct-gap semiconductor alloy, limiting the benefit of this material system for applications in optoelectronic devices.

Chapter 4

Origin of enhanced band to band tunneling in $Ge_{1-x}Sn_x$ alloys

4.1 Overview

In this chapter we investigate the electronic properties of the second group-IV alloy of interest in this thesis, $Ge_{1-x}Sn_x$. While for $Ge_{1-x}C_x$ we were primarily interested in determining the evolution of the direct gap with C composition, we know $Ge_{1-x}Sn_x$ possesses a direct fundamental band gap for Sn compositions greater than 6-9% Sn. emerging evidence indicates that a direct band gap emerges continuously with increasing x due to alloy band mixing and that the fundamental gap of $Ge_{1-x}Sn_x$ is in fact a hybridised band gap with both indirect and direct gap character. We are interested in how the hybridisation of the band gap impacts band to band tunneling in $Ge_{1-x}Sn_x$ and by extension the effect on tunneling field effect transistors which are based on band to band tunneling. Specifically we are interested in the evolution of the band to band tunneling generation rate as a key determinant of a viable TFET.

We begin this chapter with an overview of the latest research on the nature of the band gap of $Ge_{1-x}Sn_x$ alloys in section 4.2, where we describe the past modelling of the band structure of $Ge_{1-x}Sn_x$ and provide an overview of the latest developments in the literature. The key difference between the past and recent theoretical modelling is the transition from virtual crystal based models[155] to atomistic models[69]. Following on from the background in section 4.3 we will provide an overview of the theoretical models used to calculate the BTBT generation rate and their implementation. Two transport models will be used for generation rate calculation (1) an atomistic non-equilibrium Green's function (NEGF) approach to compute the generation rate and (2) a model $\mathbf{k}\cdot\mathbf{p}$ Hamiltonian of Sn-induced Γ_{7c}-L_{6c} hybridisation which, employed in conjunction with the Wentzel-Kramers-Brillouin (WKB) approximation, quantitatively reproduces G obtained from full NEGF calculations.

In section 4.4 we begin our analysis of BTBT in $Ge_{1-x}Sn_x$, initially we focus on ordered alloy supercells where Sn atoms are selectively placed to form a reoccurring pattern in the supercell such that random alloy disorder is reduced, this represents an ideal case. We begin with an analysis of the complex band structure as it is a key determinant of the BTBT generation rate. Then

in section 4.5 we calculate the ordered BTBT generation proper using the transport methods mentioned above. We investigate the impact of short range alloy disorder in section 4.5 using disordered $Ge_{1-x}Sn_x$ supercells and then in section 4.6 we investigate the evolution of the BTBT generation rate with disorder.

4.2 Band structure of $Ge_{1-x}Sn_x$

$Ge_{1-x}Sn_x$ represents a great hope of the semiconductor community for the formation of a direct gap group-IV alloy which will have many applications in integrated photonics, photodetectors and BTBT based TFETs. Consequently there has been great interest in determining evolution of the electronic bandstructure of $Ge_{1-x}Sn_x$ stretching back over 30 years[57]. Initial calculations in 1989 using the virtual crystal approximation (VCA) confirmed the formation of a direct gap at a Sn composition of 26%[57] where the direct Γ state passes below the indirect L state energy. However, to this day the exact crossover point remains an open question. Numerous reparameterisations of VCA band structure over the intervening years has lead to successive lowering of the predicted crossover energy to the range $x = 6$ – 9%[65–67]. However, recent analysis has cast doubt on the applicability of the VCA to the calculation of the $Ge_{1-x}Sn_x$ alloys band structure, recent DFT analysis has suggested that alloy effects such as band mixing and short range alloy disorder can have a large impact on the bandstructure[69]. Alloy effects lead to hybridisation of the VB edge states that causes the CB minimum state to acquire an admixture of indirect and direct gap character. This has been shown through hydrostatic pressure calculations, which can compare the pressure coefficient of the hybridised CB edge to the high symmetry points of Ge, as these symmetry points, Γ, L and X have different pressure coefficients. From theses calculations the pressure coefficient of the alloy CB edge was found to vary continuously from an indirect gap towards a direct gap pressure coefficient. Which conflicts with the single crossover point here the energy of the Γ state becomes lower than the indirect L state assumed in VCA based calculations.

4.3 Theory

4.3.1 Atomistic: tight-binding method and non-equilibrium Green's function

The aim of this study is to investigate the origin of enhanced BTBT in $Ge_{1-x}Sn_x$ alloys. This will be achieved by calculating carrier tunnelling through $Ge_{1-x}Sn_x$ alloys for different Sn compositions while the alloy is evolving from an indirect towards a direct gap material. The transport properties of the alloys will be investigated using long bulk-like supercells with periodic boundary conditions in directions perpendicular to the direction of transport, the [001] direction. Alloy effects will be investigated under two formats – ordered supercells and disordered supercells. In ordered supercells Sn atoms will be selectively placed in a Ge supercell such that each Sn atom is a fixed distance to all the next nearest Sn atoms, forming a periodic pattern of Sn atoms in the supercell. This periodic pattern represents an ideal situation which will serve to magnify the BTBT gains

produced by Sn while neglecting disorder effects. On the other hand disordered supercells more closely represent real structures where Sn atoms are randomly distributed throughout a supercell with no pattern to their placement. The electronic structure of these supercells will be modelled using an sp^3s^* TB Hamiltonian [68] with spin orbit coupling. The sp^3s^* TB model was chosen in lieu of the more accurate $sp^3d^5s^*$ Hamiltonian, because the band structure characteristics of primary interest was the hybridisation of the CB edge states, therefore we needed to accurately model the high symmetry points of the band structure for which the sp^3s^* Hamiltonian is suitable and the importance of spin orbit coupling in $Ge_{1-x}Sn_x$[68] necessitated its inclusion in the TB model. And for generation rate calculations we focus on the improvement in $Ge_{1-x}Sn_x$ BTBT relative to the Ge generation rate which would be similar for both TB models. Further the sp^3s^* model has a greatly reduced computational load compared to the $sp^3d^5s^*$ Hamiltonian. The TB model was parameterised for the individual $Ge_{1-x}Sn_x$ materials Ge, α-Sn and zinc blende GeSn, all benchmarked against DFT calculations. Additionally due to the large difference in atomic sizes between Ge and Sn, structural relaxation of alloy supercells well be required, in this case we use a VFF potential[104] to relax atoms. The relaxation was achieved using a VFF potential based on a modified form of a potential introduced by Musgrave and Pople[102]. Our VFF model was parameterised using DFT calculations and was implemented using the Large-scale Atomic/Molecular Massively Parallel Simulator[108, 109] (LAMMPS) to relax supercells and benchmark them against DFT calculations[104]. The TB/VFF framework enables efficient calculation of electronic properties for large supercells with up to 10^4 atoms.

In this work we will compare the band gaps of our atomistic tight-binding model with those of a virtual crystal approximation (VCA) based tight-binding model. The VCA we will use to calculate the parameters will be[156]

$$d^2_{alloy}V_i^{alloy} = xd^2_{Sn}V_i^{Sn} + (1-x)d^2_{Ge}V_i^{Ge} - \left(\frac{x(1-x)}{N}\right)^{\frac{1}{2}}(d^2_{Sn}V_i^{Sn} - d^2_{Ge}V_i^{Ge}) \tag{4.1}$$

Where the V_i^n are the TB interaction parameters and d_n are the interatomic distances. The last term of the Eq. (4.1) accounts for the bowing of the alloy band gap.

A schematic illustration of our calculational workflow for BTBT in $Ge_{1-x}Sn_x$ alloys is illustrated in Fig. 4.1(a). Our atomistic calculations employ a valence force field (VFF) potential to compute relaxed atomic positions in $Ge_{1-x}Sn_x$ alloy supercells, which are then used to construct the alloy supercell TB Hamiltonian. The relaxed-supercell TB Hamiltonian is then used to perform complex band structure calculations, and as input to a full-band atomistic NEGF solver, to compute the direct BTBT generation rate G. The VFF lattice relaxations and TB electronic structure calculations are based on those described in Ref. [68], where detailed benchmarking was undertaken against density functional theory (DFT) calculations for small alloy supercells.

Our alloy supercell lattice relaxations employ the VFF potential of Ref. [157], which is a fully analytic form of the non-polar potential introduced by Martin[103] and has been described in section 2.2.2. Our electronic structure calculations employ a nearest-neighbour sp^3s^* TB Hamiltonian[92],

including spin-orbit coupling[98]. The contribution to the alloy supercell TB Hamiltonian at a given lattice site is computed explicitly depending on the local relaxed atomic environment[68]. The on-site orbital energies are computed by averaging over the orbital energies associated with the elemental (Ge or α-Sn) or compound (zinc blende GeSn) materials formed by the on-site atom and each of its four nearest neighbours, including the natural VB offsets between these materials. The nearest-neighbour interatomic interactions are computed by explicitly accounting for changes in relaxed nearest-neighbour bond lengths and angles using, respectively, the generalised form of Harrison's rule and the Slater-Koster two-centre integrals[97]. Our bulk TB parameters for Ge, α-Sn and zinc blende GeSn have been fitted to reproduce the energies and hydrostatic deformation potentials, at selected high-symmetry points in the Brillouin zone, obtained from hybrid functional DFT calculations[68]. We note that the choice of a sp^3s^* TB basis reduces the accuracy of the description of the bulk band structure compared to a larger $sp^3d^5s^*$ basis, tending to overestimate CB and VB edge effective masses. However, our detailed benchmarking against DFT alloy supercell calculations for $Ge_{1-x}Sn_x$ alloys has demonstrated that an appropriately parameterised sp^3s^* TB Hamiltonian captures quantitatively the key features of the electronic structure, verifying its capability to make quantitative predictions of the alloy properties. [68] The use of a sp^3s^* rather than a $sp^3d^5s^*$ TB basis halves the order of the Hamiltonian matrix for a given supercell, thereby reducing the computational cost associated with the Hamiltonian diagonalisation by close to an order of magnitude, and hence allowing access to larger system sizes with reduced computational cost.

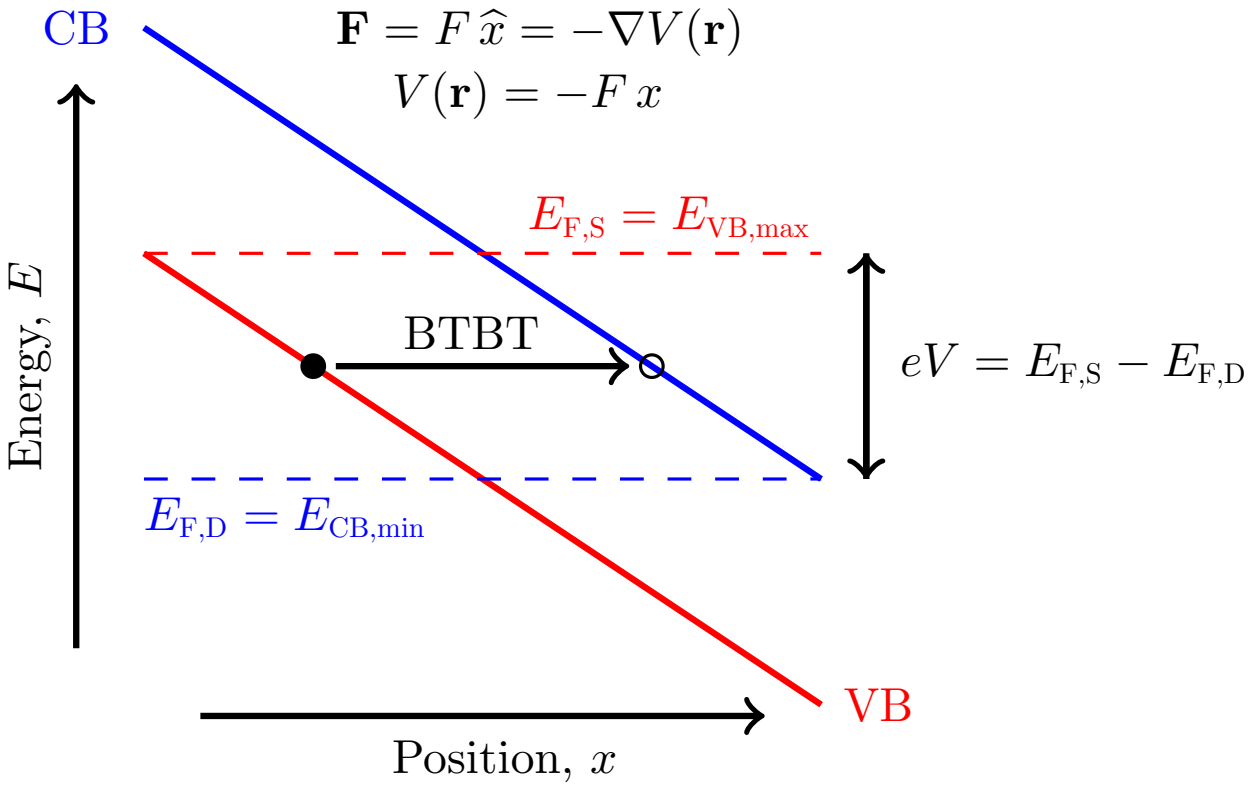

FIGURE 4.1: Schematic of BTBT generation rate calculations

Previous analysis of BTBT in Ge has demonstrated (i) that the BTBT generation rate is dominated

by direct (ballistic) BTBT, with minimal contribution from indirect (phonon-assisted) BTBT[14], and (ii) that the BTBT generation rate is largely independent of the orientation of the applied electric field[15]. We therefore restrict our attention to direct BTBT, which we compute for (100)-oriented intrinsic $Ge_{1-x}Sn_x$ alloy supercells with applied electric field along (100). Specifically, we analyse BTBT in realistic, disordered $Ge_{1-x}Sn_x$ alloys using supercells that are elongated along the (100) tunneling direction, along which direction open boundary conditions are applied[72], and employ periodic boundary conditions in the [100] plane. A schematic illustration of the calculational set-up is provided in Fig. 4.1(b). The complex band structure calculations – which elucidate the available evanescent Bloch states that provide pathways for direct BTBT – proceed on a "slab" basis, following the methodology of Chang and Schulman[114]. Here, a given supercell is dissected into slabs formed of the minimum number of atomic layers required to generate a nanowire of infinite length via translation along the tunneling direction, allowing to compute a "companion matrix" to the supercell Hamiltonian that can be diagonalised as a function of energy E to obtain the complex-valued supercell wave vectors $\mathbf{K}$. The complex band structure is then used in conjunction with a recursive NEGF algorithm to compute the BTBT current density J at fixed applied electric field strength F[158]. The calculated J is then used to compute the BTBT generation rate G via [15, 159]

$$G = \frac{JF}{qV}\,, \tag{4.2}$$

where V is the applied voltage generating the electric field F, $qV = E_{\mathrm{F,S}} - E_{\mathrm{F,D}}$ is the energetic width of the tunneling window, and $E_{\mathrm{F,S}}$ and $E_{\mathrm{F,D}}$ are respectively the source and drain Fermi levels (cf. Fig. 4.1(b)).

The complex band structure and NEGF BTBT calculations in this work were performed by implementing our sp^3s^* TB Hamiltonian for $Ge_{1-x}Sn_x$ alloys using the OMEN code[72, 160]. OMEN is a full-band quantum transport simulator, which solves the coupled Schrödinger-Poisson equations fully atomistically using a NEGF approach based on the TB method. The use of open boundary conditions[72], combined with efficient parallelisation strategies for energy and wave vector integration[160], allows OMEN to predicatively compute the electrical properties of realistically-sized transistor structures[15, 161–164].

4.3.2 Continuum: k·p method and WKB approximation

In Ref. [68] we demonstrated, using DFT and TB electronic structure calculations, that the evolution of the CB edge in ordered $Ge_{1-x}Sn_x$ alloys is characterised by Sn-induced hybridisation between the L_{6c} CB minimum and Γ_{7c} zone-centre CB edge states of Ge. Specifically, beginning with a N-atom Ge_N supercell and substituting a single Ge atom by Sn to form an ordered $Ge_{N-1}Sn_1$ ($x = N^{-1}$) alloy supercell, the resultant perturbation of the supercell Hamiltonian – due to chemical inhomogeneity and lattice relaxation – drives hybridisation between the zone-centre Ge CB edge state $|\Gamma_{7c}\rangle$ and a linear combination $|L_{6c}(A_1)\rangle$ of L-point Ge states having s-like (A_1)

symmetry at the Sn lattice site. To compute the portion of the complex band structure relevant to direct BTBT we begin with a 2-band (Kane) **k·p** Hamiltonian – describing the dispersion of the Γ-point CB and light-hole (LH) VB – and extend its basis to include $|\mathrm{L}_{6c}(A_1)\rangle$. To enable direct comparison to our atomistic calculations, we parameterise the resulting 3-band **k·p** Hamiltonian using the Ge band gaps and effective masses computed via the TB Hamiltonian of section 4.3.1.

We use the TB method to explicitly construct $|\mathrm{L}_{6c}(A_1)\rangle$, allowing in ordered $Ge_{N-1}Sn_1$ supercells to derive and parameterise the following 3-band **k·p** Hamiltonian – having basis states, in order, $|\mathrm{L}_{6c}(A_1)\rangle$, $|\Gamma_{7c}\rangle$ and $|\Gamma_{8v}\rangle$ – describing the Sn composition-dependent band edge energies and Γ_{7c}-L_{6c} hybridisation [40, 165]

$$H(x) = \begin{pmatrix} E(\mathrm{L}_{6c}) + \gamma x + \frac{\hbar^2}{2m_{\mathrm{L}}^*}\left(k_\parallel^2 + k_\perp^2\right) & \beta x & 0 \\ \beta x & E(\Gamma_{7c}) - \alpha x + \frac{\hbar^2}{2m_0}\left(k_\parallel^2 + k_\perp^2\right) & iP\sqrt{k_\parallel^2 + k_\perp^2} \\ 0 & -iP\sqrt{k_\parallel^2 + k_\perp^2} & \kappa x - b_{\mathrm{VB}}x^2 + \frac{\hbar^2}{2m_0}\left(k_\parallel^2 + k_\perp^2\right) \end{pmatrix}, \tag{4.3}$$

where P is the interband (Kane) momentum matrix element determining the Γ-point CB and LH effective masses, and m_{L}^* is the L-point density of states effective mass. Here, we have written the wave vector in terms of its components $k_\parallel$ and $k_\perp$ parallel and perpendicular to the (100) tunneling direction. The zero of energy is chosen to lie at the Ge VB edge, $E(\Gamma_{8v}) = 0$, so that $E(\mathrm{L}_{6c}) = 0.760$ eV and $E(\Gamma_{7c}) = 0.909$ eV are then respectively equal to the indirect (fundamental) L_{6c}-Γ_{8v} and direct Γ_{7c}-Γ_{8v} band gaps of Ge. [68] Based on our TB-calculated Ge band structure [68] we compute the Γ- and L-point CB edge effective masses $m_\Gamma^* = 0.053\,m_0$ and $m_{\mathrm{L}}^* = 0.762\,m_0$. Following Ref. [166], we choose $P = 7.866$ eV Å by requiring that m_Γ^* is exactly reproduced by the 2-band Γ-point Hamiltonian for the Ge host matrix semiconductor (obtained at $x = 0$ by removing the first row and column from Eq. (4.3)). The parameters $\gamma = 4.651$ eV, $\alpha = 1.325$ eV and $\kappa = 1.656$ eV respectively describe virtual crystal-type shifts to the L-point CB, Γ-point CB and Γ-point VB edge energies; $b_{\mathrm{VB}} = 2.473$ eV describes the bowing of the VB edge energy, and $\beta = 5.855$ eV describes the strength of the Sn-induced hybridisation between the $|\mathrm{L}_{6c}(A_1)\rangle$ and $|\Gamma_{7c}\rangle$ Ge CB edge states. [165]

Our calculation of the complex band structure admitted by Eq. (4.3) is based on the eigenvalue method of Chang and Schulman[114]. For a given Sn composition x we set $k_\perp = 0$ in Eq. (4.3) and write $H = H^{(0)} + H^{(1)}k_\parallel + H^{(2)}k_\parallel^2$, where $H^{(0)}$, $H^{(1)}$ and $H^{(2)}$ are the 3×3 coefficient matrices associated with terms in H that are respectively independent of $k_\parallel$, linear in $k_\parallel$, and quadratic in $k_\parallel$. The energy-dependent complex wave vectors $k_{\parallel,n}(E, 0)$ at $k_\perp = 0$ are then computed via diagonalisation of the 6×6 companion matrix

$$C(E) = \begin{pmatrix} 0 & I \\ -(H^{(2)})^{-1}(H^{(0)} - EI) & -(H^{(2)})^{-1}H^{(1)} \end{pmatrix}, \tag{4.4}$$

where I is the 3×3 identity matrix. The $k_\perp$-dependent complex bands are then obtained via [159, 166]

$$k_{\parallel,n}(E, k_\perp) = \sqrt{k^2_{\parallel,n}(E, 0) - k^2_\perp}\,. \tag{4.5}$$

Our continuum BTBT model consists of using the complex band structure admitted by Eq. (4.3) to compute the BTBT transmission coefficient T and generation rate G. To calculate the BTBT transmission coefficient T we will use the WKB approximation, that assumes we have a slowly varying potential barrier, T is computed as [159, 166, 167]

$$T(\mathbf{k}_\perp) = \frac{\pi^2}{9} \exp\left(-\frac{2}{eF} \int_{E_{\mathrm{VB}}(\mathbf{k}_\perp)}^{E_{\mathrm{CB}}(\mathbf{k}_\perp)} |\mathrm{Im}\{k_\parallel(E, \mathbf{k}_\perp)\}|\, \mathrm{d}E \right), \tag{4.6}$$

where $E_{\mathrm{CB}}(\mathbf{k}_\perp)$ and $E_{\mathrm{VB}}(\mathbf{k}_\perp)$ describe the (real) CB and LH VB dispersion, $k_\parallel(E, \mathbf{k}_\perp)$ is the complex band linking the CB and VB at perpendicular wave vector $\mathbf{k}_\perp$, and F is the strength of the applied electric field along the tunneling direction. The direct BTBT generation rate G is computed via integration of T as [159, 166]

$$G = \frac{eF}{\pi\hbar} \int \frac{\mathrm{d}\mathbf{k}_\perp}{(2\pi)^2}\, T(\mathbf{k}_\perp)\,. \tag{4.7}$$

The complex band structure admitted by Eq. (4.3) is spherical, allowing to set $\mathrm{d}\mathbf{k}_\perp = 2\pi k_\perp \mathrm{d}k_\perp$ in Eq. (4.7), where $k_\perp = |\mathbf{k}_\perp|$, so that numerical calculation of G requires numerical quadrature in only one dimension.

Our benchmark calculations for InAs in Ref. [166] verified that, when band nonparabolicity is minimal in the ranges of E and $\mathbf{k}_\perp$ that contribute to BTBT, the results obtained via numerical evaluation of Eqs. (4.6) and (4.7) closely reproduce the analytical $T(k_\perp)$ and $G(F)$ of the Kane model. [168, 169] Eqs. (4.6) and (4.7) then provide a generalisation beyond the simplifying approximations employed in the Kane model, allowing here to quantify the impact of Sn-induced Γ_{7c}-L_{6c} hybridisation on G.

4.4 Complex band structure: Sn-induced band hybridisation and complex band anti-crossing

We begin by considering the complex band structure of, and direct BTBT in, idealised ordered $\mathrm{Ge}_{1-x}\mathrm{Sn}_x$ alloy supercells. Our previous DFT and TB calculations have demonstrated that the evolution of the electronic structure close in energy to the CB and VB edges in $\mathrm{Ge}_{1-x}\mathrm{Sn}_x$ is driven primarily by Sn-induced hybridisation of Ge host matrix CB states, with this hybridisation taking a simple form in an ordered alloy[40, 68, 69]. Specifically, in ordered $\mathrm{Ge}_{1-x}\mathrm{Sn}_x$, Sn atoms perturb the crystal Hamiltonian such that hybridisation is introduced between orbital components of Ge states having the same symmetry about the Sn site[68, 170]. The strength of this hybridisation

depends inversely on the difference in energy between the hybridising states, such that Sn-induced hybridisation in the composition range $x \lesssim 20\%$ for which $Ge_{1-x}Sn_x$ is a semiconductor occurs primarily between two Ge CB states due to their proximity in energy: the Γ_{7c} zone-centre CB edge state, and a linear combination of L-point L_{6c} CB minimum states having s-like orbital symmetry on the Sn atom[68, 69]. The evolution of the alloy CB structure with increasing x is then dominated by this hybridisation, which leads the alloy CB edge to acquire increasing Ge Γ_{7c} character, such that the alloy CB edge evolves continuously from having entirely indirect (Ge L_{6c}) character in Ge to having predominantly direct (Ge Γ_{7c}) character for $x \gtrsim 6\%$[69].

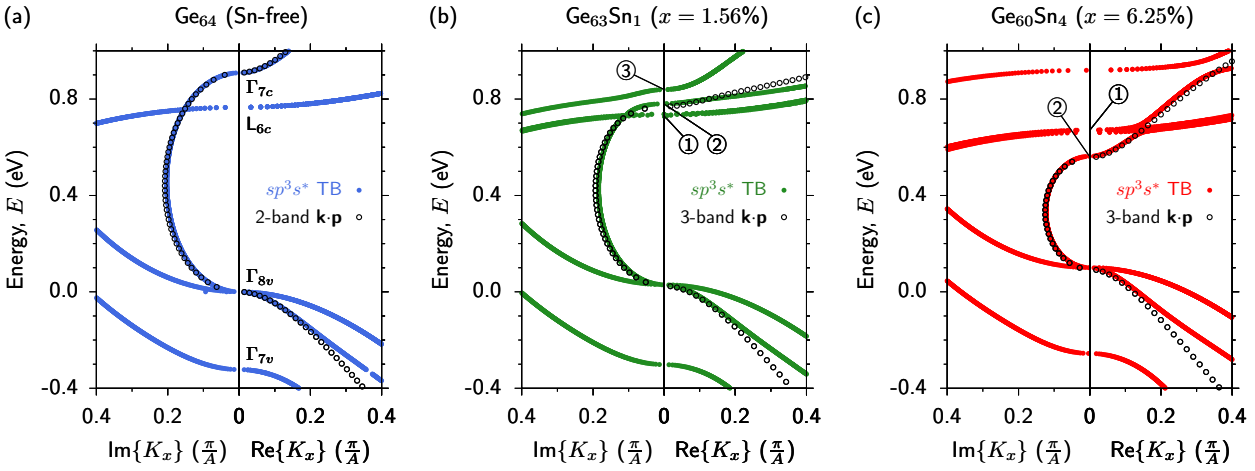

FIGURE 4.2: Complex band structure of relaxed (a) Ge_{64} (Sn-free; closed blue circles), (b) ordered $Ge_{63}Sn_1$ ($x = 1.56\%$; closed green circles), and (c) ordered $Ge_{60}Sn_4$ ($x = 6.25\%$; closed red circles) supercells, calculated using the atomistic TB method. In each case the left- (right-) hand panel shows the calculated complex (real) band dispersion. Open black circles in (a) show the Ge complex band structure calculated using a 2-band (Kane) $\mathbf{k}\cdot\mathbf{p}$ Hamiltonian, and in (b) and (c) show the $Ge_{1-x}Sn_x$ complex band structure calculated using the 3-band $\mathbf{k}\cdot\mathbf{p}$ Hamiltonian of Eq. (4.3). The zero of energy lies at the Ge Γ_{8v} VB maximum.

We investigate the impact of this alloy band mixing by considering two ordered, 64-atom ($2\times2\times2$ simple cubic) $Ge_{1-x}Sn_x$ alloy supercells: (i) a $Ge_{63}Sn_1$ ($x = 1.56\%$) supercell containing a single substitutional Sn atom, and (ii) a $Ge_{60}Sn_4$ ($x = 6.25\%$) supercell containing four substitutional Sn atoms. The Sn atoms in the $Ge_{60}Sn_4$ supercell are substituted on a face-centred cubic ordered array of lattice sites, with the supercell alloy microstructure then being equivalent to that of the ordered 16-atom ($2\times2\times2$ face-centred cubic) $Ge_{15}Sn_1$ supercell investigated in Refs. [68] and [69]. The use of simple cubic lattice vectors for the ordered $Ge_{60}Sn_4$ supercell allows for straightforward application of the approach of Ref. [114] to compute the [100] complex band structure (section 4.3.1). The choice of $2\times2\times2$ simple cubic supercells for the ordered alloy calculations ensures that the L-point eigenstates of the Ge host matrix back-fold to the supercell zone centre $\mathbf{K} = 0$, allowing Sn-induced hybridisation between Ge Γ- and L-point states[37, 68, 170].

Figure 4.2 shows the TB-calculated complex band structures of relaxed (a) Ge_{64} (closed blue circles), (b) $Ge_{63}Sn_1$ (closed green circles), and (c) $Ge_{60}Sn_4$ (closed red circles) supercells. In each case, the left- (right-) hand panel shows the imaginary (real) part of the component K_x of the complex supercell wave vector $\mathbf{K}$ along [100], while the zero of energy lies at the Ge VB

maximum. The complex band structures shown in Figs. 4.2(a), 4.2(b) and 4.2(c) were calculated at wave vector $\mathbf{K}_\perp = (K_y, K_z) = (0, 0)$ in the plane perpendicular to the [100] tunneling direction. Beginning with the real band dispersion in Fig. 4.2(a), we note the indirect-gap band structure of the Ge_{64} host matrix supercell. The lowest energy $\mathbf{K} = 0$ CB state in Ge_{64} is the back-folded L_{6c} CB minimum at energy 0.765 eV, while the Γ_{7c} state at energy 0.909 eV is the second-lowest energy $\mathbf{K} = 0$ supercell CB state. The Ge_{64} complex band structure admits an evanescent Bloch band linking the Γ_{8v} and Γ_{7c} zone-centre VB and CB edge states, providing the pathway for direct BTBT across the direct Γ_{7c}-Γ_{8v} band gap of pure Ge – i.e. between the zone-centre LH VB edge and CB edge states. The complex band originating from the back-folded L_{6c} state in Ge_{64} couples to states lying deep within the VB (out of scale in Fig. 4.2), so that there is no pathway for direct BTBT between the zone-centre Γ_{8v} VB maximum and the L-point L_{6c} CB minimum. We note that the evanescent Bloch band originating from the L_{6c} CB minimum passes through that linking the Γ_{8v} and Γ_{7c} VB and CB edge states without interaction at $K_y = K_z = 0$.

Considering now the real band dispersion of the ordered $Ge_{63}Sn_1$ supercell in the right-hand panel of Fig. 4.2(b), we begin by noting the Sn-induced perturbation of the $\mathbf{K} = 0$ CB states. In Ge_{64} the back-folded L_{6c} CB minimum states are eightfold (fourfold and spin) degenerate. In ordered $Ge_{63}Sn_1$ Sn-induced hybridisation partially lifts this degeneracy, giving rise to a CB minimum that is sixfold (threefold and spin) degenerate, with an additional twofold (spin) degenerate state lying slightly higher in energy. The lowest energy CB states at $\mathbf{K} = 0$ in $Ge_{63}Sn_1$ are (cf. Fig. 4.2(b)):

① a set of sixfold degenerate alloy CB minimum states comprised almost entirely of linear combinations of Ge L_{6c} states having *p*-like orbital character on the Sn atom,

② a twofold degenerate state lying 20 meV above the alloy CB minimum in energy, formed primarily of a linear combination $|L_{6c}(A_1)\rangle$ of Ge L_{6c} states having *s*-like orbital character on the Sn atom and possessing an admixture of the Ge Γ_{7c} state, and

③ a twofold degenerate state lying 125 meV above the alloy CB minimum in energy, formed primarily of the Ge Γ_{7c} state and possessing an admixture of the Ge $|L_{6c}(A_1)\rangle$ state. [68]

Here, ② and ③ are the product of Sn-induced Γ_{7c}-L_{6c} hybridisation (section 4.3.2). Similarly, ① is the product of hybridisation between linear combinations of Ge L_{6c} states having *p*-like orbital character on the Sn atom and linear combinations of other $\mathbf{K} = 0$ Ge_{64} states having equal symmetry. This hybridisation is significantly weaker than that observed between Γ_{7c} and L_{6c} states due to the larger separation in energy between the Ge L_{6c} states and the other back-folded $\mathbf{K} = 0$ states in Ge_{64} that possess *p*-like orbital components and lie closest in energy (e.g., linear combinations of X-point Ge X_{5c} CB edge states). We note that the downward shift in CB edge energy driven by Sn-induced hybridisation is accompanied by an upward shift in VB edge energy – relative to the band edge energies of Ge in both cases – but that there are no notable hybridisation effects close in energy to the VB edge, with the $Ge_{63}Sn_1$ VB maximum retaining almost entirely Ge Γ_{8v} character. [68] The $\mathbf{K} = 0$ band gap in $Ge_{63}Sn_1$ is calculated to be reduced by 40 meV relative to the fundamental L_{6c}-Γ_{8v} band gap of Ge.

Contrary to the minor changes in the real band dispersion of $Ge_{63}Sn_1$ vs. Ge_{64}, we note a radical change in the nature of the complex band dispersion in the left-hand panel of Fig. 4.2(b). Specifically, we find that Sn-induced Γ_{7c}-L_{6c} hybridisation strongly modifies the evanescent Bloch band emerging from the VB maximum: this band now links the VB maximum to state ② described above, as a consequence of the acquisition by the latter of an admixture of Γ_{7c} character via Sn-induced hybridisation. In Ge_{64} the evanescent Bloch band linking the Γ_{8v} and Γ_{7c} states passed through the evanescent bands linking L_{6c} CB states to deep VB states without interaction. However, in $Ge_{63}Sn_1$ the presence of Γ_{7c}-L_{6c} hybridisation results in anticrossing between the evanescent Bloch bands originating from the hybridised alloy CB states ② and ③. This results in an evanescent Bloch band linking the alloy VB edge to the primarily Ge L_{6c}-like state ②, rather than the primarily Ge Γ_{7c}-like state (iii). We also note that the evanescent Bloch bands emerging from states ① remain similar to those associated with the L_{6c} CB minimum in Ge_{64}: linking only to states lying deep within the VB and hence providing no pathway for direct BTBT from the alloy VB maximum.

The expected implications of this strongly modified complex band structure for direct BTBT can be readily forecast based on the WKB approximation. In the WKB approximation the BTBT transmission coefficient is an exponential function of the area bounded by the evanescent Bloch band linking the VB and CB – in the plane defined by a carrier's energy and the imaginary part of the component of its wave vector along the tunneling direction – being enhanced as this area is decreased (cf. Eq. (4.6)). The modified complex band structure of $Ge_{63}Sn_1$ strongly decreases this area. At $\mathbf{K}_\perp = 0$ in Ge_{64} this evanescent band spans an energy range of width 0.909 eV (the direct band gap) with maximum imaginary wave vector $|\mathrm{Im}\{K_x\}| = 0.18 \times \frac{\pi}{A}$ (where $A = 2a$ is the relaxed $2 \times 2 \times 2$ simple cubic supercell lattice parameter). The equivalent evanescent band in $Ge_{63}Sn_1$ spans an energy range of width 0.71 eV with maximum imaginary wave vector $|\mathrm{Im}\{K_x\}| = 0.17 \times \frac{\pi}{A}$. A significant enhancement of the direct BTBT generation rate G is then expected in response to Sn incorporation in Ge. We emphasise that this behaviour is markedly different to that assumed in previous VCA-based analyses: our atomistic $Ge_{63}Sn_1$ supercell calculation reveals that Sn-induced hybridisation strongly modifies the complex band structure, opening a direct-gap-like pathway for BTBT at low Sn composition $x = 1.56\%$ for which the alloy is assumed to be purely indirect-gap in the VCA. The corresponding evanescent Bloch band in the VCA links the alloy VB edge to the equivalent of the CB state ③ from our atomistic calculation – which, in the VCA, acquires no admixture of Ge L_{6c} character – so that the VCA will thus fail to capture even qualitatively the nature of the $Ge_{1-x}Sn_x$ complex band structure close in energy to the band gap. By neglecting atomistic effects the VCA then overestimates the band gap relevant to direct BTBT in $Ge_{1-x}Sn_x$ at low x, and is therefore expected to underestimate the associated direct BTBT generation rate G.

Turning our attention to the ordered $Ge_{60}Sn_4$ ($x = 6.25\%$) supercell of Fig. 4.2(c), we note the role played by Sn composition-dependent alloy band mixing on the evolution of the CB structure. Here, hybridisation between Ge Γ_{7c} and L_{6c} states is enhanced with increasing x (cf. Eq. (4.3)),

such that states ② and ③ identified for $Ge_{63}Sn_1$ ($x = 1.56\%$) repel one another in energy and the lower (higher) energy state acquires increased Ge Γ_{7c} (Ge $|L_{6c}(A_1)\rangle$) character.

Sn incorporation has a stronger effect on the band structure for the $Ge_{60}Sn_4$ supercell in Fig.4.2(c) which has a higher composition of $x = 6.25\%$, where there is greater hybridisation of the CB edge states leading to greater transfer of direct gap character to the CB edge state derived from the Ge CB s-like L_{6c} state. As a result, the CB minimum state lying at 0.553 eV has a complex band linking to the VB maximum, with both the area of the complex band and band gap greatly reduced compared to Ge. The maximum wave vector has reduced to 0.134 $\frac{\pi}{A}$, and we therefore expect this greatly reduced area of the complex band to strongly enhance the BTBT generation rate. As a result we expect ordered $Ge_{1-x}Sn_x$ SCs to have greatly increased generation compared to Ge for compositions below the conventional indirect to direct gap cross-over.

To explicitly verify that the origin of the strongly modified complex band structures obtained from our ordered alloy supercell atomistic TB calculations are a direct consequence of Sn-induced Γ_{7c}-L_{6c} hybridisation, we employ the 3-band **k·p** Hamiltonian of section 4.3.2. We begin by computing the complex band structure of Ge using the 2-band (Kane) Hamiltonian for the CB and LH VB edge states obtained by setting $x = 0$ in, and omitting the first row and column of, Eq. (4.3). The result of this calculation at $k_\perp = 0$ is shown in Fig. 4.2(a) using closed black circles, where we note that this simple continuum model accurately captures the dispersion of the evanescent Bloch band linking the zone-centre Γ_{7c} CB edge and Γ_{8v} LH VB maximum states. We note that this simple **k·p** model only describes the real CB and LH dispersion accurately at wave vectors close to the zone centre. However, as we will demonstrate below, the fact that only states lying energetically in the immediate vicinity of the Γ-point CB and VB edges contribute to direct BTBT [159, 166, 169] allows to use this simplified band structure to quantitatively reproduce the field-dependent direct BTBT generation rate G vs. F obtained from full atomistic NEGF calculations.

Starting with this 2-band **k·p** Hamiltonian for Ge, the 3-band model of Eq. (4.3) is obtained via inclusion of the Ge $|L_{6c}(A_1)\rangle$ state described above, and accounts for (i) Sn composition-dependent shifts to the Γ- and L-point CB edge energies, as well as (ii) Sn-induced hybridisation between the $|\Gamma_{7c}\rangle$ and $|L_{6c}(A_1)\rangle$ Ge host matrix CB states. The complex band structures calculated at $k_\perp = 0$ using Eq. (4.3) for $x = 1.56\%$ ($Ge_{63}Sn_1$) and $x = 6.25\%$ ($Ge_{60}Sn_4$) are respectively shown in Figs. 4.2(b) and 4.2(c) using closed black circles. In both cases we find that the 3-band **k·p** model describes accurately the dispersion of the evanescent Bloch band linking the CB and VB edges. Here, we note a caveat regarding the interpretation of the complex band structure admitted by Eq. (4.3). This simple model captures accurately the energy and hybridised character of the lower-energy ordered alloy CB state formed via Sn-induced hybridisation of Ge Γ_{7c} and L_{6c} states. However, the higher energy CB does not in general represent a real material band, but rather a weighted average of the range of supercell CB states with which $|L_{6c}(A_1)\rangle$ and $|\Gamma_{7c}\rangle$ can (by symmetry) hybridise. This is similar to the interpretation of closely related band-anticrossing model Hamiltonians for highly-mismatched dilute III-V-N and III-V-Bi alloys[132, 171]. In the context of the present analysis, we are interested only in direct BTBT and hence only in the part of the band dispersion in the immediate energetic vicinity of the CB and VB edges, so that this

higher energy CB does not enter into, or impact the results of, our continuum BTBT calculations (cf. Eqs. (4.6) and (4.7)).

Overall, this simple 3-band $\mathbf{k}\cdot\mathbf{p}$ model explicitly verifies that the emergence of a direct-gap-like pathway for BTBT in ordered $Ge_{1-x}Sn_x$ is a consequence of Sn-induced hybridisation – i.e. it arises due to $Ge_{1-x}Sn_x$ alloy CB edge states being formed of an admixture of the Γ- and L-point CB edge states of Ge. We emphasise that this band hybridisation, which is an explicitly atomistic effect, is quantitatively described by the simple model Hamiltonian of Eq. (4.3). This demonstrates that computationally efficient continuum models can be constructed to capture the impact of atomistic effects on the complex band structure, but that the derivation of such models must rely on the detailed insights afforded by, and material parameters extracted from, atomistic electronic structure calculations.

4.5 Direct BTBT: impact of Sn-induced band hybridisation and short-range alloy disorder

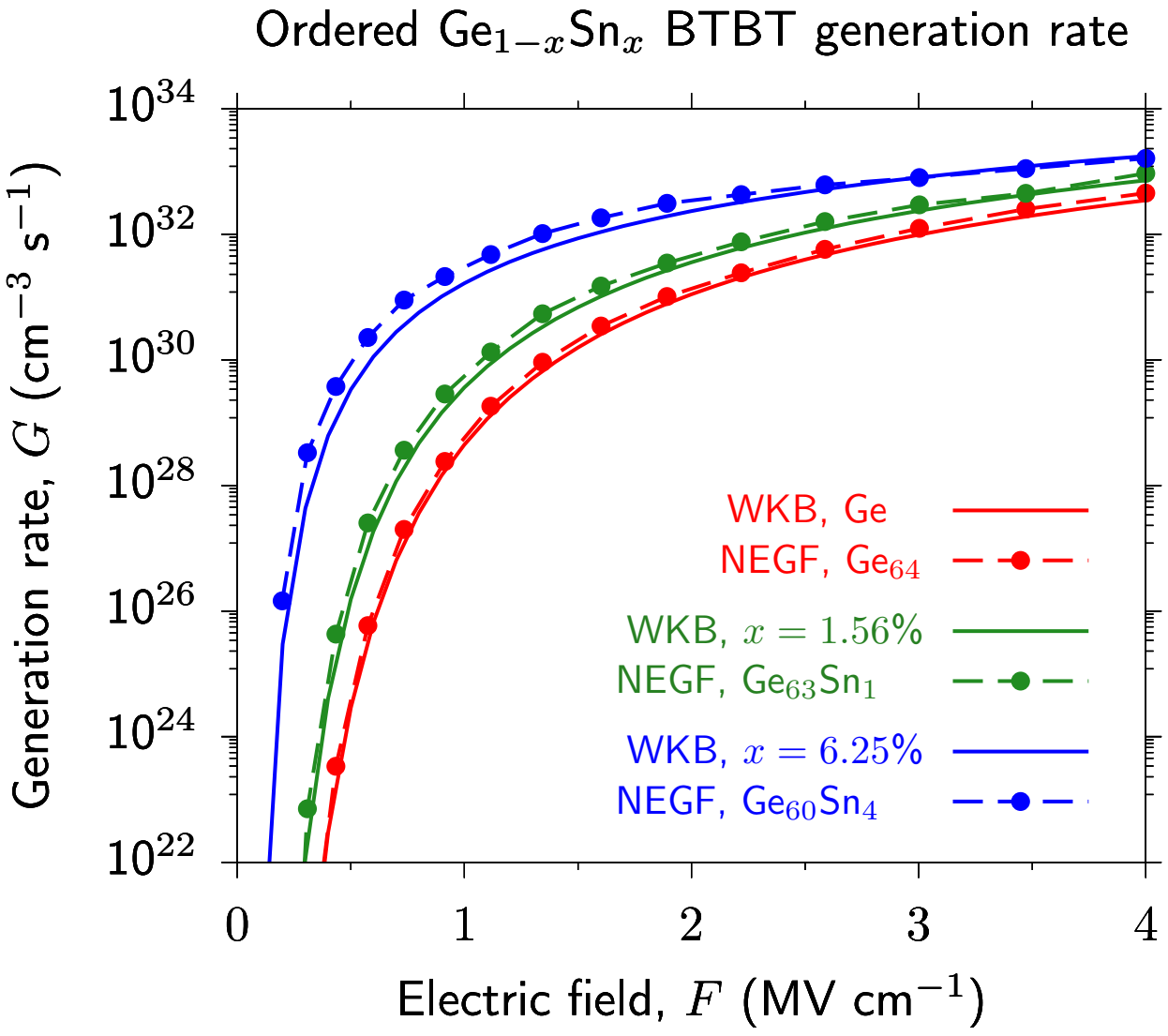

FIGURE 4.3: Generation rates calculated using NEGF model (dash-dot lines) for a Ge supercell and two ordered $Ge_{1-x}Snx$ supercells with compositions $x = 1.5625\%$ and 6.25%. Solid lines indicate generation rates calculated using the WKB approximation with the band structure calculated using the 3-band $\mathbf{k}\cdot\mathbf{p}$ Hamiltonian of Eq. (4.3) for the same two $Ge_{1-x}Snx$ compositions and the 2-band Hamiltonian for Ge

Having described in detail the impact of Sn incorporation on the complex band structure in ordered $Ge_{1-x}Sn_x$ alloys, we now turn our attention to the resultant consequences for direct BTBT. We firstly compare the calculated G vs. F obtained via our atomistic (TB + NEGF) and continuum ($\mathbf{k}\cdot\mathbf{p}$ + WKB) models for the $x = 1.56$ and 6.25% supercells of section 4.4. Following this, we demonstrate the impact of short-range disorder by considering large, disordered supercells at these same Sn compositions and comparing the results of our small, ordered and large, disordered supercell calculations. We see that the band mixing effects are reduced but not eliminated with disorder, so that a direct tunneling path still remains from states close to or at the CB edge.

For each composition we started with the ordered $2 \times 2 \times 2$ SC supercells used in the complex band structure calculations which was then repeated along the transport direction creating a supercell with periodic structure along the transport direction with a length of 30nm. This structure has periodic boundary conditions in directions perpendicular to the transport direction and the ends are connected to semi-infinite reservoirs enabling injection of charge carriers[72]. A uniform electric field was applied along the transport direction of the structure and the current was calculated using the NEGF formalism. The electric fields chosen were in the range 0.1 - 4 MV cm^{-1}, with the values F chosen so there are more points near a field of 1 MV cm^{-1}. The current density calculated by the OMEN solver was used with Eq. (4.2) to get the generation rate of the supercell. The evolution of the generation rates with electric field F for Ge and $Ge_{1-x}Sn_x$ with x = 1.5625% and 6.25% are shown in Fig.4.3 as dashed lines. Here we see a marked increase in the generation rate of both $Ge_{1-x}Sn_x$ supercells in comparison to Ge, which is in keeping with the reduced area of the complex band linking the VB and CB edges states. The largest increase in generation rate is for the x = 6.25% $Ge_{60}Sn_4$ supercells with an increase of more than four orders of magnitude for F $<$ 1 MV cm^{-1}. For high fields there is an increase of less than an order of magnitude compared to Ge as the generation rate saturates at high F and the effect of the reduced area of the complex band has less impact. For the lower composition 1.5625% Sn supercell there is an increase of 1 order of magnitude for F $<$ 1 MV cm^{-1}. While not as strong as the higher composition 6.25% case it does point to an immediate strong impact when Sn is incorporated. The increase in the generation rate thus suggests band mixing can have a large effect on BTBT in $Ge_{1-x}Sn_x$: the increase for $x = 1.56\%$ is found where a conventional VCA approach would not demonstrate a large increase in the generation rate.

To further support the evidence of band mixing effects on BTBT in $Ge_{1-x}Sn_x$ we use the complex bands calculated using the 3-band $\mathbf{k}\cdot\mathbf{p}$ Hamiltonian to calculate the transmission probability using the WKB approximation. The generation rate was calculated using Eq.(4.7), from which the generation rate results for Ge and $Ge_{1-x}Sn_x$ with x = 1.5625% and 6.25% are plotted in Fig.4.3 as solid lines. There is excellent agreement between the NEGF and WKB generation rates for the three supercells, showing that a simple model using only three VB and CB edge states with a Sn-induced Γ-L mixing term is sufficient to accurately describe the BTBT behaviour of ordered $Ge_{1-x}Sn_x$ alloys. Due to band mixing there is enhanced BTBT for $Ge_{1-x}Sn_x$ alloys for Sn compositions below the conventional indirect to direct gap transition. Overall these results further emphasise band mixing having a large impact on BTBT in $Ge_{1-x}Sn_x$ alloys. However, these calculations have not included the local alloy disorder that would be present in real devices which can be expected to reduce some of the impact of band mixing.

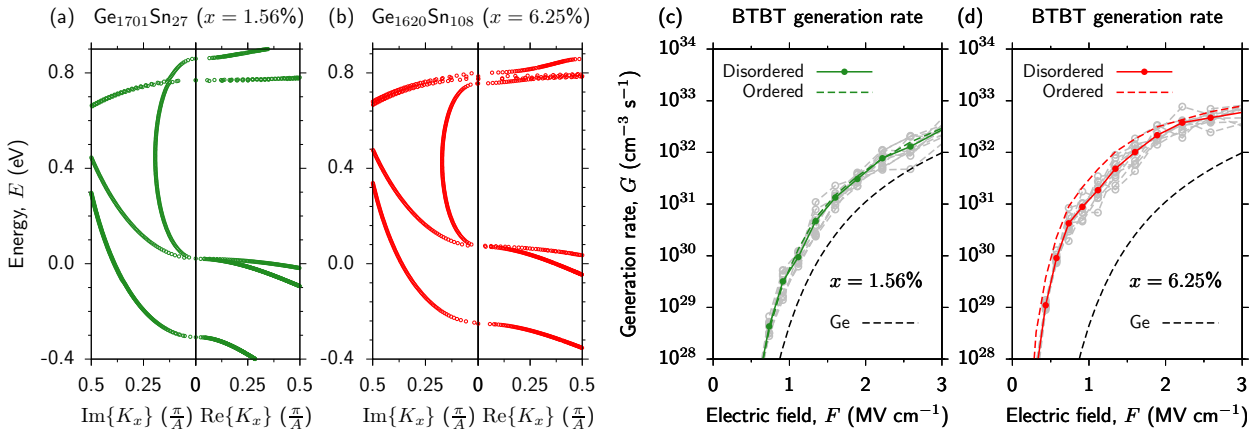

FIGURE 4.4: TB-calculated complex band structure of disordered, 1728-atom (a) $Ge_{1701}Sn_{27}$ ($x = 1.56\%$; open green circles), and (b) $Ge_{1620}Sn_{108}$ ($x = 6.25\%$; open red circles) supercells. In each case the left- (right-) hand panel shows the calculated complex (real) band dispersion. (c) and (d) respectively show the NEGF-calculated BTBT generation rate G vs. applied electric field F for alloy supercells having Sn compositions $x = 1.56\%$ and $x = 6.25\%$. Open grey circles show G vs. F calculated for each of the 10 distinct, disordered supercells considered at each Sn composition. Closed green circles in (c), and closed red circles in (d), show the corresponding configuration-averaged value of G at each applied electric field. The solid green line in (c) and solid red line in (d) respectively show the calculated G vs. F for ordered $Ge_{63}Sn_1$ ($x = 1.56\%$) and $Ge_{60}Sn_4$ ($x = 6.25\%$) supercells (cf. Fig. 4.3). The dashed black line in (c) and (d) shows the calculated G vs. F for Sn-free Ge (cf. Fig. 4.3).

4.6 Evolution of band-to-band tunneling current in disordered $Ge_{1-x}Sn_x$ alloys

Having described how incorporation of Sn in ordered $Ge_{1-x}Sn_x$ alloys drives an increase in the BTBT generation rate due to hybridisation of the CB edge states, we now turn to more realistic structure with disordered $Ge_{1-x}Sn_x$ alloys. Based on the results for the ordered structures, we can expect an increased tunnelling rate at low Sn compositions compared to that predicted by previous VCA calculations, due firstly to the reduced energy gap in atomistic compared to VCA calculations, and secondly due to the continued impact of band mixing and alloy scattering effects, even at low Sn compositions, which should allow direct tunnelling from the lowest band, even when the band gap is still considered to be indirect. The difference in tunnelling rate between atomistic and continuum VCA-type calculations should then reduce at higher compositions, where the alloy has a direct energy gap.

As with ordered supercells, we begin by looking at the evolution of the complex band structure with composition. Our choice of $Ge_{1-x}Sn_x$ supercell is guided by the need to be sufficiently large so that for low Sn compositions there are enough Sn atoms to allow alloy disorder effects to be present. We compute the complex band structure for a 1728 atom $6 \times 6 \times 6$ SC supercell. The $6 \times 6 \times 6$ supercell retains the large number of atoms required for bulk transport calculations. The disordered complex band structure calculations were carried out at the same compositions as the ordered supercells, to enable direct comparison with the results in Fig.4.2. A starting Ge 1728 atom supercell was created and for both compositions Sn atoms were randomly incorporated

in place of Ge atoms, after which the supercell was relaxed using the VFF model. The resulting complex band structures of the disordered $Ge_{1-x}Sn_x$ supercells are shown in Fig.4.4(a,b). For both compositions, disorder reduces but does not eliminate the anti crossing of the complex bands in comparison to the ordered complex band structures of Fig.4.2. For the x = 1.5625% supercell in Fig.4.4(a) there is a weak anti crossing of the complex bands originating from the CB edge states derived from the Ge Γ_{7c} and s-like L_{6c} CB edge states, leading to a reduction in the area of the complex band linking the CB and VB edges in comparison to Ge (Fig.4.2(a)). As a result, there is a shorter path for tunneling between the band edges. The reduction in area of the complex band between the VB and CB edges is not much less than that of the corresponding ordered x = 1.56% supercell in Fig.4.2(b). Consequently the disordered BTBT generation rate can be expected to be comparable to that of the ordered supercell, with disorder having only a limited impact at this low composition. The x = 6.25% disordered supercell has a larger energy gap (0.68 eV) compared to the ordered 6.25% structure (0.533 eV). The complex band linking the CB and VB edges covers an energy range of 0.68 eV, compared to an energy range of 0.553 eV in the ordered case. This will lead to a reduction in BTBT in the disordered case compared to that found in the ordered supercell calculation. A direct tunnelling path can be observed from the lowest conduction band to the highest valence band in both Fig. 4.4(a) (x = 1.56%) and in Fig. 4.4(b) (x = 6.25%). Hence, the area enclosed by the disordered complex band is still reduced compared to that in Ge, which can be expected to lead to an increased tunnelling rate at low composition, compared both to Ge and to the VCA alloy.

The generation rates for ordered and disordered structures with $x = 1.56\%$ and 6.25% are shown in Figs. 4.4(c-d). For both compositions there is a marked increase in the generation rates compared to Ge. There is minimal difference between the ordered and disordered generation rates for $x = 1.56\%$, as expected from the similar energy gaps and complex band structures in the two cases. For $x = 6.25\%$ there is a reduction in the disordered generation rate compared to the ordered case due to the smaller energy gap in the ordered case. However the rate is still greatly enhanced compared to Ge, reflecting the large reduction in the lowest energy gap compared to the direct gap value in Ge. Looking at the open grey circles in Figs. 4.4(c-d) we see there is a spread of up to an order of magnitude in the values of the calculated BTBT generation rate for each of the 10 distinct disordered supercells. A spread of greater than an order of magnitude in BTBT currents for random alloys have been reported elsewhere in the literature for group-IV[172] and III-V alloys[74].

Fig. 4.5(a) shows the calculated BTBT generation rate for ordered WKB calculations, as the Sn composition is increased from 0% to 10% in steps of 2%, with the trends colored purple to red corresponding to compositions x=1% to 10%. Fig. 4.5(b) shows a similar plot for the disordered NEGF calculations. For all compositions, there is an increase in the generation rate compared to Ge, with the increase being most pronounced at lower fields ($F <\sim 1$ MV cm^{-1}). The results are qualitatively similar for the two cases. The change in generation rate in both Fig. 4.5(a) and (b) is most pronounced between the curves for x = 0% and x = 2%, reflecting that band mixing permits direct tunnelling from the lowest conduction band in $Ge_{0.98}Sn_{0.02}$, something which is not

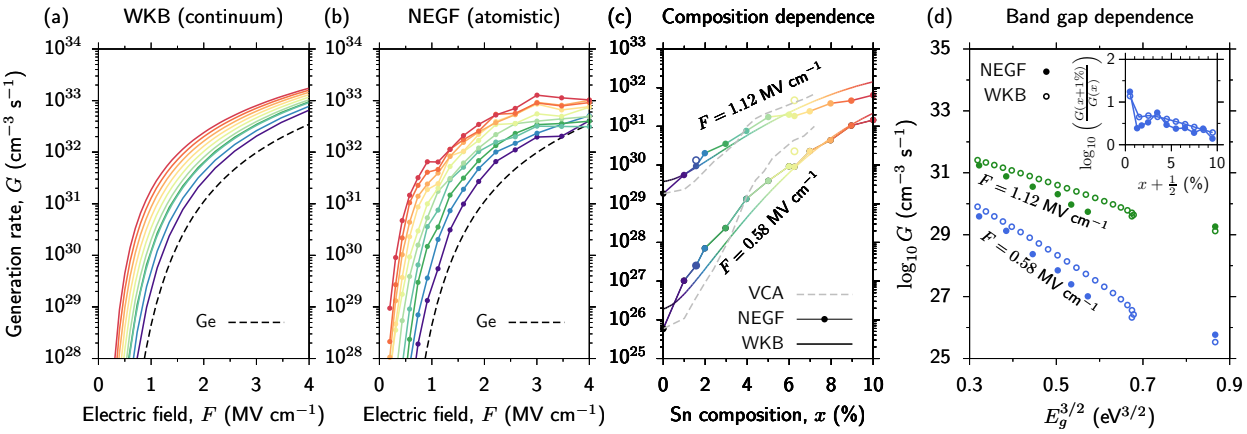

FIGURE 4.5: BTBT generation rate G vs. applied electric field F calculated using the (a) continuum WKB, and (b) atomistic NEGF models. In (a) and (b) G vs. F is shown for Ge (dashed black line), and for $Ge_{1-x}Sn_x$ having Sn compositions $x = 1\%$ (solid purple line and closed circles) to 10% (solid red line and closed circles) in steps of 1%. Values of G in (b) are configuration-averaged results for disordered alloy supercells. The dashed red line in (b) shows the calculated G vs. F for an ordered $Ge_{60}Sn_4$ ($x = 6.25\%$) supercell. (c) Evolution of G with Sn composition x at $F = 0.58$ MV cm^{-1} (lower) and 1.12 MV cm^{-1} (upper), calculated using the continuum WKB (solid lines) and atomistic NEGF (closed circles) models. Open black circles denote WKB-calculated values of G for Ge. Open blue and yellow circles respectively show NEGF-calculated values of G for ordered $Ge_{63}Sn_1$ ($x = 1.56\%$) and $Ge_{60}Sn_4$ ($x = 6.25\%$) supercells. Dashed lines indicate generation rates calculated using VCA based model (d) Evolution of $\log_{10} G$ with $E_g^{3/2}$ at $F = 0.58$ MV cm^{-1} (blue) and 1.12 MV cm^{-1} (green), calculated using the continuum WKB (open circles) and atomistic NEGF (closed circles) models. Inset: calculated order of magnitude increase in G with each 1% increase in x at $F = 0.58$ MV cm^{-1}.

permitted in Ge. The generation rates for a given Sn composition are generally higher in the WKB calculations, reflecting that the energy gap calculated from Eq. (4.3) is lower than that found from the TB calculations, with the reduction in gap becoming more pronounced as x increases.

From Figs. 4.5(b) and (c), the enhancement in tunnelling rate is most pronounced at lower fields. This is confirmed in Fig. 4.5(c), which plots the generation rate as a function of Sn composition x at a low field, $F = 0.58$ MV cm^{-1} (lower curves), and at a field of 1.12 MV cm^{-1} (upper curves), where the solid data points show the results of TB NEGF calculations, while the solid lines are calculated using Eq. (4.3) and the WKB approximation. The open circles at $x = 0$ are the generation rates calculated using the WKB method for tunnelling from the Ge conduction band Γ state at 0.95 eV to the top of the Ge conduction band.

It can be observed from both the NEGF and WKB data in Fig. 4.5(c) that there is a marked increase in tunnelling rate at low field ($F = 0.58$ MV cm^{-1}), as soon as any Sn is added to Ge, with the rate of increase in generation rate then decreasing as further Sn is added. This is confirmed by the inset in Fig. 4.5(d), where we plot the order of magnitude increase in the generation rate per 1% increase in Sn composition for both the disordered NEGF and ordered WKB calculations. On the y axis a value of 1 represents an order of magnitude increase in the generation rate compared to the previous Sn composition, while on the x axis compositions are displaced by $\frac{1}{2}\%$ so the y value at $x = 2.5\%$ represents the order of magnitude increase in generation rate for a composition of $x = 3\%$ compared to the previous composition of $x = 2\%$. From this plot we can see the greatest

increase in the generation rates occurs for lower Sn compositions, in particular between $x = 0\%$ and $x = 1\%$.

We see from Fig. 4.5(c) and Fig. 4.5(d) that the impact of Sn incorporation at low compositions becomes less important at higher fields. No marked increase in generation rate is observed between $x = 0\%$ and $x = 1\%$ for a field of $F = 1.12$ MV cm^{-1} in Fig. 4.5(d), while the calculated generation rate for $x = 1\%$ and $x = 2\%$ falls below that for Ge at $F = 4$ MV cm^{-1} in Fig. 4.5(b). This is consistent with our recent analysis of BTBT in highly mismatched semiconductor alloys[166]. At low fields, the generation rate is dominated by tunnelling from states near to the band edge at the centre of the Brillouin zone. Band mixing allows tunnelling from the lower (L-like) conduction band edge state as soon as Sn is added to Ge. However, as the built-in field increases, states with a wider range of in-plane k vectors contribute to the tunnelling rate, and so the overall tunnelling rate then depends more strongly on the character of conduction states at these higher in-plane wavevector values.

All previous studies of BTBT in $Ge_{1-x}Sn_x$ alloys have been undertaken using the virtual crystal approximation (VCA). We test how the results of VCA calculations compare with fully atomistic ones, by using our tight-binding model to parameterise a VCA Hamiltonian for $Ge_{1-x}Sn_x$. We note that the VCA inherently does not include alloy effects such as band mixing and should therefore not have any anti-crossing in the complex band structure. A linear interpolation between the parameters of Ge and Sn was used to create the VCA parameters, where the Ge and Sn parameters came from our existing TB model. No fitting was used to match the band gap evolution with Sn composition of the VCA based model with the alloy calculations. As a result, the VCA model under estimated the band gap reduction and the indirect to direct gap transition in $Ge_{1-x}Sn_x$, with an indirect to direct crossover at $x = 15\%$ as opposed to the conventional $x = 6$-10% Sn in the alloy.

Therefore, a direct comparison between the VCA and alloy calculations at the same compositions was not possible, given that the tunnelling rate depends on energy gap, and the lowest energy gap had a different composition dependence in the two models. Instead the band structures were matched for two criteria (i) the energy splitting of the $Ge_{1-x}Sn_x$ CB edge Γ_{7c} and L_{6c} states and (ii) the band gap. Matching these energies for the VCA and alloy band structures would give us a VCA band structure that replicates the key aspects of the alloy band structure. For a selected alloy composition of 1% Sn the band structure was matched by a VCA composition of 2% Sn giving the same CB edge Γ-L splitting as well as the same band gap. Similarly, an alloy composition of 2% Sn was matched with a VCA composition of 4% Sn. These VCA compositions allow us to study the evolution of BTBT in $Ge_{1-x}Sn_x$ where the only effect of Sn incorporation is band gap reduction. We can then contrast the VCA generation rates with those of alloy calculations where both band mixing and band gap reduction are present. The dashed lines in Fig. 4.5(c) indicate the trend of generation rate with composition for the VCA parameters up to 8% Sn. These confirm an increase in the BTBT generation rate of the alloy calculations over the VCA based calculations. As seen earlier, the alloy effects are greatest for the lower field of F = 0.58 MV cm^{-1} leading to a large increase over the VCA results. This further confirms that band mixing

effects play a key role in $Ge_{1-x}Sn_x$. The inability of the VCA to match the generation rate of alloy calculations demonstrates a need to specifically include alloy effects in modelling of devices based on $Ge_{1-x}Sn_x$. Comparisons for higher VCA compositions are not applicable due to the inability of a VCA to match the Γ-L splitting as composition increases.

Overall, disordered $Ge_{1-x}Sn_x$ calculations demonstrate a strong enhancement of the generation rate compared to Ge, in particular at low fields and compositions, due to band mixing effects. Comparison with VCA calculations explicitly demonstrates that band mixing is the driving force behind the enhanced generation rates.

4.7 Implications for TFET applications

The emergence of a direct band gap in $Ge_{1-x}Sn_x$ alloys for compositions greater than 8% has attracted interest in $Ge_{1-x}Sn_x$ applications as a group-IV TFET[58–64]. This interest has driven further research into the modelling and growth of $Ge_{1-x}Sn_x$ based TFETs[73–85], previous research was based on the assumption of the emergence of the direct band gap at a single critical Sn composition and a corresponding increase in the BTBT generation rate at this composition while below the critical composition the assumed indirect band gap would limit BTBT. To model this behaviour recent analysis have been dependent on on VCA based calculations of the electronic band structure. However these VCA based models are unable to accurately reflect some of the key aspects of the electronic structure evolution of $Ge_{1-x}Sn_x$, particularly alloy effects which therefore represents a serious shortcoming of modelling of $Ge_{1-x}Sn_x$ TFETs using a VCA. Our calculations that specifically include alloy effects demonstrate their key role in evolution of the BTBT in $Ge_{1-x}Sn_x$ alloys. We have shown there is an immediate positive impact upon incorporation of small quantities of Sn that provides an enhanced BTBT generation rate below the conventional indirect to direct gap crossover. Further analysis shows that the enhancement occurs due to hybridisation of the CB edge states leading to the CB minimum acquiring some direct gap like behaviour allowing tunneling from the CB minimum to the VB maximum.

Our ordered alloy calculations demonstrate that on incorporation of a small quantity of Sn $x = 1.56\%$ there is an immediate impact on the complex band structure through hybridisation of the CB edge Γ and L states. As a result, a tunneling path forms between the CB minimum and the VB maximum leading to a corresponding strong increase in the BTBT generation rate of more than an order of magnitude. A VCA fails to capture this increase in the generation rate which we have shown is explicitly due to band mixing effects through parameterisation of a 3-band $\mathbf{k}\cdot\mathbf{p}$ Hamiltonian that can accurately reflects the behaviour of the alloy generation rates based on band mixing effects. Therefore existing modelling of $Ge_{1-x}Sn_x$ TFETs using a VCA will underestimate the BTBT generation rate.

Analysis of local alloy disorder effects demonstrates limited impact for low compositions up to 2% Sn where the benefits of band mixing remain. For higher compositions there is a reduction in the generation rate compared to ideal ordered calculations but crucially the generation rate remains

enhanced. The strong increase in the generation rate for dilute quantities of Sn will be attractive for TFET application due to the limited impact of disorder in dilute structures, where we have shown limited variation between ordered and disordered generation rates up to $\approx 2\%$ Sn.

4.8 Conclusions

In summary, we have presented a detailed theoretical analysis of the nature and evolution of direct (ballistic) BTBT in direct-gap group-IV $Ge_{1-x}Sn_x$ alloys. We established an atomistic calculational framework to analyse BTBT in $Ge_{1-x}Sn_x$, encompassing lattice relaxation based on a fully analytic VFF potential, electronic structure calculations based on a nearest-neighbour TB Hamiltonian, and quantum kinetic BTBT calculations based on a NEGF solution of the coupled Schrödinger-Poisson equations. This framework allows for predictive, large-scale and high-throughput calculations of the electrical properties of bulk-like $Ge_{1-x}Sn_x$ alloys and $Ge_{1-x}Sn_x$-based nanostructures. We applied this approach to move beyond the limitations imposed by the commonly-employed VCA, to (i) elucidate the impact of atomistic electronic structure effects on the $Ge_{1-x}Sn_x$ complex band structure, and (ii) quantify the resultant consequences of alloy-induced band hybridisation and short-range alloy disorder on the BTBT generation rate.

Previous analysis of BTBT in $Ge_{1-x}Sn_x$ has centred on a single approach, comprising electronic structure calculations performed in the VCA, which are used as input to semi-classical BTBT calculations based on the WKB approximation. This approach implicitly neglects atomistic effects, assuming that the indirect- to direct-gap transition occurs abruptly at a single, critical Sn composition x. Our atomistic calculations highlight that this indirect- to direct-gap transition in fact proceeds continuously with increasing x, driven by alloy-induced hybridisation between the L_{6c} CB minimum and Γ_{7c} CB edge states of the Ge host matrix semiconductor. For ordered alloy supercells we demonstrated that this Γ_{7c}-L_{6c} mixing generates complex band-anticrossing that opens up a direct-gap-like pathway for BTBT at Sn compositions at which the alloy is assumed to be indirect-gap in the VCA. This modified complex band structure strongly enhances the direct BTBT generation rate G, which we calculate to exceed that of Ge by approximately four orders of magnitude in an ordered alloy at $x = 6.25\%$. To verify the origin of this behaviour, we derived a model $\mathbf{k}\cdot\mathbf{p}$ Hamiltonian of Sn-induced Γ_{7c}-L_{6c} mixing. This continuum model was shown to quantitatively reproduce the complex band structure obtained from atomistic TB ordered alloy supercell calculations, while using the $\mathbf{k}\cdot\mathbf{p}$ complex band structure in conjunction with the WKB approximation quantitatively reproduced the electric field-dependent G obtained from full atomistic NEGF calculations. This comparison confirms the validity of a semi-classical BTBT analysis, but highlights that such analysis must be underpinned by an appropriate complex band structure model to provide predictive power.

For realistic, disordered $Ge_{1-x}Sn_x$ alloys we quantified the evolution of BTBT via high-throughput, large-supercell NEGF calculations. While a loss of short-range order was found to reduce the impact of Sn-induced band hybridisation, our disordered alloy calculations revealed that the direct-gap-like complex band structure identified in ordered alloy supercell calculations persists. This

results in an immediate onset of enhanced direct BTBT in response to Sn incorporation, such that the associated generation rate G is significantly higher than that predicted by the VCA when the alloy band gap possesses primarily indirect-gap character. Sn composition-dependent calculations demonstrated that the impact of short-range alloy disorder is minimal for $x \lesssim 3\%$, in which Sn composition range the calculated G is close to that obtained from ordered alloy supercell calculations. At higher Sn compositions the disordered-alloy BTBT generation rate is reduced compared to that obtained from ordered alloy supercell calculations, due to a "washing out" of the strength of alloy-induced hybridisation due to a loss of lattice translational symmetry. Nonetheless, the direct BTBT generation rates predicted by our disordered alloy supercell calculations exceed those obtained from VCA-based calculations by approximately an order of magnitude across the $x = 0-10\%$ composition range considered. Explicit comparison between atomistic and VCA-based calculations demonstrated that the omission of band hybridisation effects in the VCA fails to capture the details of the complex band structure, leading to significant underestimation of the BTBT generation rate G. This occurs even when the VCA Hamiltonian is appropriately parameterised to match the experimentally measured band gap bowing, highlighting that the omission of atomistic effects precludes a quantitative understanding of the alloy electrical properties.

Overall, our analysis highlights that previously overlooked atomistic effects play an important role in governing the electrical properties of $Ge_{1-x}Sn_x$ alloys, and that inclusion of these effects in BTBT calculations predicts a significant enhancement in BTBT generation rate compared to initial theoretical predictions. We conclude that the impact of Sn incorporation on the CB structure of $Ge_{1-x}Sn_x$ alloys can then allow for higher on-state currents in $Ge_{1-x}Sn_x$-based TFETs than previously predicted. This, combined with the ability to tune the band gap via Sn composition and nanostructuring, provides broad scope to engineer performance and obtain competitive characteristics from CMOS-compatible TFETs.

Chapter 5

Theoretical analysis of GeSn tunneling field effect transistors

5.1 Overview

In this chapter we present a theoretical analysis of GeSn-based tunneling field effect transistors, with particular interest in the impact of atomistic effects and Sn-induced hybridisation of the CB edge states. As demonstrated in chapter 4 atomistic effects can affect the tunneling characteristics of GeSn alloys. In recent years there has been growing interest in GeSn-based TFETs[63, 73, 74, 78, 79, 173] owing to their direct band gap and compatibility with existing group-IV CMOS fabrication processes. This interest has motivated theoretical work to model the current characteristics of GeSn-based TFETs. Theoretical analyses of GeSn TFETs have to date been based on pseudopotential calculations for the electronic bandstructure and using the semi-classical WKB-Kane transport model[63, 64, 73, 74, 78, 79, 83, 173]. As discussed in chapter 4 this framework is unable to model the atomistic behaviour of GeSn alloys due to the lack of inclusion of alloy effects such as CB hybridisation and local alloy disorder. Here, we investigate the behaviour of GeSn TFET devices using an atomistic approach that specifically include alloy effects to determine their impact on the current characteristics of TFET devices.

We calculate the current characteristics for two device structures, a double gate ultra thin body (DGUTB) TFET and a gate all around (GAA) TFET. We use a semi-empirical theoretical framework consisting of tight-binding-based electronic structure model, valence force field relaxation of alloy supercells and a basis compression algorithm[124] for transport calculations. With this approach we quantify the impact of Sn incorporation on the key TFET current characteristics, the subthreshold swing and the on and off currents.

We begin this chapter in section 5.1 with a review of the physics of the tunneling field effect transistor, describing the differences between the TFETs and the standard MOSFETs and the areas where TFETs are capable of improved performance compared to MOSFETs. In section 5.2 we describe the theoretical workflow we will be using to analyse the current characteristics of GeSn-based TFETs. In this chapter we will be using the basis compression algorithm (BCA) of section 2.3.3, a computationally efficient transport solver when compared to the NEGF method[124].

Here, we also describe the design of the two TFETs we will be examining – the DGUTB TFET and the GAA TFET. Our results will be split into two sections: we first analyse the current characteristics of the DGUTB TFET in section 5.4, where we will look at the evolution of the current characteristics for three device properties; the wire thickness, the channel length and Sn composition. For the GAA TFET we will carry out similar analysis in section 5.5. Finally in section 5.6 we will summarise our findings and conclude.

5.2 Physics of TFET operation

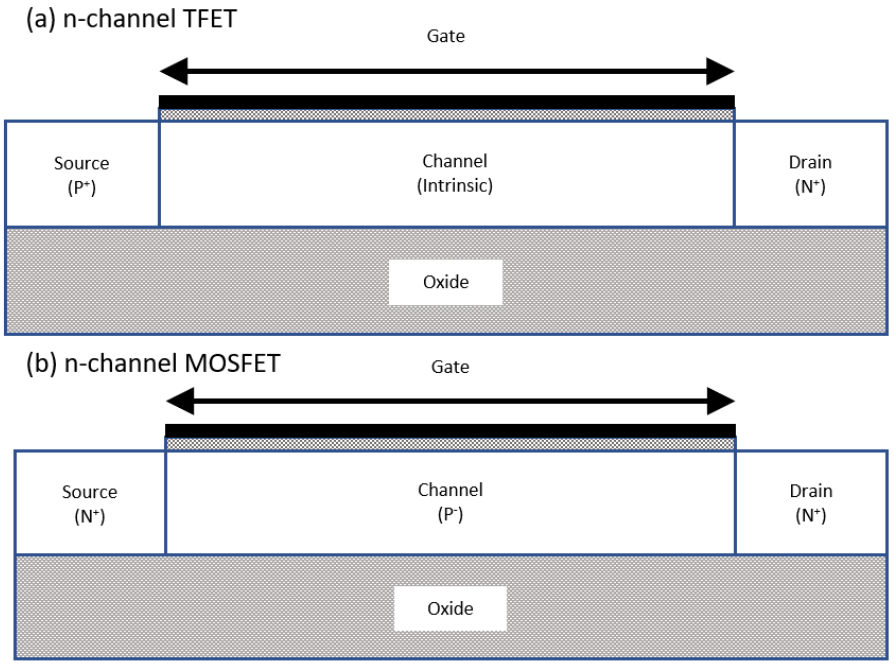

FIGURE 5.1: Schematic diagrams of (a) a MOSFET and (b) a TFET device.

A key characteristic of semiconductor technology is the continuous scaling down of the device dimensions, described by Moore's Law, with the most recent iteration leading to integrated circuits containing on the order of 10^9 transistors, in this case MOSFETs. MOSFET scaling has benefits other than increasing the number of transistors in a chip. The reduced size of the MOSFET reduces the size of the gate leading to a reduced gate capacitance and which improves the switching speed of the device. Additionally, there is a reduction in power consumption due to the reduced voltage required to power the device. With the reduction of MOSFETs to less than 50nm, new issues have appeared such as the increased OFF-state power consumption due to mechanism by which MOSFETs operate, namely thermionic emission from the source to the channel[174] which increase as the potential barrier between the source and channel decreases due to an increase in the gate voltage. The reduced device size leads to two issues, a large off state current due to subthreshold conduction and a related increase in the subthreshold slope (SS). A lower SS is characteristic of a larger ratio between the on current and off current. The subthreshold slope of a MOSFET is given as

$$SS = \frac{d(log_{10}I_{DS})}{dV_G} = 2.3\frac{kT}{q}\left(1 + \frac{C_d}{C_{ox}}\right) \tag{5.1}$$

where C_d is the depletion region capacitance and C_{ox} is the gate oxide capacitance. In Eq. (5.1) there is a necessarily a minimum value for the SS governed by $2.3\frac{kT}{q}$, which at room temperature gives an SS of 60 mV/decade. To get an $\frac{I_{ON}}{I_{OFF}} = 10^5$, we need to apply a gate voltage of 5×60 mV $= 0.3$V according to Eq. (5.1). As a result, it is difficult to scale down the supply voltage and simultaneously have a large $\frac{I_{ON}}{I_{OFF}}$ ratio. Given the inability of MOSFET technology to overcome the issues of large off state current and large SS, a new device has become necessary.

One device proposed in recent years is the tunnelling field-effect transistor (TFET)[175]. The main attraction with TFETs is the possibility of achieving a SS of less than 60 mV/decade. This is due to the difference in device operation between the MOSFET and TFET. While a MOSFET operated via thermionic emission, TFETs use quantum mechanical tunneling to transport charge carriers from the source VB to the channels CB[175]. The potential barrier the charge carriers must tunnel through is wide in the off state, allowing them to posses a low SS. Schematics of MOSFETs and TFETs are shown in Fig. 5.1, which shows the basic structure of an n-channel TFET (Fig. 5.1(b)) consisting of three regions, namely the source, drain and channel. The key difference between TFETs and an n-channel MOSFET (Fig. 5.1(a)), is the source doping in a TFET is p-type, whereas it is n-type in the MOSFET. Therefore TFETs can avail of existing fabrication processes in use for MOSFETs.

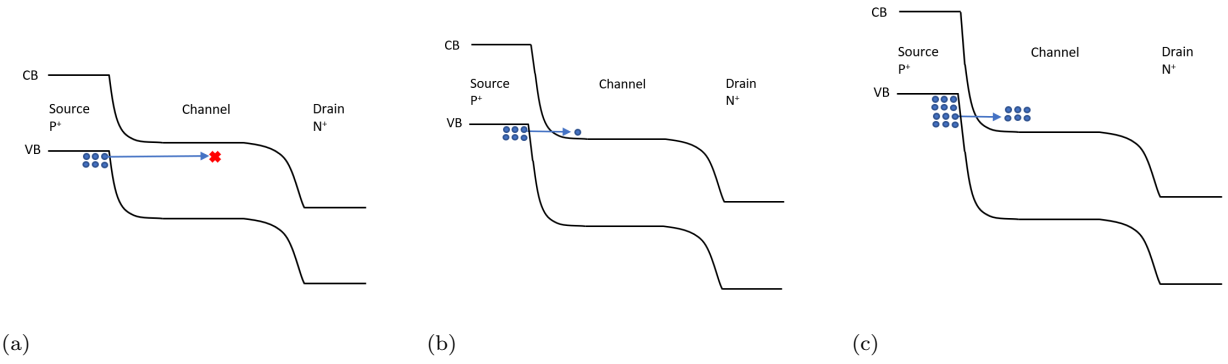

(a) (b) (c)

FIGURE 5.2: Conduction and valence band diagrams of a TFET in the off state (a) and the on state (b, c). The on state is shown for two gate voltages, one at the threshold voltage (b) and one at a higher gate voltage (c).

The IV curves of a TFET provide the key device characteristics, namely I_{on}/I_{off} and the sub-threshold swing. Additional understanding can be gained by plotting the band diagrams of a TFET for different gate voltages V_G, which describe the origin of the current in the I-V curves for a TFET. In Fig. 5.2(a) we plot the band diagrams of a TFET in the off state when $V_G = 0$, any charge carriers present in the CB would drift to the drain forming a current, however, due to the doping of the source (p type) there will be very few free electrons in the CB to maintain a current leading to a small off state current. In order to generate a current, charge carriers must be injected into the CB of the channel. For TFETs the origin of charge carriers will be in the VB

of the source, which will be injected into the channel via tunneling. To instigate tunneling the VB of the source must be energetically aligned with the CB of the channel, this is achieved by increasing the gate voltage. Increasing the V_G caused the CB and VB of the channel to decrease as in Fig. 5.2(b). Once the bands are aligned there will be energy states available for the electrons to tunnel into from the source VB, these electrons can now tunnel through the potential barrier between the source VB and the channel. The V_G at which this alignment occurs is the threshold voltage of the TFET. Increasing V_G further will increase the number of electrons that can tunnel into the channel, additionally as can be seen in Fig. 5.2(c) the tunneling length decreases as V_G increases. As the tunneling probability is related to the exponential of the tunneling length [168], the current will increase further. These two effects lead to a significant increase in the current as V_G increases, thus allowing SS values below the MOSFET limit of 60 mV/decade.

As highlighted previously the key characteristics that make TFETs an attractive replacement for MOSFETs are their low SS and consequently the high I_{on}/I_{off} ratio. The different mechanism of current conduction (band-to-band tunneling) in a TFET is what enables this improved behaviour. However, the change in mechanism will lead to slightly different behaviour of the SS. In a MOSFET, the SS will have an approximately constant slope as in Eq. (5.1). However, TFETs will not have a constant SS. The tunnelling generation rate is an inverse exponential function of the electric field. Leading to the following relationship between the drain current and the electric field E

$$I_{DS} \propto e^{-\frac{1}{E}} \tag{5.2}$$

where E is a function of V_G. Hence the SS of TFET will vary with the gate voltage and will not have a constant value as in the case of a MOSFET. Therefore, for a TFET, two kinds of SS are defined, the point subthreshold swing SS_{point} and the average subthreshold swing SS_{avg}. The point subthreshold swing is calculated at each value of V_G, and is given as

$$SS_{point}(V_{GS}) = \frac{d(log_{10} I_{DS}(V_G))}{dV_G} \tag{5.3}$$

while the average SS is defined over a range of V_G between the off state and the on state

$$SS_{avg} = \frac{V_{th} - V_{off}}{log_{10}(I_{DS}(V_{th}) - I_{DS}(V_{off}))} \tag{5.4}$$

5.3 Theoretical models

5.3.1 Atomistic: VFF potential and TB Hamiltonian

As in chapter 4, our atomistic calculations employ a valence force field (VFF) potential to compute relaxed atomic positions in $Ge_{1-x}Sn_x$ alloy supercells, which are then used to construct the GeSn TFET structures. For the electronic structure we use a sp^3s^* TB Hamiltonian. To compute the drain current I_{DS} in the structure, the relaxed-supercell TB Hamiltonian is then used as input to

a full-band atomistic transport solver based on the basis compression algorithm of section 2.3.3. The VFF lattice relaxations and TB electronic structure calculations are based on those described in [68], where detailed benchmarking was undertaken against density functional theory (DFT) calculations for small alloy supercells.

Our alloy supercell lattice relaxations employ the VFF potential of [157], which is a fully analytic form of the non-polar potential introduced by Martin[103] and has been described in section 2.2.2. Our electronic structure calculations employ a nearest-neighbour sp^3s^* TB Hamiltonian[92], including spin-orbit coupling[98]. The contribution to the alloy supercell TB Hamiltonian at a given lattice site is computed explicitly depending on the local relaxed atomic environment[68]. The on-site orbital energies are computed by averaging over the orbital energies associated with the elemental (Ge or α-Sn) or compound (zinc blende GeSn) materials formed by the on-site atom and each of its four nearest neighbours, including the natural VB offsets between these materials. The nearest-neighbour interatomic interactions are computed by explicitly accounting for changes in relaxed nearest-neighbour bond lengths and angles using, respectively, the generalised form of Harrison's rule and the Slater-Koster two-centre integrals[97]. Our bulk TB parameters for Ge, α-Sn and zinc blende GeSn have been fitted to reproduce the energies and hydrostatic deformation potentials, at selected high-symmetry points in the Brillouin zone, obtained from hybrid functional DFT calculations[68]. We note that the choice of a sp^3s^* TB basis reduces the accuracy of the description of the bulk band structure compared to a larger $sp^3d^5s^*$ basis, tending to overestimate CB and VB edge effective masses. However, our detailed benchmarking versus DFT alloy supercell calculations for $Ge_{1-x}Sn_x$ alloys has demonstrated that an appropriately parameterised sp^3s^* TB Hamiltonian captures quantitatively the key features of the electronic structure, verifying its capability to make quantitative predictions of the alloy properties[68]. The use of a sp^3s^* rather than a $sp^3d^5s^*$ TB basis halves the order of the Hamiltonian matrix for a given supercell, thereby reducing the computational cost associated with the Hamiltonian diagonalisation by close to an order of magnitude, and hence allowing access to larger system sizes with reduced computational cost.

5.3.2 Transport model: Recursive Green's function versus basis compression algorithm

Previous analysis of BTBT in Ge has demonstrated (i) that the BTBT generation rate is dominated by direct (ballistic) BTBT, with minimal contribution from indirect (phonon-assisted) BTBT[14], and (ii) that the BTBT generation rate is largely independent of the orientation of the applied electric field[15]. We therefore restrict our attention to currents generated via direct BTBT. We analyse TFETs using realistic, disordered $Ge_{1-x}Sn_x$ alloys, using supercells that are elongated along the (100) tunneling direction, along which direction open boundary conditions are applied [72]. The boundary conditions in directions perpendicular to (100) depend on the device structure being used. For the DGUTB device there is a periodic boundary condition in the z-direction and open boundary conditions in the y-direction, for the GAA device there are open boundary

conditions in the [100] direction. The devices are surrounded by a 1 nm thick dielectric layer following the designs of Luisier et al. [176] with a dielectric constant of $\epsilon_R = 3.9$. Here, a given supercell is dissected into slabs formed of the minimum number of atomic layers required to generate a nanowire of infinite length via translation along the tunneling direction, allowing to compute a "companion matrix" to the supercell Hamiltonian that can be diagonalised as a function of energy E to obtain the complex-valued supercell wave vectors $\mathbf{K}$. The BTBT current density will be calculated using a BCA as described in section 2.3.3. The choice of the BCA over the more accurate recursive NEGF algorithm was motivated by the greatly reduced computational demand of the BCA compared to the NEGF[124]. This enables us to calculate several configurations at each composition and thereby calculate averages.

5.3.3 Device design and simulation workflow

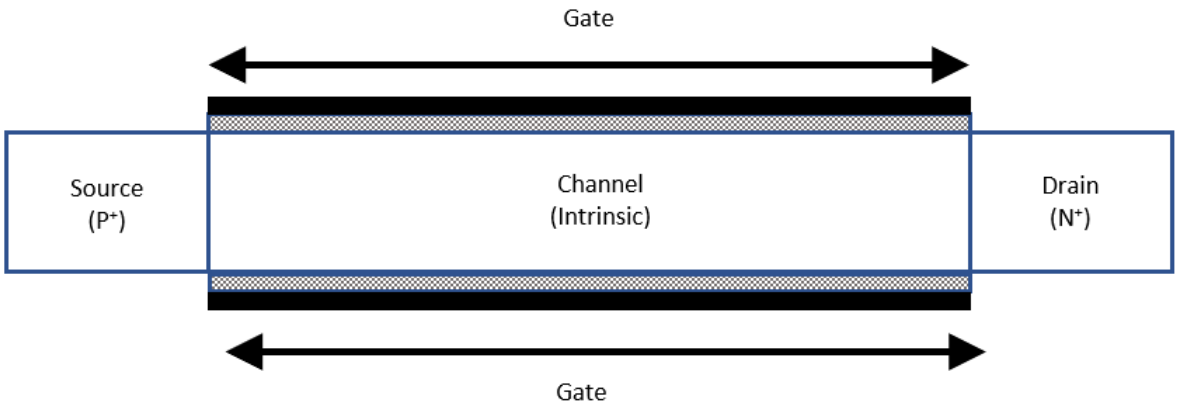

FIGURE 5.3: Diagram of the device structure of a double gate ultra thin body TFET

The basic design of a tunneling transistor consists of a p-doped source, an intrinsic or lightly doped channel and an n-doped drain (Fig. 5.3). However, the final design can vary substantially, consisting of varying geometries and sizes. Key to the design of a TFET is the placement and shape of the gate which can have a large impact on the performance of a TFET. While there are a large number of possible arrangements of the gate and the source-drain region we will investigate two common forms, the double gate ultra thin body (DGUTB) TFET and the gate all around (GAA) TFET. In the DGUTB TFET (Fig. 5.3) transport occurs along the (100) direction with open boundary conditions in this direction. In the periodic (001) direction we will use two unit cells for our GeSn calculations. The GAA TFET consists of a nanowire again separated into the same three regions – source, channel, drain. However, now the nanowire is circular in nature as opposed to square, with a circular gate entirely encompassing the oxide and channel region. In this case there are open boundary conditions in all directions with no periodic boundary conditions. Transport again occurs along the (100) direction. While there are a large number of alternative TFET configurations that have been proposed to improve performance we have selected these two due to their simplicity and we are primarily interested in the change in characteristics of GeSn

TFETs with composition as compared to Ge which will demonstrate the impact of alloy effects on device performance.

To relax the supercell for a DGUTB calculation a Ge supercell of the required size was created and Sn atoms were incorporated either selectively for an ordered TFET or randomly for a disordered TFET. Then the supercell was relaxed using the LAMMPS VFF framework for input to calculations. Conversely the GAA TFET was difficult to form due to its cylindrical nature, requiring that we first relax a larger cuboid supercell, then we "cut-out" a cylindrical nanowire of the required diameter. This necessarily reduces our control of the GAA ordered and disordered compositions compared to a DGUTB TFET.

Transport calculations are carried out using the OMEN software[72] using the GeSn TB parameter sets that we have developed and already applied in chapter 4. Disordered structures are formed by randomly incorporating Sn atoms in place of Ge atoms in a Ge supercell and then relaxing the supercell using the VFF framework. For TFET calculations we apply a fixed drain voltage while varying the gate voltage V_g for a range of values that include the on and off regimes. For all calculations the doping levels of the source and drain region are $1 \times 10^{25}\mathrm{m}^{-3}$ and $4 \times 10^{25}\mathrm{m}^{-3}$ respectively. The OMEN software then calculates the current at each gate voltage comprising our main results[72].

When analyzing the calculations we will be focused on three main characteristics of TFETs, I_{on}, I_{off} and the SS of the TFET. I_{on} is taken as the current when the IV curve reaches a peak after passing the threshold voltage, while I_{off} is the lowest current in the off region. The SS is measured via two methods, the point SS and the average SS. The point SS is calculated at every V_g using Eq. (5.3) while the average SS is calculated using Eq. (5.4). In the next two sections we will analyze the results of transport calculations for both the DGUTB and GAA TFETs with a view to assessing the impact of band hybridisation on the current characteristics.

5.4 Double gate ultra thin body TFETs

In this section we present our work on the current characteristics of DGUTB TFETs where we will carry out three types of calculations. First we will investigate the behaviour of disordered GeSn TFETs as we vary the wire thickness, that is the distance between the gate contacts in Fig. 5.3(a). This will primarily be a benchmarking set of calculations to determine the optimal wire thickness for further calculations. Secondly, we will investigate how the current behaves in disordered wires as we vary the channel length. Finally the main focus of this work will be looking at the impact of Sn incorporation as we vary the Sn composition: in this instance we will investigate both ordered and disordered TFETs. For compositional calculations we will be interested in two atomistic factors, how the current characteristics evolve at low Sn contents due to the impact of CB hybridisation seen in chapter 4 and how disorder impacts the current at larger Sn compositions.

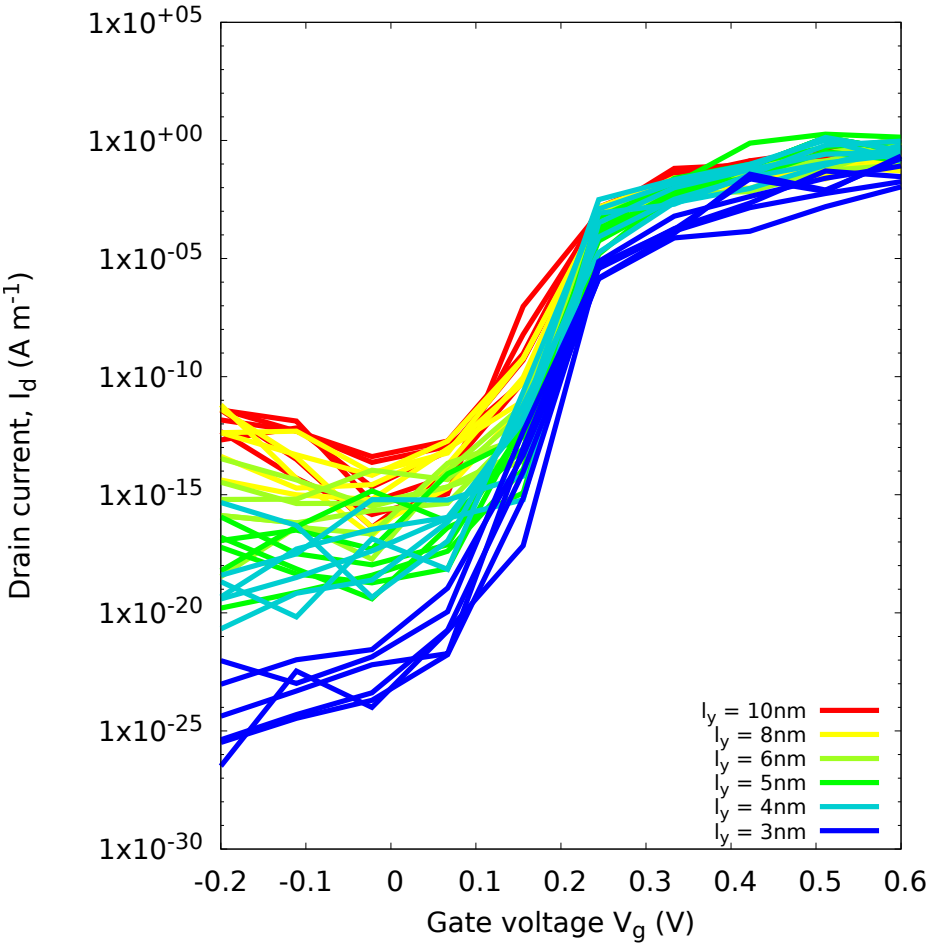

H]

FIGURE 5.4: IV curves for the DGUTB device for a composition of 2% Sn. Curves are coloured based on the thickness between the gate contacts l_y.

5.4.1 Trends with wire thickness

For these calculations we vary the thickness of the DGUTB TFET between the gate contacts while keeping the periodic (001) direction thickness fixed. We use two Sn compositions for these calculations, x = 2, 6%. For each of these compositions we calculate the current characteristics for a range of wire thicknesses ranging from 3nm to 10nm. Wire thicknesses below 3nm cannot be calculated using the OMEN software while thicknesses greater than 10nm require excessive computation times that are costly to run. For each composition and wire thickness pair we calculate the current for six different disordered configurations. This is less than the ten used in the disordered configurations in chapter 4 due to the increased computational requirements of TFET calculations compared to bulk calculations.

Fig. 5.4 shows a plot of the IV curves for these calculations for a composition of x=2%, the IV curves are coloured based on the wire thickness ranging from blue for 3nm to red for 10 nm. From this we can see that there is generally an increase in the current for all gate voltages as the wire thickness increases and that the increase in the off current is much larger than increases in the on current. In the off regime there is large variance in the current of the six configurations for each

composition and wire thickness pair, with a typical range of up to two orders of magnitude while the on current shows much less variation.

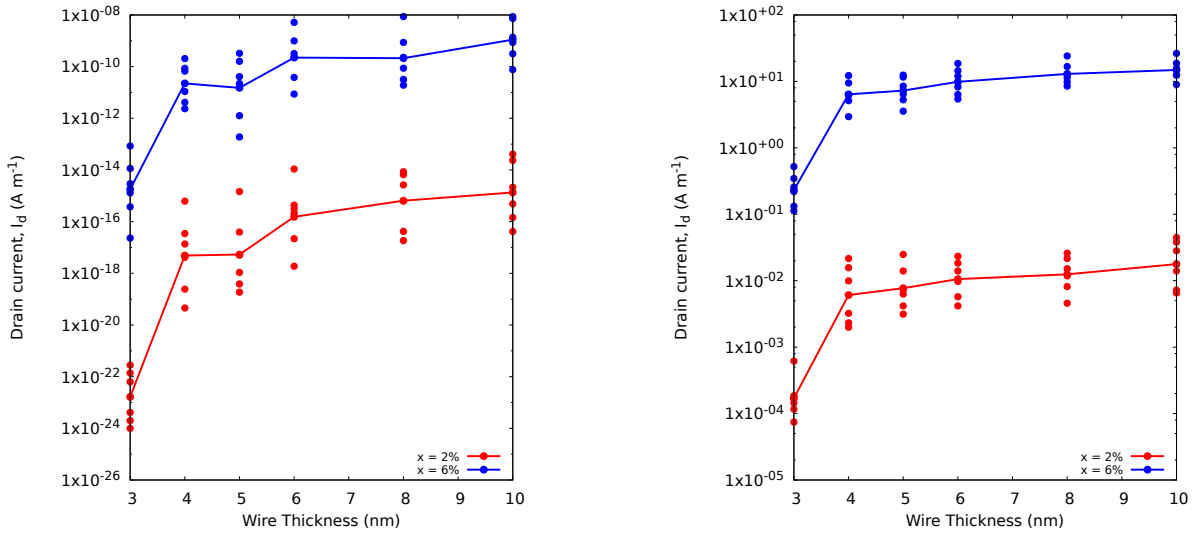

FIGURE 5.5: (a) Drain current of DGUTB versus wire thickness between the gate contacts for a gate voltage in the off state (V_g = -0.02 V). (b) Drain current versus wire thickness in the on state for a gate voltage of V_g = 0.42 V. Data is coloured based on Sn composition (x = 2, 6%). At every wire thickness and composition pair the values for the six disordered configurations are included as points. While solid lines indicate the geometric mean for each composition.

To get a detailed description of the current trends in the IV curves, we plot the current versus the wire thickness for two gate voltages. One in the off region, V_g = 0.02V, and another in the on region V_g = 0.42V. The on and off currents are plotted in Fig. 5.5 for both compositions. In both the on and off states, for both compositions, the current shows little variation for a wire thickness of 4 nm and above, which is in keeping with previous research on InAs TFETs. The variance of the currents at each thickness remains approximately the same though the variance of I_{off} is larger than I_{on} for both compositions.

In Fig. 5.6 we plot the behaviour of the SS_{ave} for these TFETs as we vary the wire thickness. Our SS_{ave} values are all below the target 60mV/decade limit of a MOSFET, with values here reaching a minimum of order 20mV/decade. As we increase the wire thickness the large increase in the off current leads to a reduced SS_{ave} compared to smaller wire thicknesses due to limited increase in the on current. This behaviour occurs for both the point and average SS_{ave} values. The SS_{ave} values seen here are generally much lower than those seen in other theoretical and experimental results[73–85], due to the large impact trap assisted tunneling (TAT)[64] has on the SS_{ave} in experimental calculations and which is included in other theoretical research[64]. Therefore, while our off currents and SS_{ave} results are much lower than contemporary experimental work they represent the best possible values for GeSn TFETs.

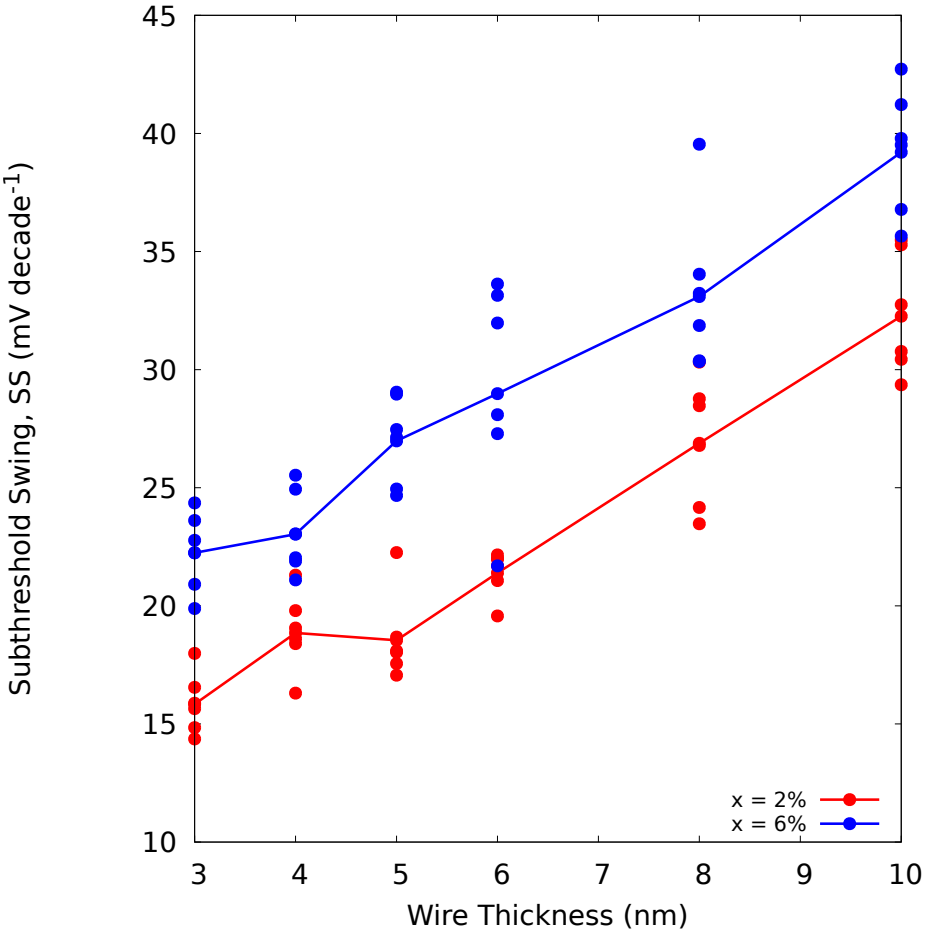

FIGURE 5.6: DGUTB average subthreshold swing vs. wire thickness for Sn compositions of 2, 6%. Included is the geometric mean for each composition (solid line).

5.4.2 Varying channel length

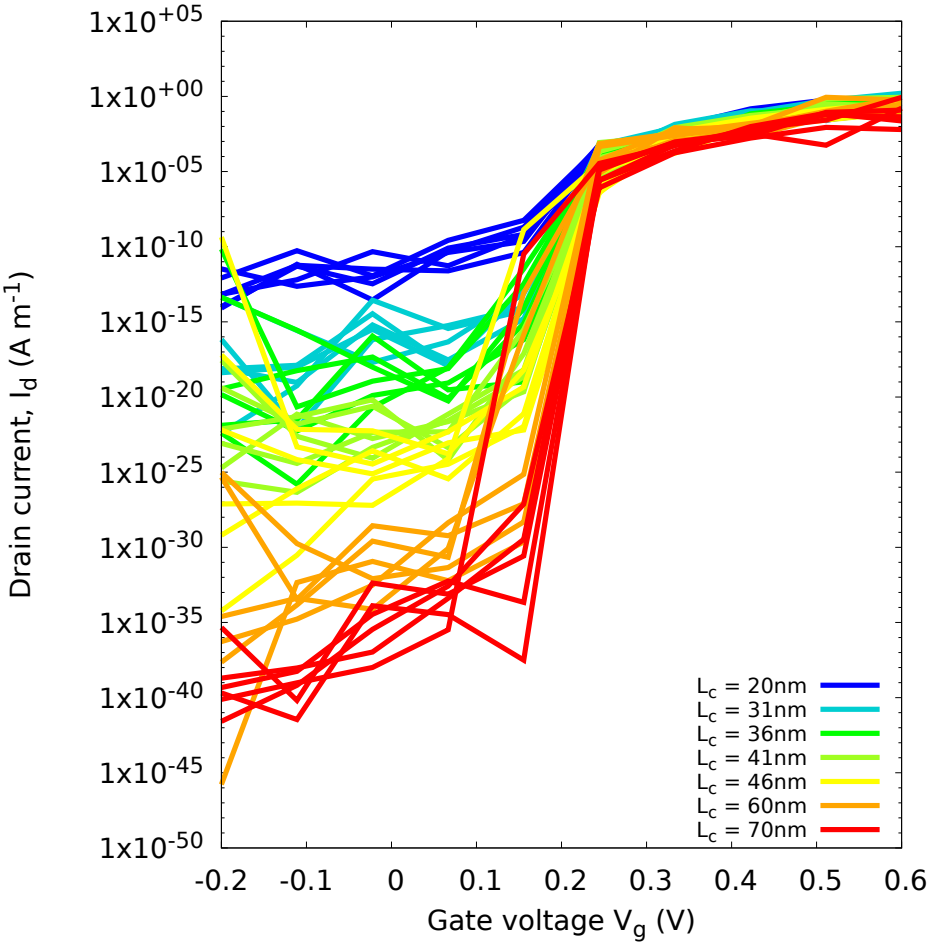

FIGURE 5.7: IV curves for a DGUTB when varying the channel length. IV curves are coloured based on channel length – varying from red for a 70 nm channel length to blue for a 20 nm channel length

Following calculations of the wire thickness we ran calculations where we varied the channel length of the GeSn UTB TFETs, where the gate covers the entire channel. The supercell for these calculations was longer than the previous section, we used a 200x8x2 supercell for a length of approximately 113nm depending on the specific supercell lattice constant. We ran the calculations for a range of channel lengths between 20nm and 70nm, while the drain and source regions made up the remainder of the supercell. Fig. 5.7 shows a plot of the IV curves of these calculations for a composition of x = 2%. We observe an increase in I_{off} as the channel length is reduced; this is due to the reduced tunneling length from the channel to the drain in the off state. This can be seen in Fig. 5.8 by looking at the band diagrams for a long and short channel length and the corresponding IV curves in Fig. 5.7. We can see that the short channel length TFET has a greatly reduced barrier to BTBT compared to the long channel TFET in the off regime; as a result there is a strong increase in the off current, which is still substantially less than the on current but much greater than the off current in the long channel TFET. From the IV curves we can see limited variation in the on currents, with an average increase of approximately an order of magnitude.

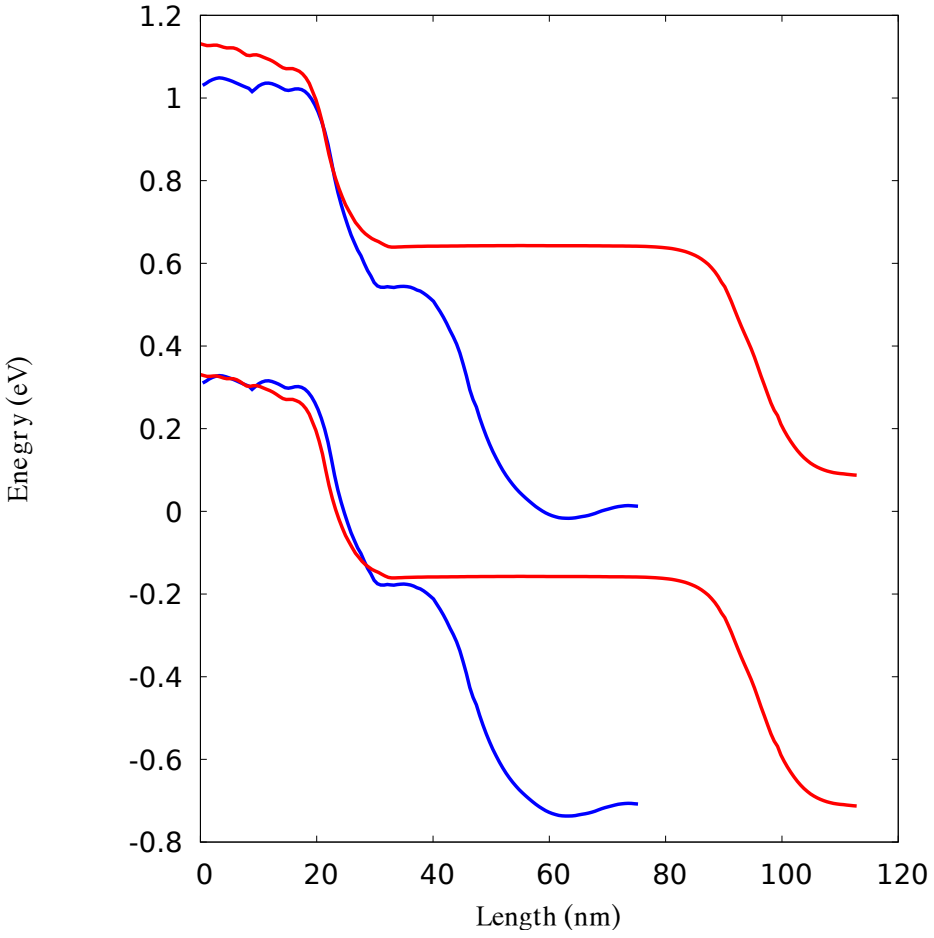

FIGURE 5.8: CB and VB edges for two DGUTB TFETs with different channel lengths. A short 20 nm channel length device (blue) and a long 70 nm channel length device (red)

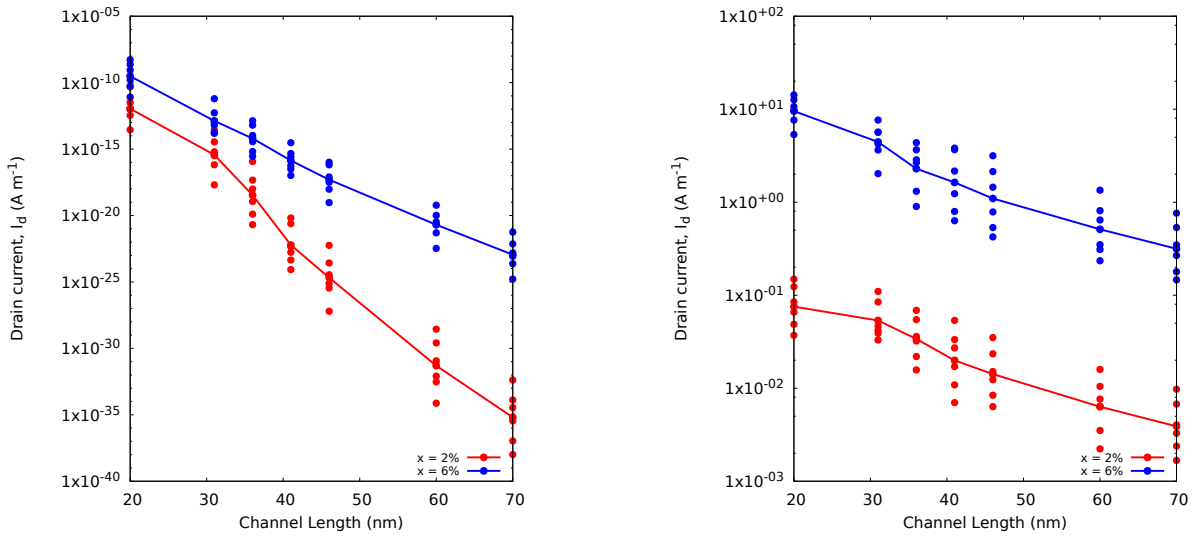

(a) (b)

FIGURE 5.9: (a) Drain current of DGUTB TFET versus channel length for a gate voltage in the off state (V_g = -0.02 V). (b) Drain current versus channel length in the on state for a gate voltage of $V_g = 0.42$ V, the on state. For each channel length and composition pair we include values from the six disordered configurations as points. The geometric mean is included as solid lines for each composition.

In Fig. 5.9 we plot I_{on} and I_{off} versus channel length for x =2% (red) and 6% (blue), from which we can see an increase in I_{on} of approximately an order of magnitude while I_{off} increases by approximately ten orders of magnitude for $x = 6\%$. Comparing the variation between the two compositions at lower channel lengths the difference between I_{on} for the 2% and 6% composition reduces to less than an order of magnitude. In Fig. 5.10 we show how the SS_{ave} varies with channel length, as would be expected from the increase in the off current the SS_{ave} increases with decreasing channel length, with the lowest SS_{ave} values of $\approx$ 10 mV/decade for x =2% and $\approx$ 15 mV/decade for $x = 6\%$.

5.4.3 Trends with Sn composition

The key aspect of the GeSn-based TFETs in which we are interested for this work is the behaviour of the current characteristics as we vary the Sn composition. From the results of chapter 4 we demonstrated that there is an enhanced generation rate in atomistic alloy transport calculations of GeSn supercells when compared to VCA calculations for low Sn compositions, x. This enhanced generation rate shows the importance of including atomistic effects when undertaking calculations for values of x below the predicted Γ-L crossover composition. Here, we determine how this enhanced generation rate impacts on TFET calculations.

We calculate the current characteristics for Ge and for two sets of GeSn supercells – ordered and disordered. For ordered supercells we use the same Sn compositions seen in chapter 4, x = 1.56, 6.25%. For disordered calculations we use a range of Sn compositions between 1-10% Sn, where for each Sn composition we use six disordered configurations. From our calculations where we

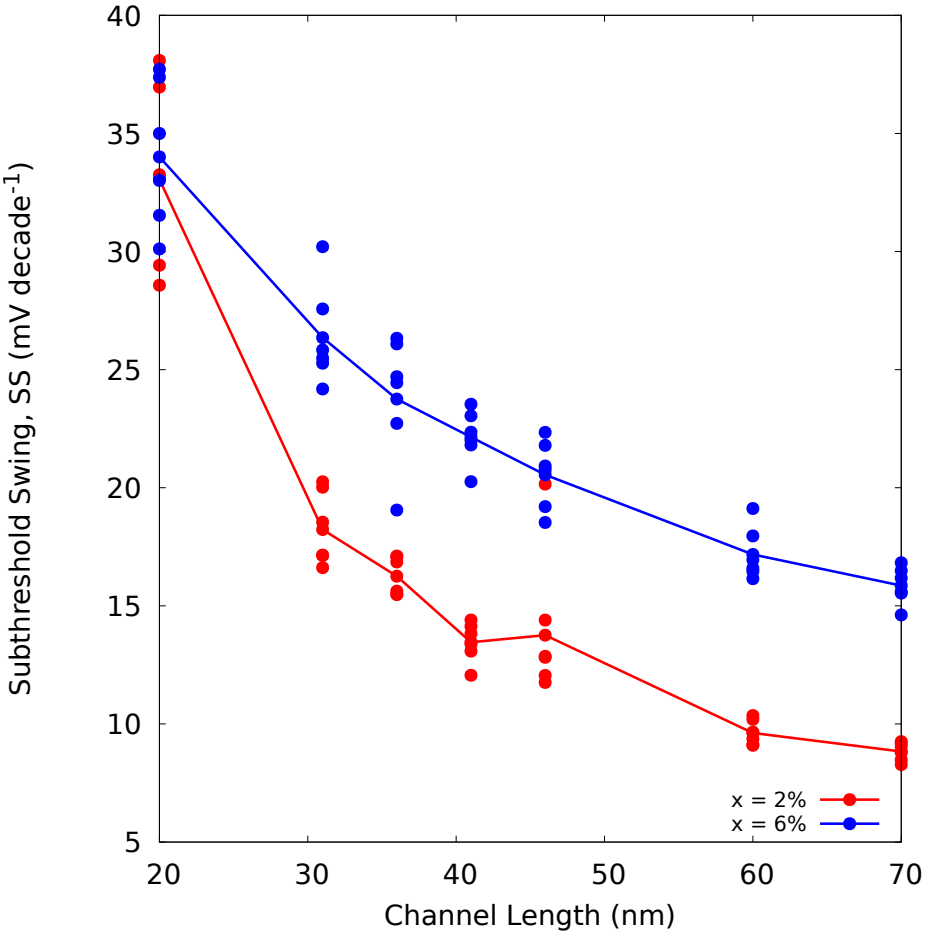

FIGURE 5.10: DGUTB average subthreshold swing vs. channel length for Sn compositions of 2, 6% for each of the six disordered configurations (points). Included is the geometric mean for each composition (solid lines).

varied the wire thickness the current shows little variation for a thickness of 4 nm and above. We therefore choose a thickness of 4mm for composition based calculations, specifically we use a 148x8x2 supercell consisting of on the order of 10^4 atoms. Choosing the lowest possible wire thickness was motivated by the large increase in computation time when increasing the thickness of the supercells. A channel length of 60 nm was chosen for these calculations.

5.4.3.1 Ordered alloy structures

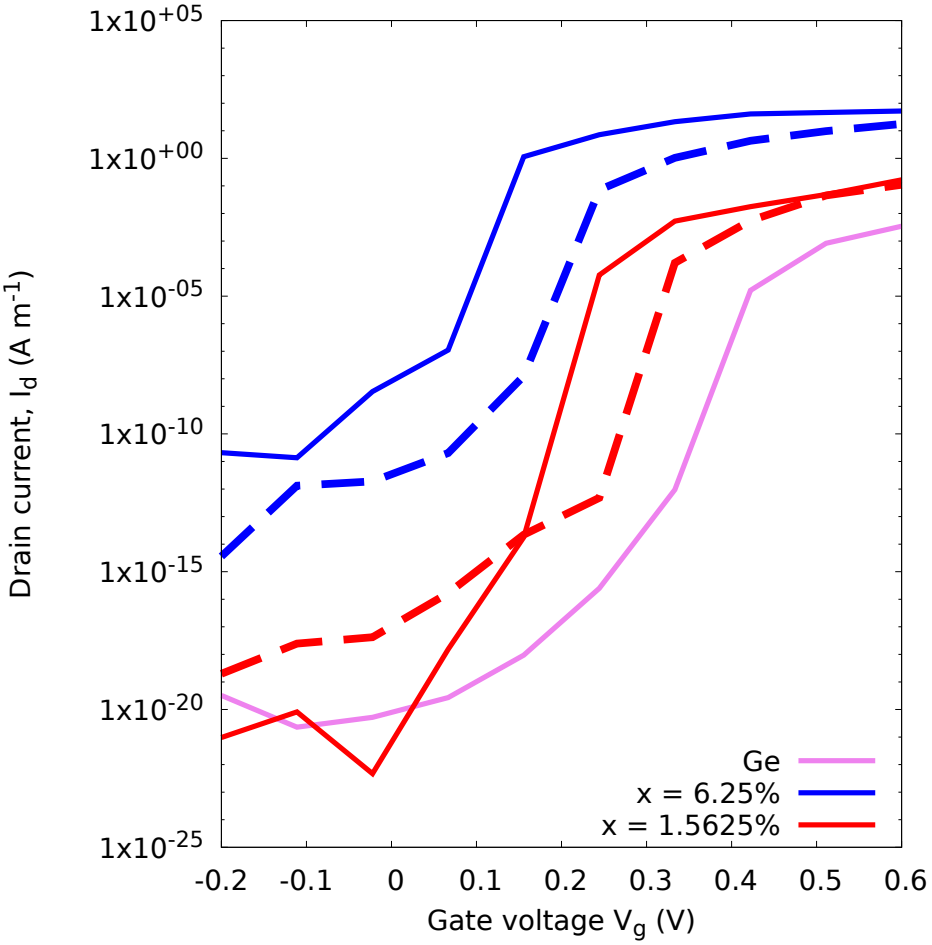

FIGURE 5.11: IV curves for ordered GeSn DGUTB TFETs and a Ge TFET. VCA based GeSn TFET IV curves are included as dashed lines. Lines are coloured based on Sn composition.

Fig. 5.11 shows the IV curves for Ge (purple line) and the two ordered GeSn supercells (1.56% orange solid; 6.25% blue solid). We note the expected increase in I_{on} and I_{off} as we increase Sn composition compared to Ge and that I_{off} increases by a greater margin than I_{on}. However, I_{on} still increases significantly, for the 6.25% supercell I_{on} reaches a value of 2A/m which is approximately five orders of magnitude greater than Ge. The lower composition also sees an increase compared to Ge with an increase in I_{on} of two orders of magnitude. For comparison we include VCA based calculations at the same compositions. Here the VCA is calculated using Eq. (4.1), with no matching to the alloy bandstructure as in section 4.6. From this we can see there is an increase in I_{on} for both of the atomistic calculations compared to the VCA based calculations, this is primarily due to the difference in band gap between the VCA and atomistic calculations. The SS for both GeSn ordered supercells show a large decrease from that of Ge, from 40 mV/decade to 15mV/decade in line with the reduced values already observed for disordered GeSn alloys in Fig. 5.10.

5.4.3.2 Random alloy structures

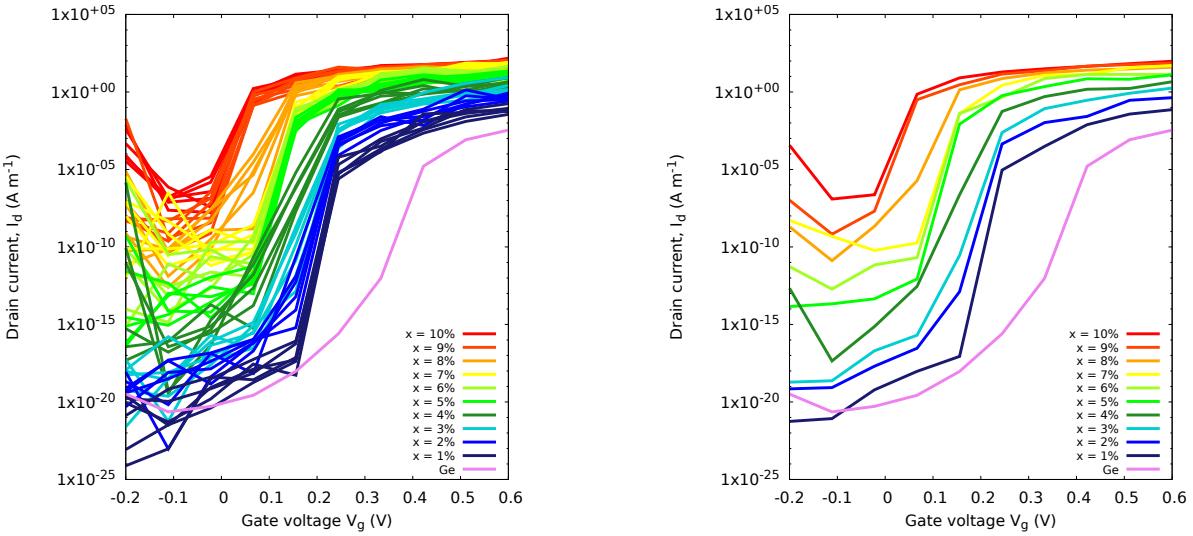

(a) (b)

FIGURE 5.12: (a) IV curves for each of the six disordered configurations of GeSn TFETs for compositions in the range 1 - 10% Sn. The IV curve for Ge is also included. (b) Geometric mean of the six disordered configurations at each composition

Fig. 5.12 shows the IV curves for Ge and the disordered GeSn supercells and the two ordered GeSn supercells. Upon incorporation of 1% Sn there is an immediate order of magnitude increase in I_{on} while there is limited change in I_{off}. After this initial jump there is an increase in both I_{on} and I_{off}, where I_{off} increases by fourteen orders of magnitude and I_{on} increases by five orders of magnitude.

In Fig. 5.13 we plot the current versus Sn composition for Ge and the ordered and disordered GeSn supercells for two gate voltages, one in the off regime (-0.02 V) and one in the on regime (0.42 V). We see there is an immediate jump in I_{on} due to Sn incorporation for both the ordered and disordered supercells, as composition increases I_{on} increases, though the rate at which the current is increasing slows as composition increases and tends to reach a maximum current of the order 10^2 $\frac{A}{m}$ for this structure. This is an increase of eight orders of magnitude compared to Ge at the same field. Disorder does have impact on I_{on} for these TFETs, the ordered 6.25% composition TFET has a larger I_{on} than similar disordered compositions (6, 7%) while the 1.5625% ordered composition has a similar I_{on} to the 1% and 2% disordered supercells. Once I_{on} reaches a value of 10^2 $\frac{A}{m}$ there is limited increase with larger compositions, however, I_{off} continues to increase. I_{off} does not reach a maximum value and instead tends to increase continuously as Sn composition increases, this represents the shortcoming of high Sn content devices whereby I_{off} becomes unmanageable. These calculations underestimate I_{off} and represent an ideal case without TAT that dominates I_{off} in fabricated devices, however, these I_{off} trends suggest that even if TAT is minimized I_{off} will still remain large compared to I_{on} at high Sn contents with a I_{on}/I_{off} ratio of only 10^5. GeSn TFETs have been fabricated for composition from 2 – 8%[59, 61, 63, 64]. For fabricated TFETs the

lowest reported value for the point SS was 215 mV/decade [64], our calculations return much lower values for the average SS due to the lack of TAT in our calculation which serves to dramatically increase I_{off}. I_{on} values for fabricated TFETs are in a similar range as our calculations with the largest reported I_{on} = 22 A/m at x = 5%[59]. In Fig. 5.13 we see a large spread in the currents at individual compositions, with up to a two orders of magnitude spread in I_{off} and one order in I_{on}. As compared to other random alloy calculations a spread of more than an order of magnitude in I_{on} is typical[172, 177].

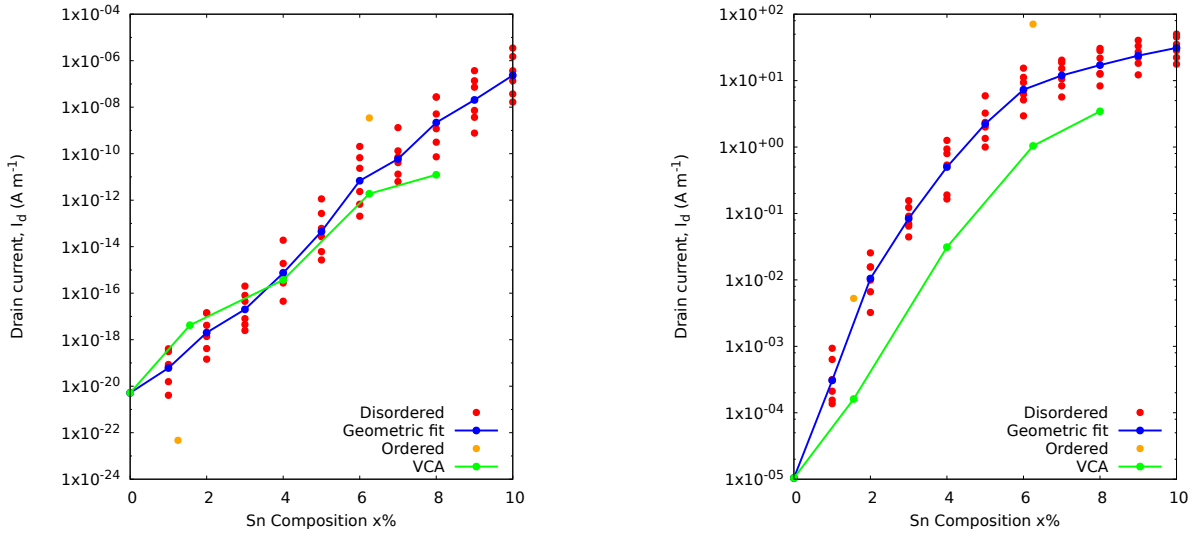

FIGURE 5.13: (a) Drain current of DGUTB versus Sn composition between the gate contacts for a gate voltage in the off state (V_g = -0.02 V). (b) Drain current versus Sn composition in the on state for a gate voltage of V_g = 0.42, the on state.

In Fig.5.14 we plot the trend of the SS versus composition for Ge and the ordered and disordered GeSn supercells. The SS shown here are the average SS (red) and the lowest point SS (blue) for each device. There is an immediate drop in both trends upon incorporation of Sn, with a point SS of 15 mV/decade and a average SS of 25mV/decade. At higher compositions there is an increase in the SS due to a lower I_{on}/I_{off} ratio, by a composition of 10% the average SS reaches a value of 45 mV/decade. We note that these represent the lowest possible SS for these devices and that fabricated devices will likely have much greater SS due to the presence of TAT[64]. In comparison to other random alloy calculations a spread of up to 70 mV/decade has been observed[177].

In summary our analysis of DGUTB devices demonstrates that the atomistic effects observed in our bulk generation rate calculations translates to the current characteristics of GeSn TFETs. We demonstrate an increase in the on current upon incorporation of small quantities of Sn in excess of that predicted by a VCA-based calculation and a substantial drop in SS values. Up to a composition of 10% Sn we see an increase in I_{on} of eight orders of magnitude compared to Ge.

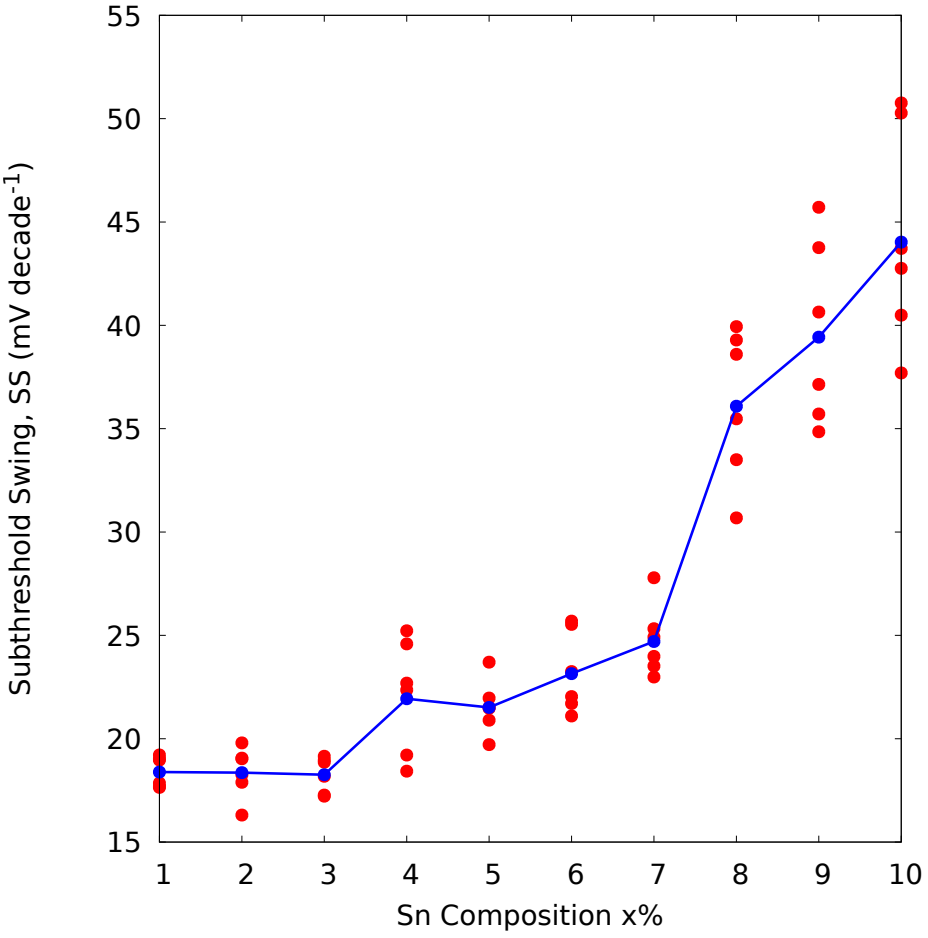

FIGURE 5.14: DGUTB subthreshold swing vs. Sn compositions. Including is the geometric mean(solid line).

5.5 Gate all around TFET

We next investigate the second TFET device, the GAA TFET. In this section we will be interested in two types of calculations, first the behaviour of disordered GeSn TFETs as we vary the wire thickness, in this case the diameter of the wire due to its cylindrical nature. This is primarily be a bench marking set of calculations to determine the optimal wire thickness for further calculations. Secondly we will focus on the impact of Sn incorporation on the current characteristics as the Sn content is varied, here we will again present results for both ordered and disordered supercells. For compositional calculations we will be interested, how the current characteristics change at low Sn contents due to the impact of CB hybridisation and the role of disorder.

GAA TFETs are three dimensional objects as compared to the two dimensional UTB TFETs, as a result there is a significant increase in the computational requirements of calculations with GAA TFETs. This limits the size of the supercells we will use in these calculations, compared to DGUTB supercells they will in general have 60-70% less atoms. We do not to carry out calculations where we vary the channel length for GAA TFETs as only a small range of channel lengths could

be simulated due to the excessive computational times required for supercells with larger channel lengths.

5.5.1 Trends with wire thickness

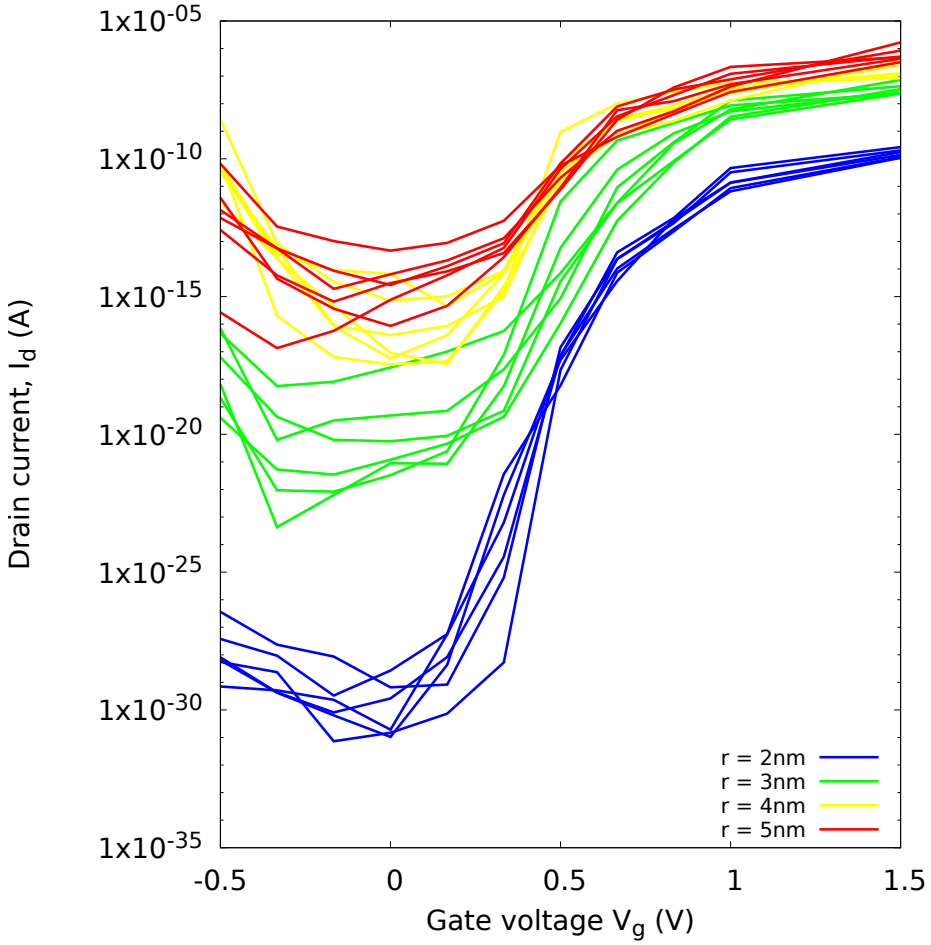

FIGURE 5.15: IV curves for a GAA device at a Sn composition of 2%. The curves are coloured based on the diameter of the wire.

For GAA TFETs, we vary the wire diameter from 2nm to 5nm while the total length of the TFET is 40nm. These calculations are performed at the same compositions as the DGUTB TFETs, x = 2, 6%. However, for GAA TFETs there will be some variation of the composition due to the process of forming the wire (section 5.3.3), where the cylindrical wire is cut out of a larger block which has compositions of x = 2, 6%. These calculations occur at $V_{ds} = 0.3$V and drain and source doping of 1×10^{20}cm^{-3}. In Fig. 5.15 for a composition of x = 2% we plot IV curves coloured based on the wire diameter. As in section 5.4.1 we see that I_{off} increases for both compositions with increasing diameter while there is a smaller increase in I_{on}. I_{on} increases by three orders of magnitude over this range, with I_{on} reaching a plateau where further increases in the diameter yield minimal increase in I_{on}. For the largest diameter wire of 5 nm the I_{on}/I_{off} ratio is approximately on the order of 10^5. For comparison the largest I_{on}/I_{off} ratio in fabricated TFETs is 10^3[64].

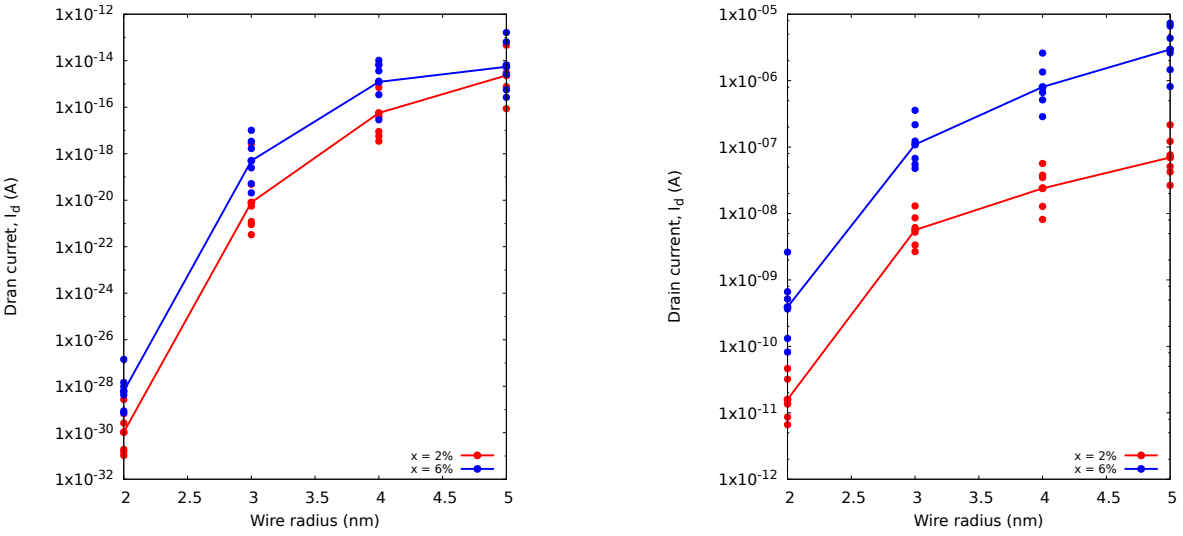

(a) (b)

FIGURE 5.16: (a) Drain current of GAA TFET versus wire diameter between the gate contacts for a gate voltage in the off state (V_g = -0.02 V). (b) Drain current versus wire diameter in the on state for a gate voltage of V_g = 0.42 V, the on state. Data is shown for composition of 2% (red) and 6% (blue). Points indicate current values from each disordered configuration while lines represent the geometric mean of each group of six disordered configurations.

Plots of the I_{on} and I_{off} versus diameter in Fig. 5.16 show a similar trend as in section 5.4.1, I_{on} approaches a maximum for a wire diameter of 4nm, the same thickness as for the DGUTB TFETs. There is some increase for larger diameters though not substantial compared to the initial increase. For further calculations when varying the composition of the GAA TFETs we will use a TFET with a diameter of 4nm. We aim to keep the diameter as small as possible due to the large increase in computational requirements for thicker wires, which is more pronounced when using GAA TFETs than DGUTB TFETs as the UTB structure is periodic in the z-direction.

5.5.2 Trends with Sn composition

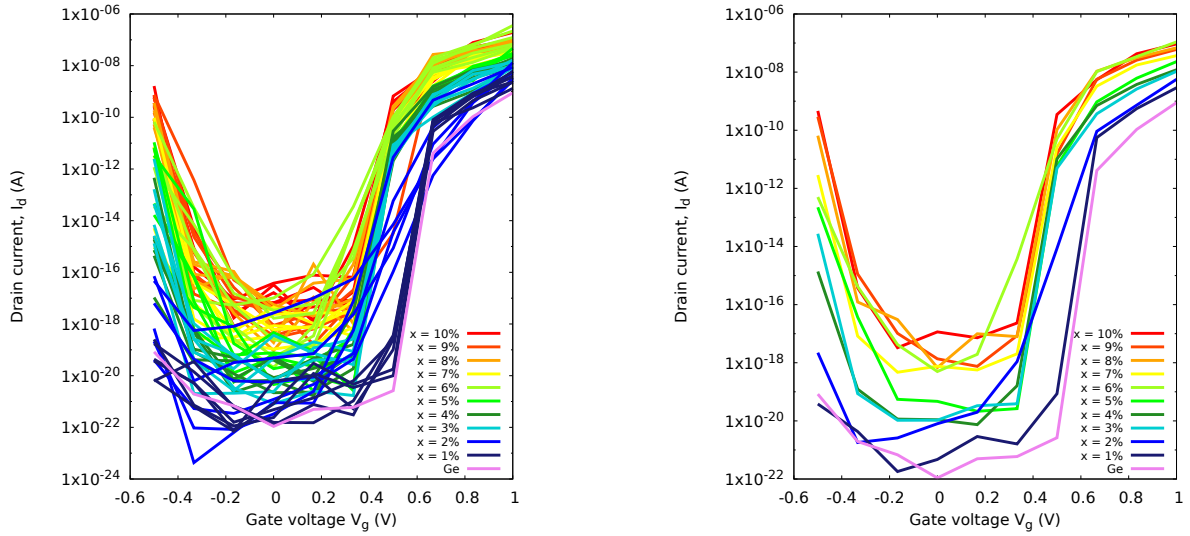

(a) (b)

FIGURE 5.17: (a) IV curves for each disordered configuration for GeSn TFETs in the composition range 1 - 10% Sn. The IV curve for Ge is also included. (b) Geometric mean of the six disordered configurations at each composition

In Fig. 5.17 we plot the IV curves of all the GeSn disordered supercells along with Ge for GAA TFETs. We observe that both I_{on} and I_{off} increase with larger Sn compositions and that there is an initial jump in I_{on} upon incorporation of 1% Sn. As composition increases I_{on} tends to reach a maximum value. I_{off} increases at a faster rate than I_{on} as was seen with DGUTB TFETs and the increase in I_{off} remains consistent as composition increases, this in turn will lead to a larger SS for the GAA GeSn TFETs due to the reducing I_{on}/I_{off} ratio. In Fig. 5.18 we include plots of I_{on} and I_{off} versus Sn composition for Ge and for both the ordered and disordered GeSn GAA TFETs. We see that the increase in I_{on} falls off at higher Sn compositions, particularly above 6% Sn while the off current increases continuously with composition. While at low Sn compositions there is an increase in I_{on}, with an increase of almost an order of magnitude for the initial 1% increase in Sn composition. The ordered 6.25% Sn GAA TFET has a larger I_{on} than the corresponding disordered compositions (6, 7%) due to a smaller band gap. For both I_{on} and I_{off} there is limited difference between the ordered 1.56% Sn composition and similar disordered compositions, which is in line with generation rate calculations from chapter 4. The overall increase in the on current is over two orders of magnitude compared to Ge, this is largely due to a reduction in the band gap.

To compare the SS between the GAA and DGUTB TFETs we required the two structures to have approximately the same channel length, as in section 5.4.2 we saw that varying the channel length can impact the currents and SS. To achieve an equal comparison we set up a new DGUTB structure – a 98×8×2 supercell with a channel length of 20 nm. Running compositional calculations as in section 5.4.3.2 allowed us to compare the SS between the GAA and DGUTB TFETs. In Fig. 5.19 we plot the trend of the average SS for both the GAA and DGUTB TFETs. We can

see the GAA TFETs have a lower SS than all DGUTB compositions and a SS in the range of 20-30 mV/decade. For low compositions the DGUTB TFETs have SS near the 60 mV/decade benchmark, but increasing the composition to 10% raises the SS to 120 mV/decade. The poor performance of the DGUTB is expected due to the reduced gate contact area compared to the GAA TFET. All of the GAA TFETs have average SS below the critical 60 mv/decade benchmark. However, these are ideal calculations which do not include the TAT seen in real devices; therefore our SS results significantly underestimate experimental results where the SS is typical in the range of 200-1000 mV/decade[59, 62, 64, 178].

Overall the results of the GAA TFET calculations show similar trends as the DGUTB TFETs, confirming that the impact of Sn incorporation persists across TFET designs. The key points of interest are the low SS values that are achievable when TAT can be minimised and the large increases in I_{on} as Sn composition increases while maintaining a sufficiently large I_{on}/I_{off} ratio in the absence of TAT. Further, the initial increase in I_{on} of more than an order of magnitude may be beneficial for use in Ge TFET designs which currently have both low SS and off currents but on currents that are too small for general use. Incorporation of small quantities $\leq 2\%$ of Sn may improve the prospect of these designs.

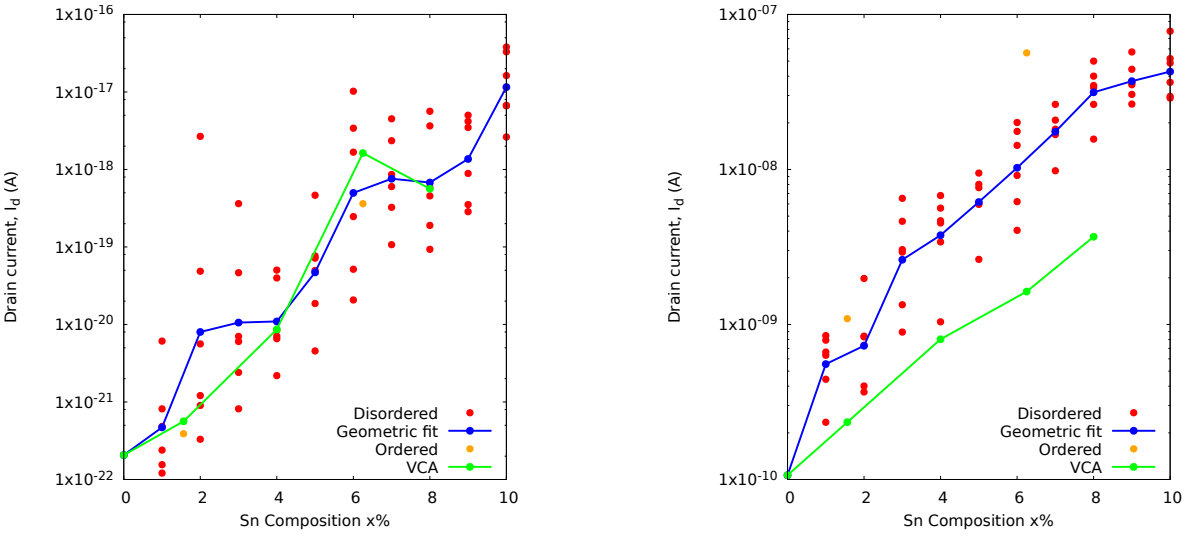

(a) (b)

FIGURE 5.18: (a) Drain current of GAA versus Sn composition between the gate contacts for a gate voltage in the off state (V = 0.0). (b) Drain current versus Sn composition in the on state for a gate voltage of V = 0.8333, the on state. Also included in green are results for calculations with VCA parameters. Ordered calculations at 1.5625% and 6.25% are included as orange points.

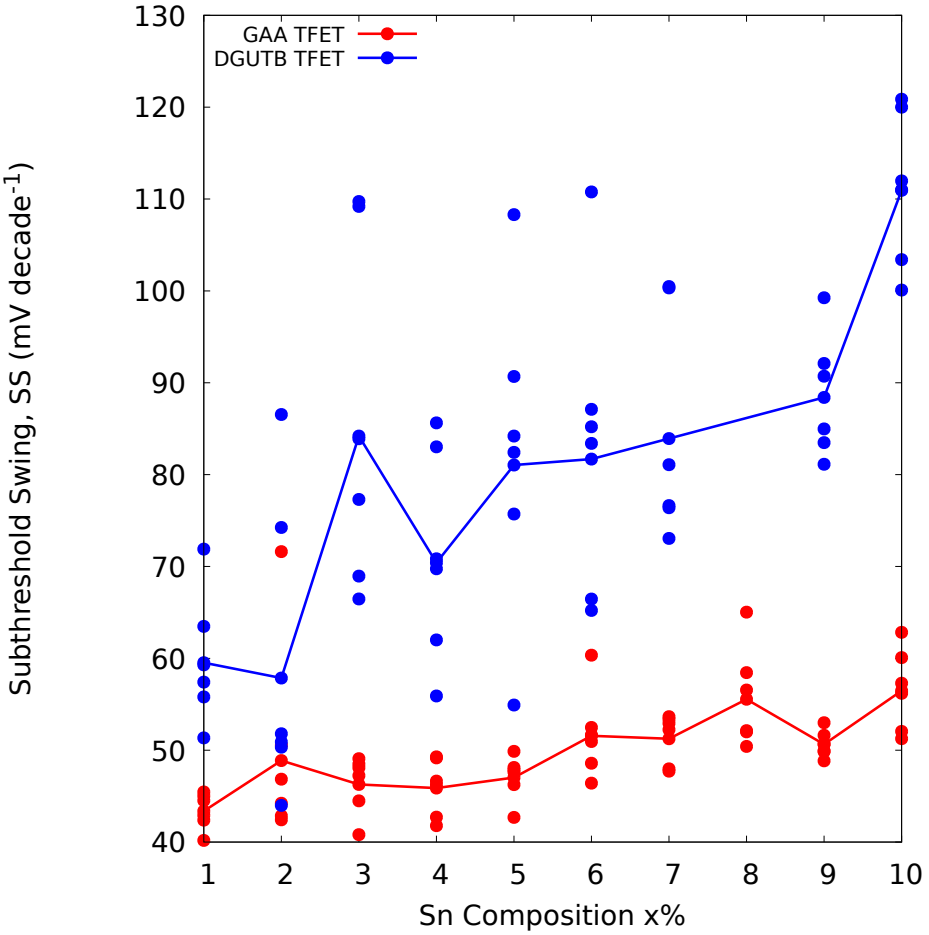

FIGURE 5.19: SS versus Sn composition for a GAA TFET (red) and for a DGUTB TFET (blue). Points are for each individual disordered configuration while lines are for the geometric mean of the six configurations at each composition. Both structures have a channel length of approximately 20 nm.

5.6 Conclusion

In summary we have provided an analysis of the current characteristics of $Ge_{1-x}Sn_x$ based TFETs. We established an atomistic calculational framework to analyse BTBT in $Ge_{1-x}Sn_x$ alloys, encompassing lattice relaxation based on a fully analytic VFF potential, electronic structure calculations based on a nearest-neighbour TB Hamiltonian, and quantum kinetic BTBT calculations based on a BCA solution of the coupled Schrödinger-Poisson equations. This framework allows for predictive, large-scale and high-throughput calculations of the electrical properties of $Ge_{1-x}Sn_x$ based TFETs. We applied this approach to move beyond the limitations imposed by the commonly-employed VCA, to elucidate the impact of atomistic electronic structure effects on the current characteristics of $Ge_{1-x}Sn_x$ TFETs. In this work we investigate the current characteristics for two TFET devices, a DGUTB TFET and a GAA TFET, these calculations are carried out for a range of Sn compositions and device dimensions.

Previous analysis of TFETs based on $Ge_{1-x}Sn_x$ have centred on a single approach, comprising electronic structure calculations performed in the VCA, which are used as input to semi-classical BTBT calculations based on the WKB approximation[73–85]. This approach implicitly neglects atomistic effects, assuming that the indirect- to direct-gap transition occurs abruptly at a single, critical Sn composition. Our atomistic calculations highlight that this indirect- to direct-gap transition in fact proceeds continuously with increasing x, driven by alloy-induced hybridisation between the L_{6c} CB minimum and Γ_{7c} CB edge states of the Ge host matrix semiconductor. Our analysis in chapter 4 have demonstrated the impact of this hybridisation on the alloy complex band structure and as a result the BTBT generation rate for $Ge_{1-x}Sn_x$ alloys. Here we extend the work of chapter 4 to determine the effect the enhanced generation rate has on the current characteristics of $Ge_{1-x}Sn_x$ based TFETs.

For DGUTB TFETs we carried out calculations for both ideal ordered and real-like disordered TFETs. Ordered calculations reveal an increase in I_{on} of eight orders of magnitude compared to Ge for a composition of 6.25% Sn. SS values are small – in the range 20-30 mV/decade, which are consistently below the 60mV/decade MOSFET limit. A comparison that we made to VCA-based calculations show that atomistic calculations have I_{on} much larger then those achieved when using VCA parameters, though at similar compositions the VCA parameters will give lager band gaps than atomistic parameters. We chose these VCA parameters to compare with other theoretical calculations[13, 64, 77, 83]. For realistic, disordered $Ge_{1-x}Sn_x$ alloys we quantified the characteristics of the TFETs via high-throughput, large-supercell transport calculations, which demonstrate a large increase in I_{on} compared to Ge, with a total increase of six orders of magnitude for a composition of 10% Sn. Disordered calculations have a reduced I_{on} compared to similar ordered calculations demonstrating the impact of local alloy disorder on the $Ge_{1-x}Sn_x$ TFETs. However, they are still in excess of corresponding VCA calculations. In line with our work from section 4.6 the greatest change and increase in the on current occurs for lower Sn compositions with an initial increase of two orders of magnitude at a composition of 1% Sn. I_{on} increases to a maximum of six orders of magnitude more than Ge, while I_{off} increases continuously with composition, reducing the I_{on}/I_{off} ratio at large compositions and thereby increasing the SS. In this work other tunneling paths in the off state have been neglected such as TAT which, it has been shown can substantially increase I_{off}[64]. As such our I_{off} values represent an ideal situation that could be reached with improved growth and fabrication processes. Overall, our subthreshold swing calculations reach low values in the range 10-20 mV/decade which is due to the low I_{off}. Varying the channel length was found to have minimal impact on I_{on} with up to an order of magnitude increase when going from a channel length of 70nm to 20nm, while I_{off} increase substantially (ten orders of magnitude for a composition of 6% Sn) over the same range.

We then carried out similar calculations with the more computationally intensive GAA TFET architecture. Compositional calculations revealed similar behaviour as the DGUTB device with a large increase in the ordered I_{on} compared to Ge with an increase of two orders of magnitude for a composition of 6.25% Sn. Disorder serves to reduce I_{on} compared to ordered structures demonstrating the impact of local alloy disorder on the current through an increase in the band

gap. The disordered I_{on} increases by two orders of magnitude compared to Ge, with the largest increases occurring at lower composition. Increases in I_{off} caused the SS to gradually increase as composition increased with the largest SS of 60 mV/decade at a composition of 10% Sn.

Overall, our analysis highlights that previously overlooked atomistic effects play an important role in governing the electrical properties of $Ge_{1-x}Sn_x$ TFETs, and that inclusion of these effects in TFET calculations predicts a significant enhancement in I_{on} compared to Ge and VCA based calculations. We conclude that the impact of Sn incorporation on the CB structure of $Ge_{1-x}Sn_x$ alloys can then allow for higher on-state currents in $Ge_{1-x}Sn_x$-based TFETs than previously predicted. Further, the large increase in I_{on} upon incorporation of small quantities of Sn will be attractive for improving existing Ge based TFETs without the drawback of large increases in disorder effects. This, combined with the ability to tune the band gap via Sn composition and nanostructuring, provides broad scope to engineer performance and obtain competitive characteristics from CMOS-compatible TFETs.

Chapter 6

Conclusions and outlook

The work presented in this thesis comprises a theoretical analysis of the material, optical and electronic properties of germanium based group IV alloys and their utility for group-IV CMOS compatible optoelectronics and post-CMOS electronic devices. In this thesis we focus on two Ge based group-IV alloys, $Ge_{1-x}C_x$ and $Ge_{1-x}Sn_x$, which have attracted interest in recent years due to their predicted direct gap behaviour. $Ge_{1-x}C_x$ alloys are the focus of chapter 3 and $Ge_{1-x}Sn_x$ alloys are the focus of chapters 4 and 5. In this final chapter we summarise the key findings and the main conclusions of our research into each of the alloys and discuss their future outlook.

6.1 Background and motivation

The continued development of Si-based CMOS technologies are limited in two key areas, (i) the integration of optical and electronic devices on a single chip and (ii) applications requiring low power devices with a steep switching mechanism. A long held goal of the semiconductor community is the combined integration of electronic and optical devices. The future potential of CMOS-related technologies is limited by the current deficit of active photonic components that are compatible with Si-based devices. Active photonics are severely limited by Si due to its fundamental indirect band gap, making it an inefficient emitter of light. For low power devices the size of current transistors has reached the limits that can be supported by CMOS technology. As a result novel device designs have been sought, chief among which are those that work on the principle of band to band tunneling such as TFETs. Si again serves as a roadblock to the development of TFETs due to its indirect band gap that significantly reduces the efficiency of TFETs. To progress in these two areas the use of Si-compatible group-IV materials has been considered; already these materials have been used in other CMOS frameworks.

Ge-based optoelectronics has received the most interest in recent years due its compatibility with Si and the small difference between its indirect fundamental band gap and its direct band gap, which is less than 150meV. This makes band engineering of Ge a highly attractive route to direct gap group-IV alloys. The work in this thesis focuses on determining the suitability of the two alloys $Ge_{1-x}C_x$ and $Ge_{1-x}Sn_x$ for applications that require a direct gap group-IV alloy. For $Ge_{1-x}C_x$ we investigated the formation of a direct band gap that could be used for active photonic components.

In $Ge_{1-x}C_x$ alloys the incorporation of dilute quantities of C into the Ge lattice has been predicted to from a C-related state in the band gap with a minimum in the zone centre, thereby forming a direct band gap. While for $Ge_{1-x}Sn_x$ we will be interested in its performance as a TFET for post-CMOS computing. Incorporation of Sn induces hybridisation of the Ge derived conduction band edge Γ and L states, initially forming a quasi-direct band gap. This behaviour in $Ge_{1-x}Sn_x$ alloys and its implications for band to band tunneling in $Ge_{1-x}Sn_x$ alloys has received limited research focus. Here we quantitatively examine the effect of the hybridised band gap on the BTBT generation rate in $Ge_{1-x}Sn_x$ alloys and then the effect on TFET devices.

6.2 Group-IV optoelectronics of $Ge_{1-x}C_x$

In chapter 3 we provided a detailed theoretical analysis of the behaviour of $Ge_{1-x}C_x$ alloys upon substitutional incorporation of C in a Ge lattice. To date, there have been few theoretical investigations of the electronic band structure evolution of Ge upon incorporation of dilute quantities of C. Existing research provides a range of conflicting reports on the nature of the band gap of $Ge_{1-x}C_x$ alloys, including observation of strong band gap bowing and the emergence of a direct band gap for a limited range of C compositions. Further research has suggested that incorporation of C in Ge leads to the evolution of a direct band gap due to the formation of a C-related localised state; this localised state is then predicted to undergo a BAC interaction with the extended Γ_{7c} zone centre CB edge states of Ge. However, recent theoretical analysis based on density functional theory calculations has cast doubt on these predictions, DFT calculations have demonstrated that C acts as an isovalent impurity leading to the formation of C-related localised state within the Ge host matrix band gap. A deeper understanding of the evolution of the C-related localised state is required before a conclusion can be made on the suitability of $Ge_{1-x}C_x$ for photonics; this is the aim of the work performed in chapter 3 of this thesis.

In chapter 3, we set out to investigate the impact of C incorporation on Ge. To achieve this we set up a large multi-scale framework to analyse $Ge_{1-x}C_x$ supercells with up to 10^4 atoms. Our calculations were based on a computationally efficient and highly-scalable semi-empirical atomistic framework, consisting of (i) structural relaxation using a VFF potential, and (ii) electronic structure calculations using a sp^3s^* TB Hamiltonian. Previous work in our group consisted of DFT calculations from which we acquired parameters for the TB and VFF models for the constituted materials Ge , C and the IV-IV compound zb-GeC. In this work we bench marked the performance of the TB and VFF parameters via comparison between the $Ge_{1-x}C_x$ electronic band structure calculated by hybrid functional DFT and TB/VFF calculations for small alloy supercells containing up to 128 atoms. Good quantitative agreement for the evolution of the alloy band gap enabled us to move to further analyze the structure of ordered and disordered alloys.

In our ordered calculations C incorporation leads to the formation of a state lying within the band gap of Ge with the CB minimum at the zone centre. However, our calculations suggest that this is a hybridised state formed from Ge host matrix states lying close to the band gap. The hybridisation

is driven by the large differences in the size and electronegativity of C and Ge. The C-related state is formed primarily by a mixture of two Ge states, the Ge Γ_{7c} CB edge state and the Ge L_{6c} state with A_1 (s-like) symmetry about the C atom site. As a result, we see a state with some direct gap like character; however, in the supercells we investigate the largest direct gap character was 18% while the indirect gap character made up the majority of the C-related state. Our work on ordered $Ge_{1-x}C_x$ supercells conflicts with the suggestion of a C-related localised state forming in the band gap that undergoes a BAC interaction with the extended Γ_{7c} zone centre CB edge states of Ge. In these supercells we showed that $Ge_{1-x}C_x$ retains primarily an indirect gap character which is in agreement with the DFT analysis of Kirwan et al. [41]; this was the case for 54, 64 and 128 atom unit cells. This indicates that the CB minimum state of $Ge_{1-x}C_x$ is not formed via the predicted BAC interaction and is instead primarily formed by the A_1-symmetric (s-like) L_{6c} CB edge states of Ge.

We next investigated the evolution of the CB minimum state of $Ge_{1-x}C_x$ as the composition in the ordered supercells approached the ultra-dilute limit. Here we showed that the Γ_{7c} character of the CB edge state decreased as it approached dilute compositions of x=0.001% with direct Γ character of just 1.12%. We also demonstrated that the localisation of the C state is only slightly stronger than the Gamma state of Ge, with a substantial part of the state spread out on other atoms. Pressure coefficient calculations demonstrated that in the ultra dilute limit the alloy possesses the same pressure coefficient as the Ge L state, 4.5 meV/kbar, while at higher compositions there is some increase in the pressure coefficient towards the Ge Γ pressure coefficient. However, the coefficient is still intermediate between that of the direct and indirect pressure coefficients, again in agreement with DFT calculations. These ordered calculations highlight firstly that the electronic structure of $Ge_{1-x}C_x$ cannot be described by a simple model such as the BAC and instead requires specific treatment of alloy effects, and secondly that a direct band gap does not form in $Ge_{1-x}C_x$ and instead it retains primarily indirect gap character.

In section 3.4 we next looked at how the disorder present in real materials affects the character of the C-related state. Alloy disorder leads to strong inhomogeneous broadening of the Bloch character associated with the CB edge states, due to a distribution of C-related localised states forming low within the band gap. On average the direct gap character tends to lie at higher energies than the indirect L character which conflicts with the assumptions of the BAC model whereby the CB edge states were predicted to obtain primarily direct gap character. Our analysis of large disordered alloy supercells also demonstrates strong sensitivity of the $Ge_{1-x}C_x$ electronic properties to the presence of short-range alloy disorder, behaviour typical of a highly-mismatched semiconductor alloy. Individually, these states only possess small direct (Ge $\Gamma_{2'c}$) character, and so will not support appreciable direct-gap optical recombination. Further analysis would be required to estimate the magnitude of the optical recombination rate associated with these localised states in a realistic, disordered $Ge_{1-x}C_x$ alloy. Owing to the small direct gap character we would expect a considerably lower radiative recombination rate in dilute $Ge_{1-x}C_x$ than would be found in a conventional direct-gap semiconductor.

In summary, rather than acquiring a direct band gap via a BAC interaction, our analysis demonstrates that the $Ge_{1-x}C_x$ CB edge attains minimal direct gap (Γ_{7c}) character. The C-induced band mixing identified by our calculations instead leads to the formation of a "quasi-direct" hybridised alloy band gap in the dilute C limit, which retains predominantly indirect gap (Ge L_{6c}) character, with a distribution of C localised states emerging within the Ge band gap in the presence of short-range alloy disorder. Based on our electronic structure analysis here, we similarly expect strong suppression of electron mobility in dilute $Ge_{1-x}C_x$ alloys. The identification in our disordered supercell calculations of strong inhomogeneous energetic broadening of the CB edge Bloch character reflects the presence of a distribution of localised states and indicates a breakdown of strict **k**-selection. On this basis, we expect many scattering pathways to open up for electrons in the $Ge_{1-x}C_x$ CB, so that the electron mobility in the alloy is both strongly and intrinsically limited. These general conclusions are in qualitative and quantitative agreement with those of recent analysis based on hybrid functional DFT calculations. We therefore conclude that C incorporation in Ge does not give rise to a direct-gap semiconductor alloy, limiting the benefit of this material system for applications in optoelectronic devices. We emphasise that the conclusions drawn above are based solely on the results of our analysis of the electronic structure of idealised $Ge_{1-x}C_x$ alloys – i.e. purely substitutional, defect-free alloys. The presence of defects – e.g. in the form of C interstitials due to non-substitutional incorporation – will likely exacerbate limitations on the optical and transport properties. Overall, while dilute $Ge_{1-x}C_x$ alloys are of interest from a fundamental perspective due to their unusual electronic properties, we conclude that they are likely to be of limited value for applications in CMOS-compatible optoelectronic devices.

6.3 Enhanced BTBT in $Ge_{1-x}Sn_x$ alloys

In this section we discuss the results of our analysis on the atomistic origin of enhanced BTBT in $Ge_{1-x}Sn_x$ alloys. Previous analysis of BTBT in $Ge_{1-x}Sn_x$ has centred on a single approach, comprising electronic structure calculations performed in the virtual crystal approximation (VCA) being used as input to semi-classical BTBT calculations based on the WKB approximation. This approach implicitly neglects atomistic effects, assuming that the indirect- to direct-gap transition occurs abruptly at a single, critical Sn composition. Recent DFT analysis has shown that this indirect to direct gap transition evolves continuously with increasing Sn content, characterised by alloy-induce band mixing between the Ge CB edge states, L_{6c} and Γ_{7c}. In order to analyze the atomistic origin of BTBT we required an atomistic framework; we therefore selected the tight binding model for electronic structure simulation and a valence force field potential for relaxation of the alloy supercells. To investigate BTBT our transport calculations were carried out using the NEGF solver OMEN specifically using the recursive Green's function algorithm. The role of two key atomistic effects on BTBT were of interest – Γ_{7c}-L_{6c} mixing leading to hybridisation of the CB edge states and local alloy disorder.

We began with analysis of the complex band structure of ordered alloy supercells, which demonstrated that Γ_{7c}-L_{6c} mixing drives an anti crossing of the complex bands originating from the CB

edge states, opening a route for a reduced tunneling path between the zone centre CB minimum and VB maximum states. This reduced tunneling path manifests as an enhanced generation rate in BTBT transport calculations leading to a BTBT generation rate increase of eight orders of magnitude for an ordered supercell with a composition of x = 6.25% at an applied electric field of 1 MV/cm. We explicitly quantified the role alloy band mixing effects play in the enhanced generation via parameterisation of a 3 band k.p Hamiltonian that specifically includes band mixing through a Γ_{7c}-L_{6c} mixing term. The resulting complex band structure has excellent quantitative agreement with alloy calculations obtained from atomistic TB supercell calculations. Using the k.p complex band structure with the WKB approximation in semi-classical BTBT calculations we were able to reproduce the generation rates of the alloy calculations with excellent agreement for both compositions, highlighting the central role of band mixing on the generation rate.

To quantify the impact of the second alloy effect under investigation – local alloy disorder, we set up realistic disordered alloy calculations to determine the evolution of the BTBT generation rate with composition. A loss of short range order resulted in a reduction of the complex band anti-crossing; however, the anti-crossing did persist in disordered calculations. This leads to an appreciable increase in the BTBT generation rate upon incorporation of small quantities of Sn. Comparison with similar calculations based on the VCA reveals that disordered alloy calculations exceed the generation rates of VCA calculations for a range of Sn compositions. In comparison with ordered calculations, the impact of disorder was limited at low Sn compositions with minimal difference between the ordered and disordered generation rates. At higher Sn compositions the disordered-alloy BTBT generation rate is reduced compared to that obtained from ordered alloy supercell calculations, due to a "washing out" of the strength of alloy-induced hybridisation resulting from a loss of lattice translational symmetry. Calculations using a VCA Hamiltonian parameterised to match the experimentally measured alloy band gap bowing still failed to match the increase in the generation rate for compositions below the conventional indirect to direct gap transition, highlighting that the omission of atomistic effects precludes a quantitative understanding of the alloy electrical properties.

The results of chapter 4 highlight the key role atomistic alloy effects play in the electrical properties of $Ge_{1-x}Sn_x$ alloys: calculations based on an atomistic framework show that inclusion of these effects leads to a significant increase in the BTBT tunneling generation rate when compared to a conventional VCA based approach. We conclude that the impact of Sn incorporation on the CB structure of $Ge_{1-x}Sn_x$ alloys can then allow for higher on-state currents in $Ge_{1-x}Sn_x$-based TFETs than previously predicted.

6.4 $Ge_{1-x}Sn_x$ TFETs

In chapter 5 we investigated the impact of atomistic alloy effects on the current characteristics of $Ge_{1-x}Sn_x$ TFETs. Our theoretical analysis was again based on an atomistic framework consisting of atomic relaxation using a valence force field potential and electronic band structure modelling

using the tight-binding method. Transport calculations were carried out using OMEN to solve the coupled Schrödinger-Poisson equations. This enabled detailed calculations to determine the impact of the previously ignored atomistic effects in $Ge_{1-x}Sn_x$ TFETs. In chapter 4 alloy effects were found to lead to an enhanced generation rate in bulk $Ge_{1-x}Sn_x$ alloy supercells, which we expected to increase I_{on} for $Ge_{1-x}Sn_x$ based TFETs. Using our theoretical framework we analysed the current characteristics of two $Ge_{1-x}Sn_x$ TFET designs, a double gate ultra thin body (DGUTB) TFET and a gate all around (GAA) TFET.

For the DGUTB TFET there was a large increase in I_{on} compared with Ge. For an ordered alloy TFET we see an increase of eight orders of magnitude in I_{on} for a composition of 6.25% while for a lower composition of 1.5625% there is an increase of more than two orders of magnitude compared to Ge. Comparisons with a VCA based model reveal I_{on} for the alloy composition of 1.5625% is an order of magnitude greater than a corresponding VCA based calculation, demonstrating the inability of VCA based calculations to reproduce I_{on} from alloy calculations due to the tendency of the VCA to overestimate the band gap. Disordered calculations show an increase of seven orders of magnitude in I_{on} over a composition range of 0-10% Sn. In these calculations there is a rapid increase in I_{on} for small Sn compositions up to 4% Sn, after which the rate of increase in I_{on} reduces considerably. Comparing ordered and disordered calculations shows that disorder tends to reduce I_{on} for the $Ge_{1-x}Sn_x$ TFETs compared to ordered TFETs; however, I_{on} remains larger than in similar VCA-based calculations. Throughout these calculations our IV curves have low sub-threshold swing values in the range of 10-20 mV/decade, below the target 60 mV/decade threshold. This is primarily due to the lack of inclusion of other tunneling processes such as trap assisted tunneling which can dramatically increase I_{off}[64], but have little effect on I_{on}. Therefore our SS values represent the best possible targets for $Ge_{1-x}Sn_x$ TFETs that could be reached with improved growth processes.

For the GAA TFET, there were similar results with a marked increase in I_{on} for ordered $Ge_{1-x}Sn_x$ TFETs that were greater than VCA calculations at the same compositions. For an ordered composition of 6.25% we saw an increase of more than two orders of magnitude over Ge and more than an order of magnitude over a x = 6.25% VCA calculation. Disorder again serves to reduce some the of the band mixing effects; however, I_{on} remains above that from similar VCA calculations.

In summary our investigation of the impact of atomistic effects on the current characteristics of $Ge_{1-x}Sn_x$ based TFETs revealed an increase in I_{on} when compared with the frequently used VCA framework, demonstrating that the atomistic effects that lead to an enhanced generation rate in chapter 4 have been transferred to an increase in on currents in $Ge_{1-x}Sn_x$ TFETs. Disorder serves to reduce some of the enhancement due to band mixing and alloy band gap reduction. However, the I_{on} values remain elevated above those calculated using the VCA for both TFET devices examined here, due to the larger band gaps of the VCA. These results further build on earlier theoretical predictions of attractive performance of $Ge_{1-x}Sn_x$ based TFETs for post CMOS computing. Further research will be required to combine our atomistic alloy calculations with loss processes such as trap-assisted tunneling (TAT), in order to improve predictions of current $Ge_{1-x}Sn_x$ TFETs designs.

6.5 Outlook for $Ge_{1-x}Sn_x$ alloys

Overall, our analysis highlights that previously overlooked atomistic effects play an important role in governing the electrical properties of $Ge_{1-x}Sn_x$ alloys, and that inclusion of these effects in BTBT calculations predicts an enhancement in BTBT generation rate compared to initial theoretical predictions. We conclude that the impact of Sn incorporation on the CB structure of $Ge_{1-x}Sn_x$ alloys can then allow for higher on-state currents in $Ge_{1-x}Sn_x$-based TFETs than previously predicted. This, combined with the ability to tune the band gap via Sn composition and nanostructuring, provides broad scope to engineer performance and obtain competitive characteristics from CMOS-compatible TFETs.

Future work that would be a continuation of the calculations performed here would be to determine the role if any of phonon-based transmission in $Ge_{1-x}Sn_x$ structures. This pathway was neglected in the current work, due to the dominance of coherent transmission when a direct tunneling path emerges, but we did not confirm the validity of this assumption due to the expensive nature of calculations that include phonon effects. Another area for improved theoretical predictions would be the inclusion of processes that result in increased tunneling in the off state such as trap assisted tunneling, this would enable comparison with existing experimental calculations for the subthreshold swing.

Bibliography

[1] Z. Zhou, B. Yin, and J. Michel, "On-chip light sources for silicon photonics," Light: Science & Applications **4**, e358 (2015).

[2] S. Saito, A. Z. Al-Attili, K. Oda, and Y. Ishikawa, "Towards monolithic integration of germanium light sources on silicon chips," Semicond. Sci. Technol. **31**, 043002 (2016).

[3] D. Thomson, A. Zilkie, J. E. Bowers, T. Komljenovic, G. T. Reed, L. Vivien, D. Marris-Morini, E. Cassan, L. Virot, J.-M. Fédéli, et al., "Roadmap on silicon photonics," J. Opt. **18**, 073003 (2016).

[4] M. Yamaguchi, T. Takamoto, K. Araki, and N. J. Ekins-Daukes, "Multi-junction III–V solar cells: current status and future potential," Solar Energy **79**, 78 (2005).

[5] M. Yamaguchi, K.-I. Nishimura, T. Sasaki, H. Suzuki, K. Arafune, N. Kojima, Y. Ohsita, Y. Okada, A. Yamamoto, T. Takamoto, et al., "Novel materials for high-efficiency III–V multi-junction solar cells," Solar Energy **82**, 173 (2008).

[6] R. Roucka, A. Clark, T. Wilson, T. Thomas, M. Führer, N. J. Ekins-Daukes, A. Johnson, R. Hoffman, and D. Begarney, "Demonstrating dilute-tin alloy SiGeSn for use in multijunction photovoltaics: single- and multijunction solar cells with a 1.0-eV SiGeSn junction," IEEE J. Photovolt. **6**, 1025 (2016).

[7] I. L. Markov, "Limits on fundamental limits to computation," Nature **512**, 147 (2014).

[8] S. Salahuddin, K. Ni, and S. Datta, "The era of hyper-scaling in electronics," Nature Electronics **1**, 442 (2018).

[9] G. E. Moore, "Progress in digital integrated electronics," IEEE Int. Electron. Devices Meet. Tech. Dig. p. 102 (1975).

[10] W. M. Holt, "Moore's law: a path going forward," IEEE International Solid-State Circuits Conference (ISSCC) p. 8 (2016).

[11] J. M. Shalf, "The future of computing beyond Moore's law," Phil. Trans. R. Soc. A **378**, 20190061 (2020).

[12] A. M. Ionescu and H. Riel, "Tunnel field-effect transistors as energy-efficient electronic switches," Nature **479**, 329 (2011).

[13] A. Schenk, "Rigorous theory and simplified model of the band-to-band tunneling in silicon," Solid State Electron. **36**, 19 (1993).

[14] K.-H. Kao, A. S. Verhulst, W. G. Vendenberghe, B. Sorée, G. Groeseneken, and K. De Meyer, "Direct and indirect band-to-band tunneling in germanium-based TFETs," IEEE Trans. Electron. Devices **59**, 292 (2012).

[15] S. Jin, H. Parl, M. Luisier, W. Choi, J. Kim, and K. Lee, "Band to band tunneling in SiGe: influence of alloy scattering," IEEE Electron Device Lett. **38**, 422 (2017).

[16] R. Geiger, T. Zabel, and H. Sigg, "Group IV direct gap photonics: methods, challenges, and opportunities," Front. Mater. **2**, 52 (2015).

[17] V. Reboud, A. Gassenq, J. M. Hartmann, J. Widiez, L. Virot, J. Aubin, K. Guilloy, S. Tardif, J. M. Fédéli, N. Pauc, et al., "Germanium based photonic components toward a full silicon/germanium photonic platform," Prog. Cryst. Growth & Charact. **63**, 1 (2017).

[18] F. Zhang, V. H. Crespi, and P. Zhang, "Prediction that uniaxial tension along $\langle 111 \rangle$ produces a direct band gap in germanium," Phys. Rev. Lett. **102**, 156401 (2009).

[19] M. E. Kurdia, H. Bertin, E. Martincic, M. de Kersauson, G. Fishman, S. Sauvage, A. Bosseboeuf, and P. Boucauda, "Control of direct band gap emission of bulk germanium by mechanical tensile strain," Appl. Phys. Lett. **96**, 041909 (2010).

[20] J. R. Sánchez-Pérez, C. Boztug, F. Chen, F. F. Sudradjat, D. M. Paskiewicz, R. B. Jacobson, M. G. Lagally, and R. Paiella, "Direct-bandgap light-emitting germanium in tensilely strained nanomembranes," Proc. Natl. Acad. Sci. U.S.A. **108**, 18893 (2011).

[21] M. J. Süess, R. Geiger, R. A. Minamisawa, G. Schiefler, J. Frigerio, D. Chrastina, G. Isella, R. Spolenak, J. Faist, and H. Sigg, "Analysis of enhanced light emission from highly strained germanium microbridges," Nature Photonics **7**, 466 (2013).

[22] M. V. Fischetti and S. E. Laux, "Band structure, deformation potentials, and carrier mobility in strained Si, Ge, and SiGe alloys," J. Appl. Phys. **80**, 2234 (1996).

[23] J. Liu, X. Sun, D. Pan, X. Wang, L. Kimerling, T. Koch, and J. Michel, "Tensile-strained, n-type Ge as a gain medium for monolithic laser integration on Si.," Optical Express **15**, 11272 (2007).

[24] P. H. Lim, S. Park, Y. Ishikawa, and K. Wada, "Enhanced direct bandgap emission in germanium by micromechanical strain engineering," Optical Express **17**, 1635817 (2009).

[25] M. E. Kurdi, G. Fishman, S. Sauvage, and P. Boucaud, "Band structure and optical gain of tensile-strained germanium based on a 30 band k·p formalism," J. Appl. Phys. **107**, 013710 (2010).

[26] G. Pizzi, M. Virgilio, and G. Grosso, "Tight-binding calculation of optical gain in tensile strained [001]-Ge/SiGe quantum wells," Nanotechnology **21**, 055202 (2009).

[27] J. Kouvetakis, J. Menendez, and A. V. G. Chizmeshya, "Tin-based group IV semiconductors: new platforms for opto- and microelectronics on silicon," Annu. Rev. Mater. Res. **36**, 497 (2006).

[28] P. Moontragoon, Z. Ikonić, and P. Harrison, "Band structure calculations of si-ge-sn alloys: achieving direct band gap materials," Semicond. Sci. Technol. **22**, 742 (2007).

[29] R. Soref, "Silicon-based silicon-germanium-tin heterostructure photonics," Phil. Trans. R. Soc. A **372**, 0113 (2014).

[30] S. Zaima, O. Nakatsuka, N. Taoka, M. Kurosawa, W. Takeuchi, and M. Sakashita, "Growth and applications of GeSn-related group-IV semiconductor materials," Sci. Technol. Adv. Mater. **16**, 043502 (2015).

[31] S. Wirths, R. Geiger, N. von den Driesch, G. Mussler, T. Stoica, S. Mantl, Z. Ikonic, M. Luysberg, S. Chiussi, J. M. Hartmann, et al., "Lasing in direct-bandgap GeSn alloy grown on Si," Nat. Photonics **9**, 88 (2015).

[32] J. Margetis, Y. Zhou, W. Dou, P. C. Grant, B. Alharthi, et al., "All group-IV SiGeSn/GeSn/SiGeSn QW laser on Si operating up to 90·K," Appl. Phys. Lett. **113**, 221104 (2018).

[33] W. Huang, B. Cheng, C. Xue, and C. Li, "Comparative studies of clustering effect, electronic and optical properties of GePb and GeSn alloys with low Pb and Sn concentration," Physica B **443**, 43 (2014).

[34] W. Huang, B. Cheng, C. Xue, and H. Yang, "The band structure and optical gain of a new IV-group alloy GePb: a first principles calculation," J. Alloy Compd. **701**, 816 (2017).

[35] H. Alahmad, A. Mosleh, M. Alher, S. Fahimeh, Banihashemian, S. A. Ghetmiri, S. Al-Kabi, W. Du, B. Li, S.-Q. Yu, et al., "GePb alloy growth using layer inversion method," J. Electron. Mater. **47**, 3733 (2018).

[36] X. Liu, J. Zheng, L. Zhou, Z. Liu, Y. Zuo, C. Xueab, and B. Cheng, "Growth of single crystalline GePb film on Ge substrate by magnetron sputtering epitaxy," J. Alloy Compd. **785**, 228 (2019).

[37] C. A. Broderick, E. J. O'Halloran, and E. P. O'Reilly, "First principles analysis of electronic structure evolution and the indirect- to direct-gap transition in $Ge_{1-x}Pb_x$ group-IV alloys," `arXiv:1911.05679` (2019).

[38] C. A. Stephenson, W. A. O'Brien, M. W. Penninger, W. F. Schneider, M. Gillett-Kunnath, J. Zajicek, K. M. Yu, R. Kudraweic, R. A. Stillwell, and M. A. Wistey, "Band structure of germanium carbides for direct bandgap silicon photonics," J. Appl. Phys. **120**, 053102 (2016).

[39] C. A. Stephenson, W. A. O'Brien, M. Qi, M. W. Penninger, W. F. Schneider, and M. A. Wistey, "Band anticrossing in dilute germanium carbides using hybrid density functionals," J. Electron. Mater. **45**, 2121 (2016).

[40] C. A. Broderick, M. D. Dunne, D. S. P. Tanner, A. C. Kirwan, E. J. O'Halloran, S. Schulz, and E. P. O'Reilly, "Atomistic analysis of localisation and band mixing effects in $Ge_{1-x}(C,Sn)_x$ group-IV alloys," Proc. IEEE Conference on Nanotechnology (IEEE NANO) (2018).

[41] A. C. Kirwan, S. Schulz, and E. P. O'Reilly, "Nature of the band gap of Ge:C alloys: insights from hybrid functional density functional theory," Semicond. Sci. Technol. **34**, 075007 (2019).

[42] H. J. Osten, B. Dietrich, H. Rücker, and M. Methfessel, "Local structure of strain-compensated epitaxial $Si_{1-x-y}Ge_xC_y$ layers on Si(001) grown with molecular beam epitaxy," J. Cryst. Growth **150**, 931 (1995).

[43] S. C. Jain, H. J. Osten, B. Dietrich, and H. Rücker, "Growth and properties of strained $Si_{1-x-y}Ge_xC_y$ layers," Semicond. Sci. Technol. **10**, 1289 (1995).

[44] E. Finkman, F. Meyer, and M. Mamor, "Short-range order and strain in SiGeC alloys probed by phonons," J. Appl. Phys. **89**, 2580 (2001).

[45] H. Rücker, M. Methfessel, B. Dietrich, K. Pressel, and H. J. Osten, "Phonons as a probe of short-range order in $Si_{1-x}C_x$ alloys," Phys. Rev. B **53**, 1302 (1996).

[46] M. P. Vaughan, F. Murphy-Armando, and S. Fahy, "First principles investigation of the alloy scattering potential in dilute $Si_{1-x}C_x$," Phys. Rev. B **85**, 165209 (2012).

[47] M. Okinaka, K. Miyatake, J. Ohta, and M. Nunoshita, "Large band gap bowing of MBE-grown GeC/Si(001) layers," J. Cryst. Growth **255**, 273 (2003).

[48] K. J. Roe, M. W. Dashiell, J. Kolodzey, P. Bouchaud, and J.-M. Lourtioz, "Molecular beam epitaxy growth of $Ge_{1-y}C_y$ alloys on Si (001) with high carbon contents," J. Vac. Sci. Technol. B **17**, 1302 (1999).

[49] J. Kolodzey, P. R. Berger, B. A. Orner, D. Hits, F. Chen, A. Khan, X. Shao, M. M. Waite, S. I. Shah, C. P. Swann, et al., "Optical and electronic properties of SiGeC alloys grown on Si substrates," J. Cryst. Growth **157**, 386 (1995).

[50] D. Gall, J. D'Arcy-Gall, and J. E. Greene, "C incorporation in epitaxial $Ge_{1-y}C_y$ layers grown on Ge(001): an ab initio study," Phys. Rev. B **62**, R7723(R) (2000).

[51] S. Y. Park, J. D'Arcy-Gall, D. Gall, Y.-W. Kim, P. Desjardins, and J. E. Greene, "C lattice site distributions in metastable $Ge_{1-y}C_y$ alloys grown on Ge(001) by molecular beam epitaxy," J. Appl. Phys. **91**, 3644 (2002).

[52] C. A. Stephenson, M. Gillett-Kunnath, W. A. O'Brien, R. Kudraweic, and M. A. Wistey, "Gas source techniques for molecular beam epitaxy of highly-mismatched Ge alloys," Crystals **6**, 159 (2016).

[53] W. Shan, W. Walukiewicz, J. W. A. III, E. E. Haller, J. F. Geisz, D. J. Friedman, J. M. Olson, and S. R. Kurtz, "Band anticrossing in GaInNAs alloys," Phys. Rev. Lett. **82**, 1221 (1999).

[54] J. Wu, W. Shan, and W. Walukiewicz, "Band anticrossing in highly mismatched III-V semiconductor alloys," Semicond. Sci. Technol. **17**, 860 (2002).

[55] J. Wu, W. Walukiewicz, K. M. Yu, J. W. A. III, E. E. Haller, I. Miotkowski, A. K. Ramdas, C.-H. Su, I. K. Sou, R. C. C. Perera, et al., "Origin of the large band-gap bowing in highly mismatched semiconductor alloys," Phys. Rev. B **67**, 035207 (2003).

[56] E. P. O'Reilly, A. Lindsay, P. J. Klar, A. Polimeni, and M. Capizzi, "Trends in the electronic structure of dilute nitride alloys," Semicond. Sci. Technol. **24**, 033001 (2009).

[57] K. A. Mader, A. Baldereschi, and H. von Kanel, "Band structure and instability of $Ge_{1-x}Sn_x$ alloys," Solid State Commun. **69**, 1123 (1989).

[58] Y. Yang, S. Su, P. Guo, W. Wang, X. Gong, L. Wang, K. L. Low, G. Zhang, C. Xue, B. Cheng, et al., "Towards direct band-to-band tunneling in p-channel tunneling field effect transistor (TFET): technology enablement by germanium-tin (GeSn)," Proc. IEEE Int. Electron. Dev. Meet. (IEDM) (2012).

[59] G. Han, Y. Wang, Y. Liu, H. Wang, M. Liu, C. Zhang, B. CHeng, and Y. Hao, "Relaxed germanium-tin P-channel tunneling field-effect transistors fabricated on Si: impacts of Sn composition and uniaxial tensile strain," AIP Advances **5**, 057145 (2015).

[60] J. Schulze, A. Blech, A. Datta, I. A. Fischer, D. Hähnel, S. Naasz, E. Rolseth, and E. M. Tropper, "Vertical Ge and GeSn heterojunction gate-all-around tunneling field effect transistors," Solid-State Electronics **110**, 59 (2015).

[61] E. G. Rolseth, A. Blech, I. A. Fischer, Y. Hashad, R. Koerner, K. Kostecki, A. Kruglov, V. S. S. Srinivasan, M. Weiser, T. Wendav, et al., "Device performance tuning of Ge gate-all-around tunneling field effect transistors by means of GeSn: Potential and challenges," Proc. IEEE Int. Inform. Comm. Tech. Elec. Micro. (MIPRO) pp. 54–65 (2017).

[62] D. Haehnel, I. A. Fischer, A. Hornung, A. C. Koellner, and J. Schulze, "Tuning the Ge(Sn) Tunneling FET: Influence of Drain Doping, Short Channel, and Sn Content," IEEE Trans. Electron. Devices **62**, 36 (2015).

[63] Y. Yang, G. Han, P. Guo, W. Wang, X. Gong, L. Wang, K. L. Low, and Y.-C. Yeo, "Germanium–tin p-channel tunneling field-effect transistor: device design and technology demonstration," IEEE Trans. Electron. Devices **60**, 4048 (2013).

[64] C. Schulte-Braucks, R. Pandey, R. N. Sajjad, M. Barth, R. K. Ghosh, B. Grisafe, P. Sharma, N. von den Driesch, A. Vohra, G. B. Rayner, et al., "Fabrication, characterization, and analysis of Ge/GeSn heterojunction p-type tunnel transistors," IEEE Trans. Electron. Devices **64**, 4354 (2017).

[65] A. Attiaoui and O. Moutanabbir, "Indirect-to-direct band gap transition in relaxed and strained $Ge_{1-x-y}Si_xSn_y$ ternary alloys," J. Appl. Phys. **116**, 063712 (2014).

[66] K. L. Low, Y. Yang, G. Han, W. Fan, and Y. C. Yeo, "Electronic band structure and effective mass parameters of $Ge_{1-x}Sn_x$ alloys," J. Appl. Phys **112**, 103715 (2012).

[67] B. Dutt, H. Lin, S. D. Sukhdeo, B. M. Vulovic, S. Gupta, D. Nam, C. K. Saraswat, and S. J. Harris, "Theoretical analysis of GeSn alloys as a gain medium for a Si-compatible laser," IEEE J. Sel. Topics Quantum Electron. **19**, 1502706 (2013).

[68] E. J. O'Halloran, C. A. Broderick, D. S. P. Tanner, S. Schulz, and E. P. O'Reilly, "Comparison of first principles and semi-empirical models of the structural and electronic properties of $Ge_{1-x}Sn_x$ alloys," Opt. Quantum Electron. **51**, 314 (2019).

[69] T. D. Eales, I. P. Marko, S. Schulz, E. J. O'Halloran, S. Ghetmiri, W. Du, Y. Zhou, S.-Q. Yu, J. Margetis, J. Tolle, et al., "$Ge_{1-x}Sn_x$ alloys: consequences of band mixing effects for the evolution of the band gap Γ character with Sn concentration," Sci. Rep. **9**, 14077 (2019).

[70] M. P. Polak, P. Scharoch, and R. Kudrawiec, "The effect of isovalent doping on the electronic band structure of group-IV semiconductors ," J. Phys. D: Appl. Phys **54**, 085102 (2021).

[71] I. A. Gulyas, C. A. Stephenson, Q. Meng, S. R. Bank, and M. A. Wistey, "The carbon state in dilute germanium carbides," Journal of Applied Physics **129**, 055701 (2021).

[72] M. Luisier, A. Schenk, and W. Fichtner, "Atomistic simulation of nanowires in the $sp^3d^5s^*$ tight-binding formalism: from boundary conditions to strain calculations," Phys. Rev. B **74**, 205323 (2006).

[73] Y. Yang, K. L. Low, W. Wang, P. Guo, L. Wang, G. Hana, and Y. C.Yeo, "Germanium-tin n-channel tunneling field-effect transistor: Device physics and simulation study," J. Appl. Phys. **113**, 194507 (2013).

[74] S. Sant and A. Schenk, "Pseudopotential calculations of strained GeSn/SiGeSn hetero-structures," Appl. Phys. Lett. **105**, 162101 (2014).

[75] S. Sant and A. Schenk, "Band-offset engineering for GeSn-SiGeSn hetero tunnel FETs and the role of strain," IEEE J. Electron. Devices Soc. **3**, 164 (2015).

[76] M. Liu, Y. Liu, H. Wang, Q. Zhang, C. Zhang, S. Hu, Y. Hao, and G. Han, "Design of GeSn-based heterojunction-enhanced n-channel tunneling FET with improved subthreshold swing and on-state current," IEEE Trans. Electron. Devices **62**, 1262 (2015).

[77] H. Wang, G. Han, Y. Liu, S. Hu, C. Zhang, J. Zhang, and Y. Hao, "Theoretical investigation of performance enhancement in GeSn/SiGeSn type-II staggered heterojunction tunneling FET," IEEE Trans. Electron. Devices **63**, 303 (2016).

[78] L. Liu, R. Liang, J. Wang, and J. Xu, "Enhanced performance of GeSn source-pocket tunnel field-effect transistors for low-power applications," Jpn. J. Appl. Phys. **55**, 071201 (2016).

[79] H. Wang, G. Han, Y. Wang, Y. Peng, Y. Liu, C. Zhang, J. Zhang, S. Hu, and Y. Hao, "Theoretical calculation of performance enhancement in lattice-matched SiGeSn/GeSn p-channel tunneling field-effect transistor with type-II staggered tunneling junction," Jpn. J. Appl. Phys. **55**, 04ED13 (2016).

[80] H. Wang, Y. Liu, G. Han, Y. Shao, C. Zhang, Q. Feng, J. Zhang, and Y. Hao, "Performance enhancement in uniaxially strained germanium–tin FinTFET: fin direction dependence," IEEE Trans. Electron. Devices **64**, 2804 (2017).

[81] H. Wang, G. Han, Y. Liu, J. Zhang, Y. Hao, and X. Jiang, "The performance improvement in SiGeSn/GeSn p-channel hetero line tunneling FET (HL-TFET)," Proc. IEEE Electrical Design of Advanced Packaging and Systems Symposium (EDAPS) (2017).

[82] S. Wang, J. Zheng, C. Xue, C. Li, Y. Zuo, B. Cheng, and Q. Wang, "Device simulation of GeSn/GeSiSn pocket n-type tunnel field-effect transistor for analog and RF applications," Superlattices Microstruct. **111**, 286 (2017).

[83] K. Kumar, Y. Hsieh, J. Liao, K. Kao, and Y. Wang, "Significance of multivalley and non-parabolic band structure for GeSn TFET simulation," IEEE Trans. Electron. Devices **65**, 10 (2018).

[84] X. Liu, H. Hu, M. Wang, Y. Miao, G. Han, and B. Wang, "Design and theoretical calculation of novel GeSn fully-depleted n-tunneling FET with quantum confinement model for suppression on GIDL effect," Superlattices Microstruct. **118**, 266 (2018).

[85] S. Wang, Q. Wu, J. Zheng, B. Zhang, J. Yao, Q. Zhou, L. Yang, J. Xu, and B. Cheng, "GeSn/GeSiSn double-heterojunction short channel tunnel field-effect transistor design," Jpn. J. Appl. Phys. **59**, 034001 (2020).

[86] G. He and H. A. Atwater, "Interband transitions in Sn_xGe_{1-x} alloys," Phys. Rev. Lett. **79**, 1937 (1997).

[87] J. Doherty, S. Biswas, E. Galluccio, C. A. Broderick, A. Garcia-Gil, R. Duffy, E. P. O'Reilly, and J. D. Holmes, "Progress on germanium–tin nanoscale alloys," Chem. Mater. **32**, 4383 (2020).

[88] O. Moutanabbir, S. Assali, X. Gong, E. P. O'Reilly, C. A. Broderick, B. Marzban, J. Witzens, W. Du, S.-Q. Yu, A. Chelnokov, et al., "Monolithic infrared silicon photonics: the rise of (Si)GeSn semiconductors," Appl. Phys. Lett. **118**, 110502 (2021).

[89] N. W. Ashcroft and N. D. Mermin, "Solid state Phyiscs," Holt Rinehart and Winston (1976).

[90] W. A. Harrison, "Bond-orbital model and the properties of tetrahedrally coordinated solids," Phys. Rev. B **8**, 4487 (1973).

[91] D. J. Chadi and M. L. Cohen, "Tight-binding calculations of the valence bands of diamond and zincblende crystals," Phys. Stat. Sol. B **68**, 405 (1975).

[92] P. Vogl, H. P. Hjalmarson, and J. D. Dow, "A semi-empirical tight-binding theory of the electronic structure of semiconductors," J. Phys. Chem. Solids **44**, 365 (1983).

[93] P. Yu and M. Cardonna, "Fundamentals of Semiconductors," Springer (2010).

[94] P.-O. Löwdin, "On the nonorthogonality problem connected with the use of atomic wave functions in the theory of molecules and crystals," J. Phys. Chem. **18**, 365 (1950).

[95] W. A. Harrison, "Electronic Structure and the Properties of Solids: The Physics of the Chemical Bond," Dover (1989).

[96] P. Vogl, H. P. Hjalmarson, and J. D. Dow, "A semi-empirical tight-binding theory of the electronic structure of semiconductors," J. Phys. Chem. Solids **44**, 365 (1983).

[97] J. C. Slater and G. F. Koster, "Simplified LCAO method for the periodic potential problem," Phys. Rev. **94**, 1498 (1954).

[98] D. J. Chadi, "Spin-orbit splitting in crystalline and compositionally disordered semiconductors," Phys. Rev. B **16**, 790 (1977).

[99] V. Popescu and A. Zunger, "Extracting E versus k effective band structure from supercell calculations on alloys and impurities," Phys. Rev. Lett. **85**, 085201 (2012).

[100] P. N. Keating, "Effect of invariance requirements on the elastic strain energy of crystals with application to the diamond structure," Phys. Rev. **145**, 637 (1966).

[101] O. L. Lazarenkova, P. von Allmen, F. Oyafuso, S. Lee, and G. Klimeck, "Effect of anharmonicity of the strain energy on band offsets in semiconductor nanostructures," Appl. Phys. Lett. **85**, 4193 (2004).

[102] M. J. P. Musgrave and J. A. Pople, "A general valence force field for diamond," Proc. R. Soc. Lond. A **268**, 474 (1962).

[103] R. M. Martin, "Elastic properties of ZnS structure semiconductors," Phys. Rev. B **1**, 4005 (1970).

[104] D. S. P. Tanner, C. A. Broderick, A. C. Kirwan, S. Schulz, and E. P. O'Reilly, "Elastic properties of elemental, compound, and alloyed group-IV materials: hybrid density functional theory and valence force field parametrisation," (2019).

[105] J. D. Gale, "GULP - a computer program for the symmetry adapted simulation of solids," JCS Faraday Trans. **93**, 629 (1997).

[106] J. D. Gale and A. L. Rohl, "The General Utility Lattice Program," Mol. Simul. **29**, 291 (2003).

[107] J. D. Gale, "GULP: Capabilities and prospects," Z. Krist. **220**, 552 (2005).

[108] S. Plimpton, "Fast parallel algorithms for short-range molecular dynamics," J. Comput. Phys. **117**, 1 (1995).

[109] A. P. Thompson, H. Metin Aktulga, R. Berger, D. S. Bolintineanu, W. M. Brown, P. S. Crozier, P. J. in 't Veld, A. Kohlmeyer, S. G. Moore, T. D. Nguyen, et al., "LAMMPS - a flexible simulation tool for particle-based materials modeling at the atomic, meso, and continuum scales," Comput. Phys. Commun. **271**, 108171 (2022).

[110] T. B. Boykin, G. Klimeck, R. C. Bowen, and F. Oyafuso, "Diagonal parameter shifts due to nearest-neighbor displacements in empirical tight-binding theory," Phys. Rev. B **66**, 125207 (2002).

[111] J.-M. Jancu and P. Voisin, "Tetragonal and trigonal deformations in zinc-blende semiconductors: A tight-binding point of view," Phys. Rev. B **76**, 115202 (2007).

[112] T. B. Boykin, M. Luisier, M. Salmani-Jelodar, and G. Klimeck, "Strain-induced, offdiagonal, same-atom parameters in empirical tight-binding theory suitable for [110] uniaxial strain applied to a silicon parametrization," Phys. Rev. B Phys. Rev. B **81**, 125202 (2010).

[113] A. Lindsay, " Ph.D. thesis," University of Surrey, England (2002).

[114] Y. C. Chang and J. N. Schulman, "Complex band structures of crystalline solids: an eigenvalue method," Phys. Rev. B **25**, 3975 (1982).

[115] M. Städele, B. R. Tuttle, and K. Hess, "Tunneling through ultrathin SiO2 gate oxides from microscopic models," J. Appl. Phys. **89**, 348 (2001).

[116] C. Rivas and R. Lake, "Non-equilibrium Green function implementation of boundary conditions for full band simulations of substrate-nanowire structures," Phys. Status Solidi B **239**, 94 (2003).

[117] S. Datta, "Electronic Transport in Mesoscopic Systems," Cambridge University Press (1995).

[118] R. Lake, G. Klimeck, and R. C. Bowen, "Single and multiband modeling of quantum electron transport through layered semiconductor devices," J. Appl. Phys. **81**, 7845 (1997).

[119] G. Grosso, S. Moroni, and G. P. Parravicini, "Electronic structure of the InAs-GaSb superlattice studied by the renormalization method," Physical Review B **40**, 12328 (1989).

[120] T. B. Boykin, J. P. A. van der Wagt, and J. S. Harris, "Tight-binding model for GaAs/AlAs resonant-tunneling diodes," Jr, Phys. Rev. B **43**, 4777 (1991).

[121] D. Z.-Y. Ting, E. T. Yu, and T. C. McGil, "Multiband treatment of quantum transport in interband tunnel devices," Phys. Rev. B **45**, 3583 (1992).

[122] M. Luisier, A. Schenk, W. Fichtner, and G. Klimeck, "Atomistic simulation of nanowires in the $sp^3d^5s^*$ tight-binding formalism: From boundary conditions to strain calculations," Phys. Rev. B **74**, 205323 (2006).

[123] T. B. Boykin, "Tunneling calculations for systems with singular coupling matrices: Results for a simple model," Phys. Rev. B **54**, 7670 (1996).

[124] T. B. Boykin, M. Luisier, and G. Klimeck, "Multiband transmission calculations for nanowires using an optimized renormalization method," Phys. Rev. B **77**, 165318 (2008).

[125] G. Grosso, S. Moroni, and G. P. Parravicini, "Electronic structure of the InAs-GaSb superlattice studied by the renormalization method," Phys. Rev. B **40**, 12328 (1989).

[126] D. S. P. Tanner, Ph.D. thesis, University College Cork, Ireland (2017), URL http://cora.ucc.ie/handle/10468/5459.

[127] C. A. Broderick, A. C. Kirwan, S. Schulz, and E. P. O'Reilly, "Electronic properties of elemental and compound group-IV materials: hybrid density functional theory and tight-binding parametrisation," (2019).

[128] E. P. O'Reilly and A. Lindsay, "Tight-binding approach to calculation of localised perturbations in semiconductors," J. Phys. Conf. Ser. **242**, 012002 (2010).

[129] M. S. Dresselhaus, G. Dresselhaus, and A. Jorio, "Group Theory: Application to the Physics of Condensed Matter" (Springer, 2008).

[130] J.-M. Jancu, R. Scholz, F. Beltram, and F. Bassani, "Empirical *spds** tight-binding calculation for cubic semiconductors: general method and material parameters," Phys. Rev. B **57**, 6493 (1998).

[131] A. Lindsay and E. P. O'Reilly, "Theory of enhanced bandgap non-parabolicity in GaN_xAs_{1-x} and related alloys," Solid State Commun. **112**, 443 (1999).

[132] E. P. O'Reilly, A. Lindsay, S. Tomić, and M. Kamal-Saadi, "Tight-binding and $\mathbf{k}\cdot\mathbf{p}$ models for the electronic structure of Ga(In)NAs and related alloys," Semicond. Sci. Technol. **17**, 870 (2002).

[133] A. Lindsay and E. P. O'Reilly, "Unification of the band anticrossing and cluster-state models of dilute nitride semiconductor alloys," Phys. Rev. Lett. **93**, 196402 (2004).

[134] A. Lindsay and E. P. O'Reilly, "Theory of conduction band dispersion in dilute $B_xGa_{1-x}As$ alloys," Phys. Rev. B **76**, 075210 (2007).

[135] A. Lindsay and E. P. O'Reilly, "Theory of electronic structure of BGaAs and related alloys," Phys. Status Solidi C **5**, 454 (2008).

[136] T. Sander, J. Teubert, P. J. Klar, A. Lindsay, and E. P. O'Reilly, "Effect of localized boron impurities on the line shape of the fundamental band gap transition in photomodulated reflectance spectra of (B,Ga,In)As," Phys. Rev.B **83**, 235213 (2011).

[137] M. Usman, C. A. Broderick, A. Lindsay, and E. P. O'Reilly, "Tight-binding analysis of the electronic structure of dilute bismide alloys of GaP and GaAs," Phys. Rev. B **84**, 245202 (2011).

[138] M. Usman, C. A. Broderick, Z. Batool, K. Hild, T. J. C. Hosea, S. J. Sweeney, and E. P. O'Reilly, "Impact of alloy disorder on the band structure of compressively strained $GaBi_xAs_{1-x}$," Phys. Rev. B **87**, 115104 (2013).

[139] C. A. Broderick, S. Mazzucato, H. Carrère, T. Amand, H. Makhloufi, A. Arnoult, C. Fontaine, O. Donmez, A. Erol, M. Usman, et al., "Anisotropic electron g factor as a probe of the electronic structure of $GaBi_xAs_{1-x}$/GaAs epilayers," Phys. Rev. B **90**, 195301 (2014).

[140] M. Usman, C. A. Broderick, and E. P. O'Reilly, "Impact of disorder on the optoelectronic properties of $GaN_yAs_{1-x-y}Bi_x$ alloys and heterostructures," Phys. Rev. Applied **10**, 044024 (2018).

[141] L. Brey, C. Tejedor, and J. A. Vergés, "Scaling of the Hamiltonian and momentum in semiconductors," Phys. Rev. B **29**, 6840 (1984).

[142] C. Priester, G. Allan, and M. Lannoo, "Band-edge deformation potentials in a tight-binding framework," Phys. Rev. B **37**, 8519(R) (1988).

[143] H. Rücker, R. Enderlein, and F. Bechstedt, "Strain effects on the band structure of $Si/Si_{1-x}Ge_x$ (001) superlattices," Phys. Status Solidi B **158**, 595 (1983).

[144] M. C. Muñoz and G. Armelles, "X-point deformation potentials of III-V semiconductors in a tight-binding approach," Phys. Rev. B **48**, 2839 (1993).

[145] H. P. Hjalmarson, P. Vogl, D. J. Wolford, , and J. D. Dow, "Theory of substitutional deep traps in covalent semiconductors," Phys. Rev. Letters **44**, 810 (1980).

[146] Y.-H. Li, A. Walsh, S. Chen, W.-J. Yin, J.-H. Yang, J. Li, J. L. F. D. Silva, X. G. Gong, and S.-H. Wei, "Revised ab initio natural band offsets of all group IV, II-VI, and III-V semiconductors," Appl. Phys. Lett. **94**, 212109 (2009).

[147] A. C. Kirwan, E. J. O'Halloran, C. A. Broderick, S. Schulz, and E. P. O'Reilly, "Towards direct-gap emission in $Ge_{1-x}Sn_x$ and $Ge_{1-x}C_x$: a hybrid functional DFT analysis," Proc. 18^{th} IEEE International Conference on Nanotechnology (2018).

[148] D. J. Thouless, "Electrons in disordered systems and the theory of localization," Phys. Rep. **13**, 93 (1974).

[149] D. S. P. Tanner, M. A. Caro, E. P. O'Reilly, and S. Schulz, "Random alloy fluctuations and structural inhomogeneities in c-plane $In_xGa_{1-x}N$ quantum wells: theory of ground and excited electron and hole states," RSC Adv. **6**, 64513 (2016).

[150] A. Lindsay and E. P. O'Reilly, "A tight-binding-based analysis of the band-anticrossing model in GaN_xAs_{1-x}," Physica E **21**, 901 (2004).

[151] C. Harris, A. Lindsay, and E. P. O'Reilly, "Evolution of N defect states and optical transitions in ordered and disordered $GaP_{1-x}N_x$ alloys," J. Phys.: Condens. Matter **20**, 295211 (2008).

[152] Y. Zhang and L.-W. Wang, "Global electronic structure of semiconductor alloys through direct large-scale computations for III-V alloys $Ga_xIn_{1-x}P$," Phys. Rev. B **83**, 165208 (2011).

[153] P. R. C. Kent and A. Zunger, "Theory of electronic structure evolution in GaAsN and GaPN alloys," Phys. Rev. B **64**, 115208 (2001).

[154] P. R. C. Kent, L. Bellaiche, and A. Zunger, "Pseudopotential theory of III-V nitrides," Semicond. Sci. Technol. **17**, 851 (2002).

[155] P. Moontragoon, Z. Ikonic, and P. Harrison, "Band structure calculations of Si–Ge–Sn alloys: achieving direct band gap materials," Semiconductor Science and Technology **22**, 74222 (2007).

[156] S. J. Lee, H. S. Chung, K. Nahm, and C. K. Kim, "Band structure of ternary-compound semiconductors using a modified tight-binding method," Phys. Rev. B **42**, 2 (1990).

[157] D. S. P. Tanner, C. A. Broderick, A. C. Kirwan, S. Schulz, and E. P. O'Reilly, "Fully analytic valence force fields for the relaxation of group-IV semiconductor alloys: elastic properties of group-IV materials calculated from first principles," arXiv:2110.11888 (2021).

[158] A. Svizhenko, M. P. Anantram, T. R. Govindan, B. Biegel, and R. Venugopal, "Two-dimensional quantum mechanical modelling of nanotransistors," J. Appl. Phys. **91**, 2343 (2002).

[159] D. Esseni, M. Pala, P. Palestri, C. Alper, and T. Rollo, "A review of selected topics in physics based modeling for tunnel field-effect transistors," Semicond. Sci. Technol. **32**, 083005 (2017).

[160] M. Luisier and G. Klimeck, "OMEN: an atomistic and full-band quantum transport simulator for post-CMOS nanodevices," Proc. IEEE Conference on Nanotechnology (IEEE NANO) (2008).

[161] M. Luisier and G. Klimeck, "Atomistic full-band design study of InAs band-to-band tunneling field-effect transistors," IEEE Electron. Device Lett. **30**, 602 (2009).

[162] M. Luisier and G. Klimeck, "Performance comparisons of tunneling field-effect transistors made of InSb, carbon, and GaSb-InAs broken-gap heterostructures," Proc. IEEE Electron. Devices Meeting (IEEE IEDM) (2009).

[163] G. Klimeck and M. Luisier, "Atomistic modeling of realistically extended semiconductor devices with NEMO and OMEN," Comput. Sci. Eng. **12**, 28 (2010).

[164] H. Carrillo-Nuñez, M. Luisier, and A. Schenk, "Analysis of InAs-Si heterojunction nanowire tunnel FETs: extreme confinement vs. bulk," Solid State Electron. **113**, 61 (2015).

[165] E. Vitiello, S. Rossi, C. A. Broderick, G. Gravina, A. Balocchi, X. Marie, E. P. O'Reilly, M. Myronov, and F. Pezzoli, "Continuous-wave magneto-optical determination of the carrier lifetime in coherent $Ge_{1-x}Sn_x$/Ge heterostructures," Phys. Rev. Applied **14**, 064068 (2020).

[166] S. Das, C. A. Broderick, and E. P. O'Reilly, "Impact of band-anticrossing on band-to-band tunneling in highly-mismatched semiconductor alloys," `arXiv:2108.09328` (2021).

[167] A. Pan and C. O. Chui, "Modeling direct interband tunneling I: bulk semiconductors," J. Appl. Phys. **116**, 054508 (2014).

[168] E. O. Kane, "Zener tunneling in semiconductors," J. Phys. Chem. Solids **12**, 181 (1959).

[169] E. O. Kane, "Theory of tunneling," J. Appl. Phys. **32**, 83 (1961).

[170] C. A. Broderick, M. D. Dunne, D. S. P. Tanner, and E. P. O'Reilly, "Electronic structure evolution in dilute carbide $Ge_{1-x}C_x$ alloys and implications for device applications," J. Appl. Phys. **126**, 195702 (2019).

[171] C. A. Broderick, M. Usman, and E. P. O'Reilly, "Derivation of 12- and 14-band $\mathbf{k}\cdot\mathbf{p}$ Hamiltonians for dilute bismide and bismide-nitride semiconductors," Semicond. Sci. Technol. **28**, 125025 (2013).

[172] H. H. Park, S. Jin, W. Choi, M. Luisier, J. Kim, and K. H. Lee, "Atomistic Simulation of Band-to-Band Tunneling in SiGe: Influence of Alloy Scattering," International Conference on Simulation of Semiconductor Processes and Devices (2017).

[173] F. Settino, F. Crupi, S. Biswas, J. D. Holmes, and R. Duffy, "Modelling doping design in nanowire tunnel-FETs based on group-IV semiconductors," Mater. Sci. Semicond. Process. **62**, 201 (2017).

[174] J. K. Mamidala and R. Vishnoi and P. Pandey, "Tunneling Field-Effect Transistors (TFET) Modelling and Simulation" (Wiley, 2017).

[175] S. Shukla and R. Goswami, "Perspective performance assessment of tfets for low power applications: Challenges and prospects," ECS Journal of Solid State Science and Technology **9**, 085001 (2020).

[176] M. Luisier and G. Klimeck, "Simulation of nanowire tunneling transistors: From the Wentzel–Kramers–Brillouin approximation to full-band phonon-assisted tunneling," J. Appl. Phys. **107**, 084507 (2010).

[177] S. Sant, Q. Ding, M. Rau, M. Luisier, and A. Schenk, "Variability in the Characteristics of InGaAsSb/InAs Tunnel FETs Caused by Dopant-induced Traps," Electron Devices Technology and Manufacturing Conference (2019).

[178] J. Schulze, A. Blech, A. Datta, I. A. Fischer, D. Hähnel, S. Naasz, E. Rolseth, and E.-M. Tropper, "Vertical Ge and GeSn heterojunction gate-all-around tunneling field effect transistors," Solid State Electron. **110**, 59 (2019).